Diss. ETH No 12658

Measurement of muon-pair production with the L3 experiment

A dissertation submitted to the
SWISS FEDERAL INSTITUTE OF TECHNOLOGY ZURICH

for the degree of
Doctor of Natural Sciences

presented by
Arne Robohm

Dipl.–Phys. University of Karlsruhe

born June 14th, 1967
citizen of Germany

accepted on the recommendation of

Prof. Dr. H. Hofer,   examiner
Prof. Dr. H.C. Walter,   co-examiner

1998

Abstract

This thesis reports on measurements of e^+e^- annihilation into muon pairs with the L3 detector at LEP. At center-of-mass energies around the Z mass, 16833 muon pairs are selected, corresponding to 23.7 pb^{-1} of integrated luminosity. From the data samples taken at center-of-mass energies between 130 GeV and 183 GeV, 692 muon pairs are selected, corresponding to 88.5 pb^{-1} of integrated luminosity. The cross section and forward-backward asymmetry measurements, combined with other results on lepton-pair production, are used to determine the mass and width of the Z boson, its couplings to leptons and the γZ interference. The results obtained are:

$$m_Z = 91190 \pm 3\,\mathrm{MeV},$$
$$\Gamma_Z = 2502 \pm 4\,\mathrm{MeV},$$
$$\overline{g}^l_A = -0.5013 \pm 0.0006,$$
$$\overline{g}^l_V = -0.0399 \pm 0.0018,$$
$$j^{\mathrm{tot}}_{\mathrm{had}} = 0.19 \pm 0.17.$$

The results of all measurements agree well with the Standard Model predictions.

i

Zusammenfassung

Diese Doktorarbeit präsentiert Messungen der e^+e^- Vernichtung in Muonpaare mit dem L3 Detektor am LEP Beschleuniger. Bei Schwerpunktsenergien im Bereich der Z-Masse werden 16833 Muonpaare selektiert, welche einer integrierten Luminosität von 23.7 pb^{-1} entsprechen. Aus den Daten, welche bei Schwerpunktsenergien zwischen 130 GeV und 183 GeV genommen wurden, werden 692 Muonpaare selektiert. Diese entsprechen einer integrierten Luminosität von 88.5 pb^{-1}. Die Messungen der Wirkungsquerschnitte und Vorwärts-Rückwärts-Asymmetrien, zusammen mit weiteren Ergebnissen der Leptonpaar-Erzeugung, werden verwendet, um Masse und Zerfallsbreite des Z Bosons, seine Kopplungen an Leptonen sowie die γZ Wechselwirkung zu bestimmen. Die Resultate sind:

$$m_{\mathrm{Z}} = 91190 \pm 3 \mathrm{MeV},$$
$$\Gamma_{\mathrm{Z}} = 2502 \pm 4 \mathrm{MeV},$$
$$\bar{g}_A^l = -0.5013 \pm 0.0006,$$
$$\bar{g}_V^l = -0.0399 \pm 0.0018,$$
$$j_{\mathrm{had}}^{\mathrm{tot}} = 0.19 \pm 0.17.$$

Die Ergebnisse aller Messungen stimmen gut mit den Vorhersagen des Standardmodells überein.

Contents

List of Figures

List of Tables

Chapter 1

Introduction

The main task of physics in general is to describe all physical phenomena with a few basic principles. Particle physics tries to explain the variety of the universe by means of a few elementary particles, quarks and leptons, and their interactions. There are four kinds of interactions: the weak and the strong interactions, electromagnetism and gravitation. The first three are described by two quantum field theories which build up the Standard Model of particle physics. The inclusion of the fourth interaction, gravitation, and thus the unification of all forces into one theory is still to be achieved.

The first experimental confirmation of the electroweak theory, which combines electromagnetism and the weak interaction, took place in 1973. The Gargamelle collaboration at CERN, the European nuclear research center, observed neutral weak currents in neutrino electron scattering [13]. The existence of vector bosons, predicted to carry the weak forces, was confirmed in 1983 with the discovery of the W and Z bosons at the SPS collider at CERN [14].

In 1989 the LEP e^+e^--collider and its four experiments, among them the L3 detector, began operation. One of their major tasks is to precisely measure the properties of the W and Z bosons. Until 1995, LEP was operated at center-of-mass energies around 91 GeV, corresponding to the Z mass, where electrons and positrons annihilate almost exclusively into Z bosons. Measurements of the resonant fermion-pair production at these center-of-mass energies enable the determination of mass and width of the Z boson and its couplings to leptons and quarks. Since the Z mass is a fundamental parameter of the Standard Model, its precise measurement improves the accuracy of Standard Model predictions.

From 1995, data at center-of-mass energies between 130 GeV and 183 GeV was taken. Off the Z resonance the contribution of the γZ interference to the total cross section is much larger than around the Z pole. The fermion-pair cross section measurements thus allow an improved determination of the γZ interference.

This thesis gives a brief introduction to the Standard Model. It describes the different sub-detectors of the L3 experiment, with emphasis on the muon spectrometer. Measurements of cross sections and forward-backward asymmetries for muon-pair production at four center-of-mass energies around the Z mass and at five center-of-mass energies between 130 GeV and 183 GeV are presented. Measurements of hadron, electron and tau-pair production are included for the determination of mass and width of the Z boson, the couplings of the Z to lep-

tons and the γZ interference. All these measurements are a sensitive test of the Standard Model.

Chapter 2

The Standard Model

The Standard Model [1] describes the processes of the electromagnetic, weak and strong interactions. The phenomena of strong interactions are explained by QCD[1] [1], while electromagnetic and weak interactions are combined to an electroweak theory, also known as the Glashow-Salam-Weinberg theory [2].

According to the Standard Model, matter consists of elementary fermions. Interactions between the fermions are described by means of gauge theories. The elementary particles of the gauge fields are called *gauge bosons*. The fermions are divided into three generations, each consisting of two leptons and two quarks. An anti-particle exists for every fermion.

The Standard Model is based on the symmetry groups $SU(3)$ and $SU(2)_L \times U(1)_Y$ describing strong and electroweak interactions, respectively. The strong interaction only affects quarks. Their gauge bosons, the gluons, form an $SU(3)$-octet. The gauge bosons of the electroweak interaction form an isospin-triplet of the $SU(2)$ and a $U(1)$-singlet. The fermions and gauge bosons are listed in table 2.1 with their charges and masses [3].

2.1 Electroweak theory

The $SU(2)_L$ part of the electroweak gauge symmetry describes transformations in the space of weak isospin, T. It takes into account that the weak isospin current only couples to left-handed fermions. The second part, $U(1)_Y$, represents a rotation in the space of weak hypercharge, Y. The weak hypercharge is defined via the electric charge, Q, and third component of the isospin, T^3:

$$Q = T^3 + \frac{Y}{2}.$$

The weak isospin and hypercharge quantum numbers for leptons and quarks are listed in table 2.2.

As the electromagnetic current is coupled to the photon, the electroweak currents are coupled to vector bosons. An isotriplet of vector fields, W^i_μ, couples with strength g to the weak isospin current, J^i_μ, and a single vector field, B_μ, couples to the weak hypercharge current, j^Y_μ, with a strength $g'/2$. Gauge invariance

---

[1] Quantum chromodynamics

3

	fermions			
	leptons		quarks	
1. generation	ν_e	e	u	d
q/e	0	-1	$+\frac{2}{3}$	$-\frac{1}{3}$
m	<7.0 eV	511 eV	$\approx$5 MeV	$\approx$10 MeV
2. generation	ν_μ	μ	c	s
q/e	0	-1	$+\frac{2}{3}$	$-\frac{1}{3}$
m	<0.17 MeV	106 MeV	$\approx$1.3 GeV	$\approx$200 MeV
3. generation	ν_τ	τ	t	b
q/e	0	-1	$+\frac{2}{3}$	$-\frac{1}{3}$
m	<24 MeV	1.777 GeV	$\approx$180 GeV	$\approx$4.3 GeV

	gauge bosons			
	SU(3)		SU(2)$\times$U(1)	
	g	γ	Z	$W^\pm$
q/e	0	$<6\cdot10^{-16}$ eV	0	±1
m	0	0	$\approx$91.19 GeV	$\approx$80.33 GeV

Table 2.1: The charges and masses of the fundamental particles of the Standard Model.

requires the gauge bosons of the electroweak theory to be massless. However, experiments show that the Z and $W^\pm$ bosons are massive. One possibility for the gauge invariant generation of massive gauge bosons is the spontaneous symmetry breaking introduced by the Higgs mechanism [4]. The fields

$$W_\mu^\pm = \sqrt{\frac{1}{2}}\left(W_\mu^1 \mp W_\mu^2\right)$$

describe the massive charged W bosons. The two neutral fields W_μ^3 and B_μ mix in such a way that the mass eigenstates are:

$$A_\mu = B_\mu\cos\theta_W + W_\mu^3\sin\theta_W,$$
$$Z_\mu = -B_\mu\sin\theta_W + W_\mu^3\cos\theta_W,$$

where θ_W is the weak mixing angle. The fields A_μ and Z_μ are identified with the massless photon, γ, and the massive boson Z. Corresponding to the gauge bosons γ, Z and $W^\pm$ there are three currents describing the coupling of the fermions to the respective gauge fields: the electromagnetic, the neutral weak and the charged weak current.

The coupling of fermions with charge Q_f to the photon field by means of the electromagnetic current, J_μ^{em}, is based on the elementary charge, e:

$$eJ_\mu^{em} \equiv e\left(J_\mu^3 + \frac{1}{2}j_\mu^Y\right).$$

The elementary charge, e, is related to the coupling constants g and g' as follows:

$$e = g\sin\theta_W = g'\cos\theta_W.$$

leptons	T	T^3	Y
$\nu_e,\ \nu_\mu,\ \nu_\tau$	$\frac{1}{2}$	$\frac{1}{2}$	-1
$e_L^-,\ \mu_L^-,\ \tau_L^-$	$\frac{1}{2}$	$-\frac{1}{2}$	-1
$e_R^-,\ \mu_R^-,\ \tau_R^-$	0	0	-2
quarks			
$u_L,\ c_L,\ t_L$	$\frac{1}{2}$	$\frac{1}{2}$	$\frac{1}{3}$
$d_L,\ s_L,\ b_L$	$\frac{1}{2}$	$-\frac{1}{2}$	$\frac{1}{3}$
$u_R,\ c_R,\ t_R$	0	0	$\frac{4}{3}$
$d_R,\ s_R,\ b_R$	0	0	$-\frac{2}{3}$

Table 2.2: The weak isospin and hypercharge quantum numbers of leptons and quarks.

The mixing angle, θ_W, is given by the ratio of the two independent couplings constants:

$$\tan\theta_W = \frac{g'}{g}.$$

In the Standard Model the masses of the vector bosons are not fixed, but their ratio is related to the Weinberg angle:

$$\cos\theta_W = \frac{m_W}{m_Z}.$$

The charged weak current has a pure V-A structure while the neutral weak current contains unequal vector and axial-vector couplings, g_V and g_A. Their values are:

$$g_V^f = T_f^3 - 2Q_f\sin^2\theta_W,$$
$$g_A^f = T_f^3.$$

Figure 2.1 shows the Feynman graphs for (a) the electromagnetic, (b) the charged current, and (c) the neutral current interaction. The respective vertex factors are:

- electromagnetic interaction (γ): $-ieQ_f\gamma^\mu$
- charged current interaction ($W^\pm$): $-i\frac{g}{\sqrt{2}}\gamma^\mu\frac{1}{2}(1-\gamma^5)$
- neutral current interaction (Z): $-i\frac{g}{\cos\theta_W}\gamma^\mu\frac{1}{2}(g_V^f - g_A^f\gamma^5)$

2.2 The process $e^+e^- \to \mu^+\mu^-$

2.2.1 Cross Section

In the Born approximation the exchange of a photon as well as the exchange of a Z boson contribute to the process $e^+e^- \to \mu^+\mu^-$ (figure 2.2). For center-of-mass
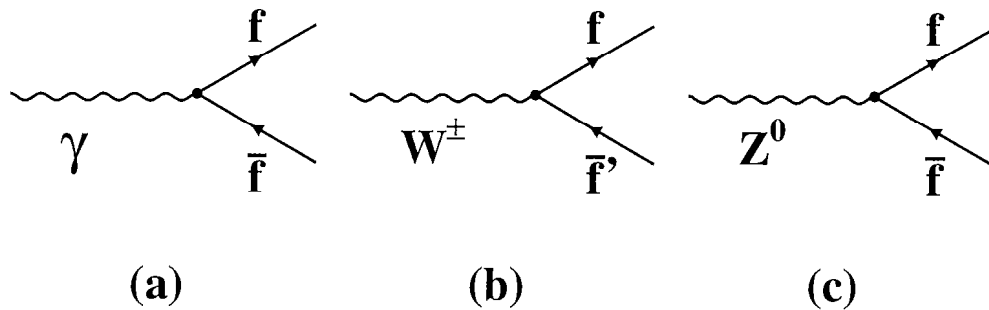
Figure 2.1: Feynman graphs for (a) electromagnetic, (b) charged current, and (c) neutral current interaction.
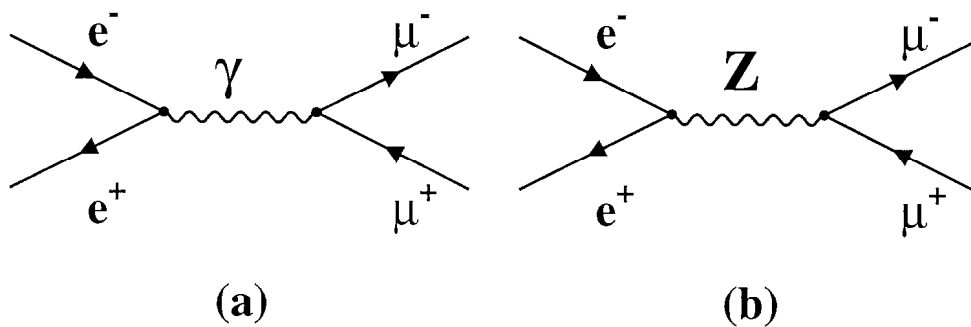
Figure 2.2: Feynman graphs for muon-pair production via (a) photon and (b) Z boson exchange.

energies $\sqrt{s} \approx m_Z$ the contribution from photon exchange is much smaller than the one from Z exchange.

The differential cross section for the process $e^+e^- \to \mu^+\mu^-$ is given by [5]:

$$\frac{d\sigma}{d\Omega} = \frac{\alpha^2}{4s} \left[G_1(s)(1 + \cos^2\theta) + G_3(s) \cdot \cos\theta \right], \tag{2.1}$$

taking into consideration that $m_\mu^2 \ll s$. The functions $G_i(s)$ are:

$$G_1(s) = Q_f^2 - 2g_V^e g_V^\mu Q_f \mathrm{Re}\chi_0(s) + \left(g_V^{e^2} + g_A^{e^2} \right) \left(g_V^{\mu^2} + g_A^{\mu^2} \right) |\chi_0(s)|^2,$$

$$G_3(s) = -4g_A^e g_A^\mu Q_f \mathrm{Re}\chi_0(s) + 8g_V^e g_A^e g_V^\mu g_A^\mu |\chi_0(s)|^2.$$

The term of equation 2.1 containing $G_1(s)$ characterises the photon and Z exchange, where the Q_f^2 of $G_1(s)$ belongs to the photon exchange. The interference is described by the asymmetric terms containing $\mathrm{Re}\chi_0(s)$, where the contribution from $G_3(s)$ dominates. The scattering angle θ is defined as the angle between the incoming electron, e^-, and the scattered muon, μ^- (figure 2.3). The pole term

$$\chi_0(s) = \frac{s}{s - m_Z^2 + i\, m_Z \Gamma_Z^0}$$

contains the mass of the Z, m_Z, and its width:

$$\Gamma_Z^0 = \sum_f \frac{\alpha}{3} m_Z \left(g_V^{f^2} + g_A^{f^2} \right).$$

The vector and axial-vector coupling constants are represented by g_V and g_A, respectively. Integrating equation 2.1 over $d\Omega$ leads to the total cross section, σ_{tot}^0:

$$\sigma_{\mathrm{tot}}^0(s) = \int_{-1}^{1} \frac{d\sigma}{d\cos\theta}(s,\theta)\, d\cos\theta = \frac{4\pi\alpha^2}{3s} G_1(s). \tag{2.2}$$

On the Z resonance ($\sqrt{s} = m_Z$) equation 2.2 simplifies to:

$$\sigma_{\mathrm{tot}}^{\mathrm{res}} = \frac{12\pi\Gamma_e\Gamma_\mu}{m_Z^2 \Gamma_Z^{0^2}},$$

where Γ_l are the lepton widths:

$$\Gamma_l = \frac{\alpha\, m_Z}{12\sin^2\theta_W \cos^2\theta_W} \left(g_V^{l^2} + g_A^{l^2} \right) \qquad \text{with } l = e, \mu.$$

2.2.2   Forward-backward asymmetry

The differential cross section (equation 2.1) is characterised by a symmetric term, $\propto(1+\cos^2\theta)$, and an asymmetric part, $\propto\cos\theta$. The deviation from a symmetric distribution is measured by the forward-backward charge asymmetry [7]:

$$A_{\mathrm{fb}}(s) = \frac{\sigma_f - \sigma_b}{\sigma_f + \sigma_b}, \tag{2.3}$$
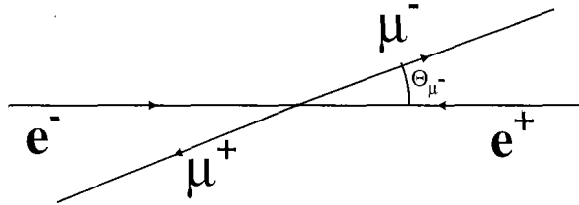
Figure 2.3: Muon-pair production with the fermion, μ^-, scattered into the forward hemisphere with respect to the e^--beam direction ($\cos\theta > 0$).

with

$$\sigma_{\mathrm{f}} = 2\pi \int_0^1 \frac{d\sigma}{d\Omega}\, d\cos\theta \quad \text{and} \quad \sigma_{\mathrm{b}} = 2\pi \int_{-1}^0 \frac{d\sigma}{d\Omega}\, d\cos\theta.$$

This gives for the asymmetry in lowest order:

$$A_{\mathrm{fb}}^0 = \frac{3}{8}\frac{G_3(s)}{G_1(s)}. \tag{2.4}$$

Due to the γZ interference the asymmetry is positive (negative) for center-of-mass energies above (below) the Z mass. The coupling of the photon to electron and muon is a pure vector coupling while the coupling of the Z boson is dominated by the axial-vector part ($|g_V/g_A| \approx 0.08$). On the Z resonance ($\sqrt{s} = m_Z$) the interference term disappears. In addition, neglecting the photon exchange with respect to the Z exchange and assuming lepton universality, equation 2.4 simplifies to:

$$A_{\mathrm{fb}}^{\mathrm{res}} = 3\frac{g_V^{l^2} g_A^{l^2}}{\left(g_V^{l^2} + g_A^{l^2}\right)^2} \approx 3\frac{g_V^{l^2}}{g_A^{l^2}} \qquad (\text{for } g_V^{l^2} \ll g_A^{l^2}). \tag{2.5}$$

Alternatively the differential cross section can also be parametrised using the total cross section, σ_{tot}, and the forward-backward asymmetry, $A_{\mathrm{fb}}(s)$:

$$\frac{d\sigma}{d\cos\theta} = 2\pi\frac{d\sigma}{d\Omega} = \sigma_{\mathrm{tot}}(s)\left[\frac{3}{8}\left(1 + \cos^2\theta\right) + A_{\mathrm{fb}}(s)\cos\theta\right]. \tag{2.6}$$

2.3 Radiative corrections

For precision measurements higher order contributions also have to be considered. These radiative corrections to the process $e^+e^- \rightarrow \mu^+\mu^-$ lead to modifications of σ_{tot}^0 and A_{fb}^0. The radiative (one-loop) corrections can be subdivided into two sub-classes:

- weak corrections,

- QED[2] corrections.

A detailed description of the radiative corrections can be found in [5, 6, 7].

---

[2]Quantum electrodynamics
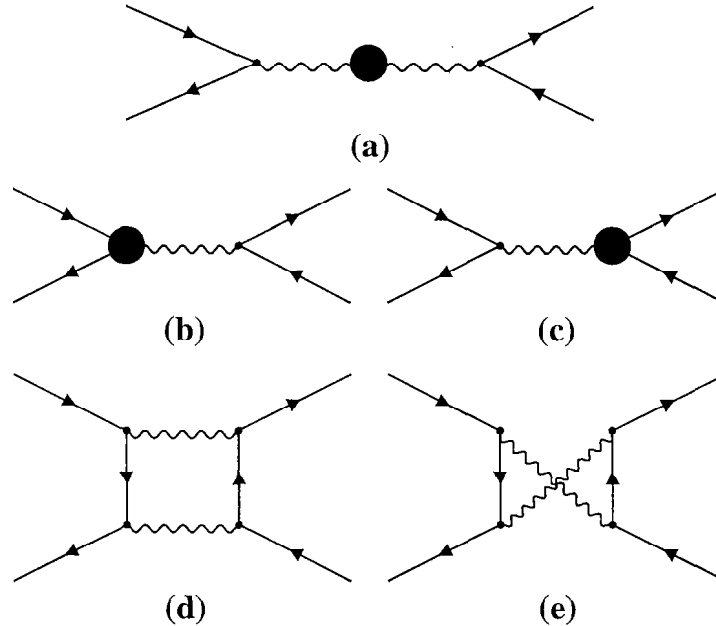
Figure 2.4: Radiative weak corrections to the process $e^+e^- \rightarrow \mu^+\mu^-$. Figure (a) shows the propagator correction, figures (b,c) and (d,e) represent vertex and box corrections, respectively.

2.3.1 Weak corrections

The weak corrections collect all non-photonic corrections arising from the following processes [5]:

- Propagator corrections describe the modification of the gauge boson propagator by self energy insertions (figure 2.4a). In case of the photon and the Z propagator this leads to a $\sqrt{s}$-dependence of the fine structure constant, α, and the Z-width, respectively.

- Vertex corrections take into account the exchange of particles between the two incoming or the two outgoing fermions (figures 2.4b,c). They are absorbed by a transformation of the couplings, g_V and g_A, to effective couplings, $\overline{g}_V$ and $\overline{g}_A$, respectively.

- Box corrections describe two gauge boson exchanges (figures 2.4d,e).

The inclusion of the radiative corrections leads to the improved Born approximation. The general structure of the Born approximation described in section 2.2.1 is maintained by re-defining the variables α, Γ_Z, g_A and g_V to their effective values $\alpha(s)$, $\Gamma_Z(s)$, $\overline{g}_A$ and $\overline{g}_V$, respectively.

2.3.2 QED corrections

QED corrections comprise corrections due to emission or absorption of a bremsstrahlung or virtual photon (figure 2.5). The contributions to the bremsstrahlungs
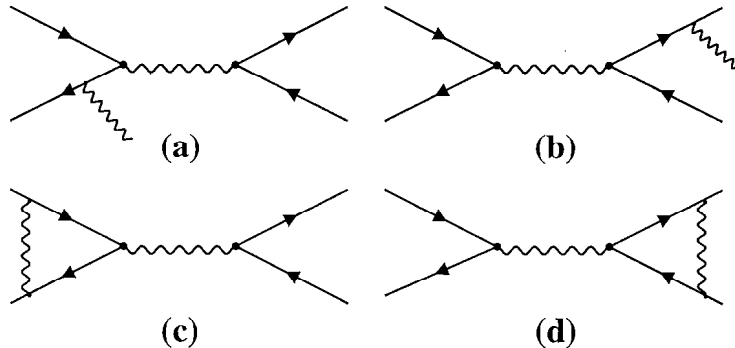
Figure 2.5: Radiative QED corrections to the process $e^+e^- \rightarrow \mu^+\mu^-$. Figures (a) and (b) show the emission of an ISR and FSR photon, respectively. Figures (c,d) are examples for virtual photon loops.

correction arise from initial state radiation (ISR), final state radiation (FSR) and from the interference between initial and final state radiation. ISR and FSR radiation take into account the coupling of a photon to an incoming and outgoing fermion, respectively. The size of the interference contribution to the total cross section is negligible [8]. When no stringent kinematic cut on the outgoing fermion-pair is imposed, the final state radiative correction gives a multiplicative factor $1+\delta_{QED}$ which is smaller than 0.17% [6].

If an ISR photon is emitted by the electron or the positron, the initial center-of-mass energy, $\sqrt{s}$, is lowered to an effective center-of-mass energy of the annihilation process, $\sqrt{s'}$. Using the energy of the emitted ISR photon, E_γ, the $\sqrt{s'}$ value is given by:

$$s' = sz = s(1 - \frac{E_\gamma}{\sqrt{s}/2}) = s - 2E_\gamma\sqrt{s}. \tag{2.7}$$

Taking all radiative weak and QED corrections into account, the cross section σ_{tot} is then given by a convolution [6]:

$$\sigma_{tot}(s) = \int_{z_0}^{1} G(z) \, \sigma_w(sz) \, dz, \tag{2.8}$$

where the cross section including weak corrections is denoted by σ_w. The radiator function $G(z)$ is the probability to emit an ISR photon, then leading to an effective center-of-mass energy, $\sqrt{s'}$. The integration ranges over all possible ISR photon energies between the kinematic limit z_0 and 1.

Chapter 3

The L3 experiment

The European nuclear research center CERN[1] is situated in Geneva, Switzerland. The experiments ALEPH, DELPHI, L3 and OPAL [15, 16] are installed in four out of eight possible interaction zones of the LEP[2] accelerator (figure 3.1).
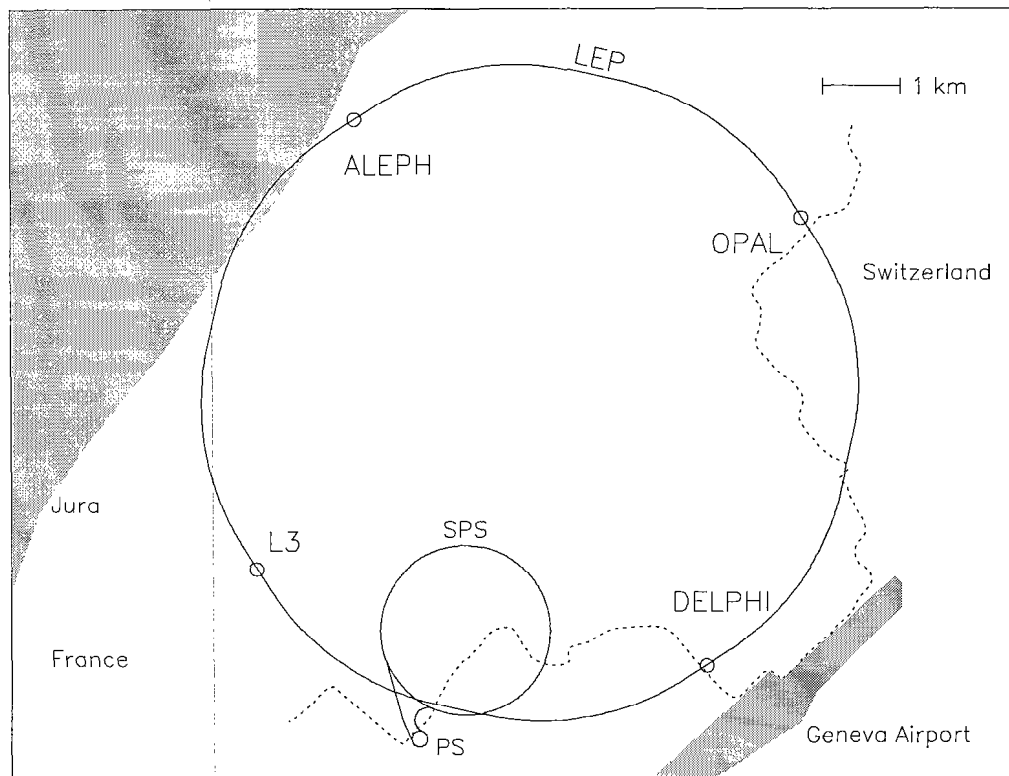
Figure 3.1: Map of the LEP accelerator at CERN.

The L3 experiment (figures 3.2, 3.3) was constructed to detect particles produced in e^+e^--collisions. Priorities were set for the energy measurement of photons and

---

[1] Conseil Européen pour la Recherche Nucléaire
[2] Large Electron Positron collider

11
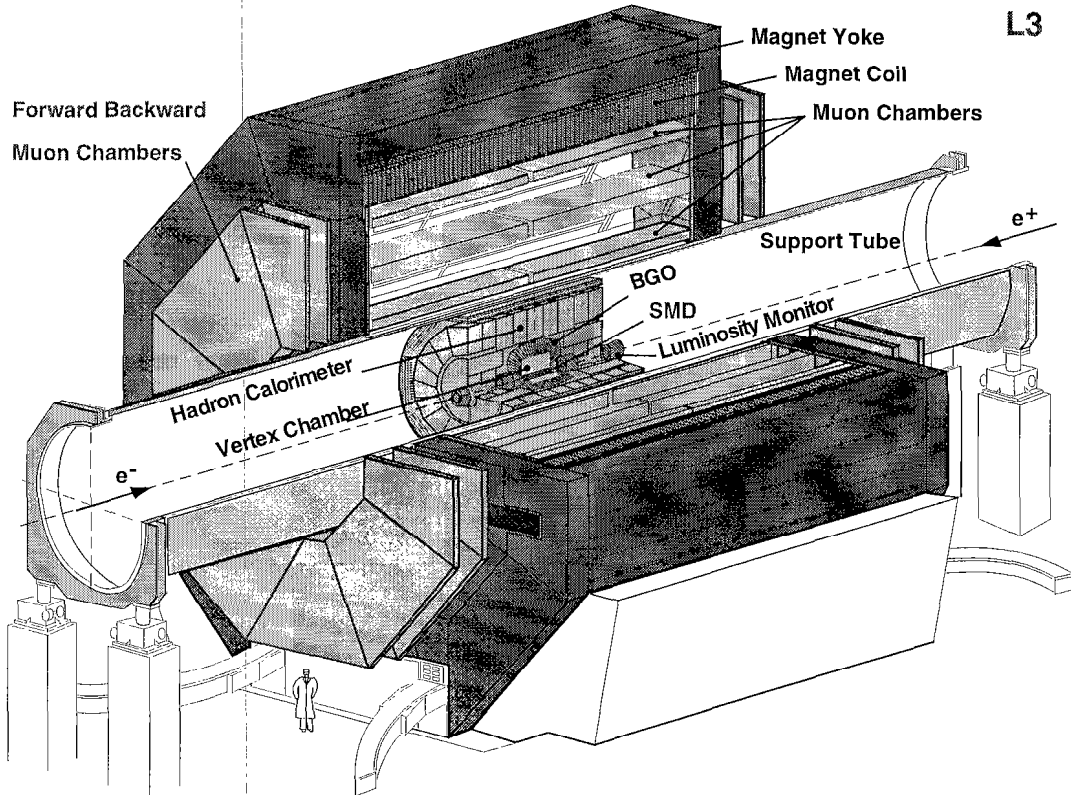
Figure 3.2: Perspective view of the L3 detector.

electrons and the momentum measurement of muons. The innermost components are the micro-vertex detector [18] and a central tracking chamber [19]. They are followed by the electromagnetic calorimeter [21], scintillation counters [23] and the hadron calorimeter [24]. The outermost detector is the muon spectrometer consisting of three layers of drift chambers [25]. The entire detector is placed inside a solenoid magnet with an inner diameter of 12 m. It generates a homogeneous field of 0.5 T parallel to the beam axis. On both sides of the experiment there are iron doors returning the flux of the solenoid field. Coils are wrapped around these doors to build up a toroid field of 1.2 T. Three layers of muon chambers are mounted onto the iron doors [26]. One layer is situated on the inside of the doors, and two are on the outside. The two outer layers are covered with resistive plate counters [27]. Close to the beam pipe on both ends of the experiment there is a very small angle tagger (VSAT) and a lead ring covered with plastic scintillators (ALR) [28]. The luminosity is measured with the luminosity monitor and a silicon strip detector (SLUM) [41]. In the following sections, the most important detectors for the muon-pair production analysis are described in more detail.

The coordinate system of the L3 experiment is defined such that θ is the polar and Φ the azimuthal angle.
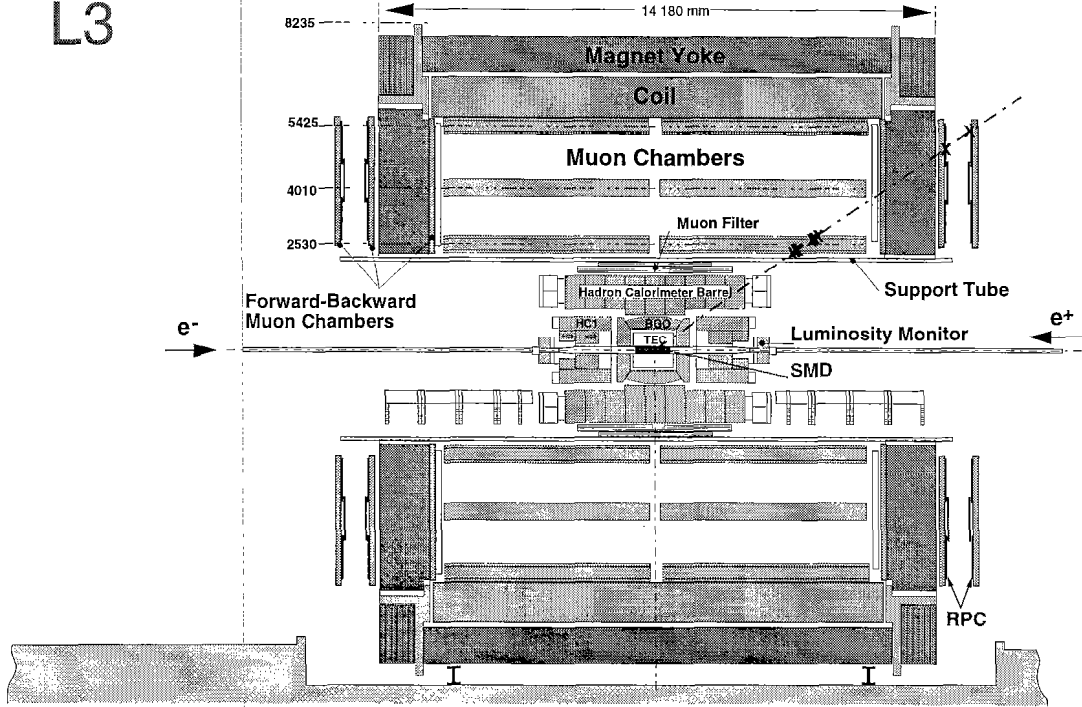
Figure 3.3: Side view of the L3 detector with a muon traversing the detector.

3.1 LEP accelerator

The LEP accelerator has a circumference of about 26.7 km. Electrons and positrons are accelerated in opposite directions and kept on their circular trajectory by dipole magnets. The acceleration is performed by radio frequency cavities and takes place at the straight parts of LEP on both sides of each of the eight potential interaction points. The electrons and positrons are each stored in four bunches. In 1995 and 1996 every bunch was subdivided in up to four bunchlets. The maximum beam energy to date of 94.5 GeV was reached in May 1998. It is mainly limited by the energy loss due to synchrotron radiation which is proportional to E^4.

The energy calibration

The calibration of the LEP center-of-mass energy is important for a precise determination of mass and width of the Z boson. The method used for the energy calibration is resonant spin de-polarisation [39]. Due to the Sokolov-Ternov effect [11], a transversal polarisation of the beam is built up. The frequency of the spin precession of electrons in the polarised beam is directly related to the beam energy:

$$\nu_s = \frac{g_e - 2}{2} \frac{E_{beam}}{m_e},$$

where ν_s is the number of spin precessions per revolution, $(g_e - 2)/2$ the anomalous moment of the electron, E_{beam} the beam energy and m_e the mass of the electron.

An oscillating horizontal magnetic field is applied to the vertically polarised beam. From the frequency of the oscillating field that de-polarises the beam the spin precession frequency and thus the beam energy is derived. It allows a relative precision of the energy measurement of 2.6×10^{-5} for 1995 and of 3.5×10^{-4} for 1996 [40].

3.2   Luminosity measurement

The luminosity is defined as:

$$\mathcal{L} = \frac{n_b N_{e^-} N_{e^+}}{4\pi T \sigma_x \sigma_y},$$

with N_{e^-} and N_{e^+} the number of electrons and positrons per bunch, respectively, n_b the number of bunches and T the time per revolution. σ_x and σ_y are the transversal dimensions of the bunch. Not all parameters are known to sufficient precision. Hence a process with a well known theoretical cross section is used for the luminosity determination:

$$\mathcal{L} = \frac{N}{\sigma \epsilon},$$

where N is the background corrected number of selected events, σ the theoretical cross section and ϵ the acceptance and selection correction.

The total luminosity, $\mathcal{L}$, is determined by measuring the number of small-angle Bhabha scatterings, $e^+ e^- \to e^+ e^- (\gamma)$ [41]. For this purpose, luminosity monitors [17] are located on either side of the interaction point at $z=\pm2.7$ m. They are cylindrical calorimeters with an inner radius of 68.2 mm and an outer radius of 191.4 mm. Each one is a finely segmented and azimuthally symmetric array of 304 BGO[3] crystals which is split in the vertical plane. A silicon strip detector (SLUM) ensures a precise definition of the fiducial volume [41].

To determine the visible cross section[4], $e^+ e^- \to e^+ e^- (\gamma)$ events are simulated at a fixed center-of-mass energy, $\sqrt{s}$, of 91.18 GeV using the event generator BHLUMI [49]. For center-of-mass energies, $\sqrt{s'}$, off the Z peak, the visible cross section is rescaled by s/s' [63] since small-angle Bhabha scattering is a QED process.

3.3   Micro vertex detector

The micro vertex detector (SMD[5]) [18] is mounted directly on the outside of the beam pipe. It consists of two layers of silicon strip detectors. They allow the position determination of a track with a precision of 7 μm in the r-Φ-plane and 14 μm in the r-z-plane. The measurement of the distance of closest approach (DCA) to the interaction point helps in the separation of muons from cosmic radiation and muon-pair events.

---

[3] Bismuth Germanium Oxide

[4] The cross section for small-angle Bhabha scattering (t-channel) in the polar angular region covered by the luminosity monitors.

[5] Silicon Micro Vertex Detector

Grid
Anodes
Grid
Cathodes
Z chamber

Outer
TEC

Charged
particle
track

Inner
TEC

SMD

Y
B
X
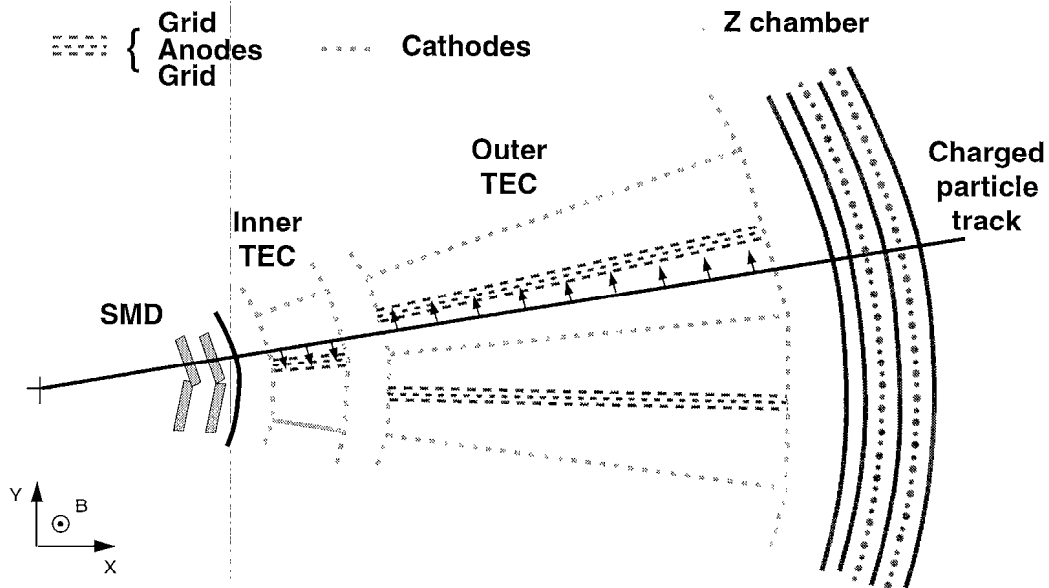
Figure 3.4: Sector of the central tracking chamber.

3.4 Central tracking chamber

The inner ring of the central tracking chamber (TEC[6]) [19] is split into 12 sectors with eight anode wires each, the outer ring comprises 24 sectors with 54 anode wires each. Two outer sectors cover one inner sector (figure 3.4). Thus it is possible to resolve ambiguities in the position determination originating from the two halves of each sector. The distance between the first and the last anode wire is about 31.7 cm. Additional wire planes separate the drift region from the region of the gas amplification around the anode wires. This results in relatively small drift velocities that allow to measure the time of the signal and hence to determine the position of the track more accurately than in drift chambers (principle of *time expansion*). The TEC is surrounded by two layers of multi-wire proportional chambers with cathode strip read-out [20]. They measure the z-coordinate, i.e. the polar angle, of the tracks. The resolution for the distance of closest approach is 57.7 μm. Combined with the position determination of the SMD a resolution for the transverse momentum $1/p_\perp$ of 0.0147 GeV^{-1} is achieved [45].

3.5 Electromagnetic calorimeter

The electromagnetic calorimeter (ECAL) [21] consists of Bismuth Germanium Oxide crystals ($Bi_4Ge_3O_{12}$). The central part covers the polar angular region of $42° < \theta < 138°$ and contains 7680 crystals. Both endcaps cover the region between

---

[6] Time Expansion Chamber
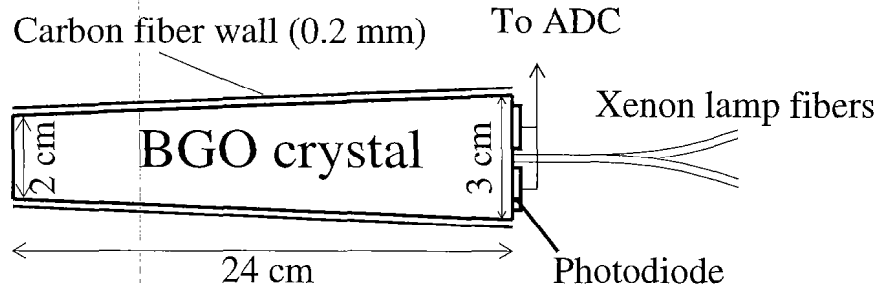
Figure 3.5: A BGO crystal of the electromagnetic calorimeter.

12° and 38° with respect to the beam axis and contain 1527 crystals each. The crystals are 24 cm long, their radiation length is 1.2 cm and the absorption length for hadronic particles is about 22 cm. Photo diodes are used for the read-out (figure 3.5). The angular resolution is of the order of 0.5°. The energy resolution ranges from 5% for E=100 MeV to 1.4% for E=45 GeV [22, 43].

3.6 Scintillation counters

On the outside of the electromagnetic calorimeter, there is one layer of plastic scintillation counters [23], covering the whole acceptance region of the muon spectrometer. They measure the time between the e^+e^--interaction and the moment the particle crosses the scintillation counter. This timing signal offers one possibility to distinguish between muons from muon-pair events and muons originating from cosmic radiation. The central region of the experiment is covered by 30 counters, the endcap regions by 16 counters each. They are read out by photo-multipliers. The time resolution is 0.8 ns and 1.9 ns for the central and endcap counters respectively [44].

3.7 The hadron calorimeter

The hadron calorimeter (HCAL) [24] is built up of alternating layers of uranium as showering material and multi-wire proportional chambers to measure the deposited energy. It covers the polar angular range of 5.5°< θ < 174.5° (figure 3.6). The HCAL measures energy and direction of hadronic jets. Its material represents about eight absorption lengths and thus prevents most particles subject to strong interaction from reaching the muon spectrometer. Surrounding the HCAL, the muon filter, a layer of brass absorber plates interleaved with proportional tubes,

16
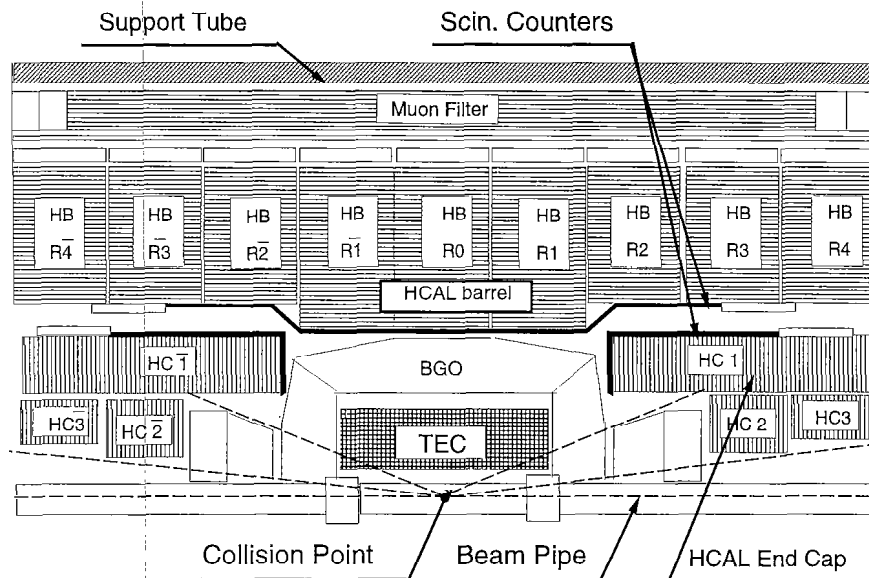
Figure 3.6: Side view of the hadron calorimeter.

also serves this purpose. The angular resolution is of the order of 0.5° and the angular deflection caused by multiple scattering has an RMS of 0.2°.

3.8 The muon spectrometer

The L3 muon spectrometer is composed of two components:

- the central detector (*barrel*) muon chambers [25],

- the endcap (*forward-backward*) muon chambers [26].

The barrel muon chambers are placed completely inside the solenoid magnet and cover the polar angular region of 44°< θ < 136°. They are arranged in 2 × 8 units called *octants* (see figure 3.9). Both end-caps consist of 16 sectors of forward-backward chamber units covering the polar angular region of 24°< θ < 44° with respect to the beam axis. One layer is mounted on the inside (FI) and two layers (FM, FO) on the outside of iron doors which contain a toroid magnetic field and return the flux of the L3 solenoid magnetic field (figure 3.7). For triggering, the middle (FM) and outer (FO) layers are covered by resistive plate counters (RPC, figure 3.8) [27, 46].

3.8.1 The barrel muon chambers

In each octant there are five drift chambers measuring the coordinates of the track in the r-ϕ-plane (*p-chambers*). They comprise one inner chamber (MI),

17
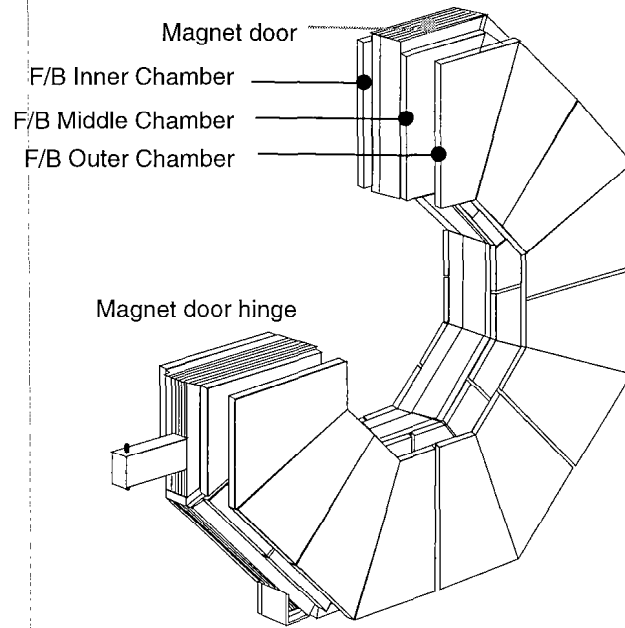
Figure 3.7: Perspective view onto three quarters of the forward-backward muon chambers.
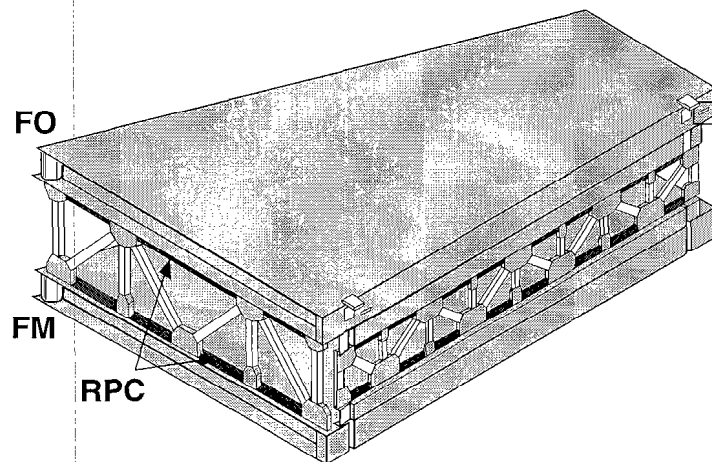
Figure 3.8: A forward-backward muon chamber module with resistive plate counters.

18
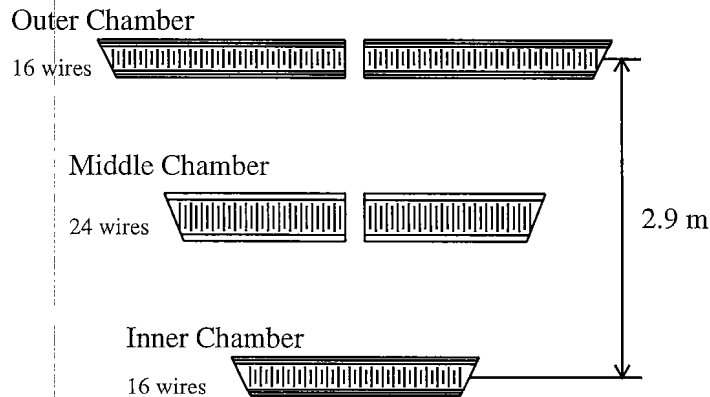
Figure 3.9: Front view of a barrel muon chamber octant.

two middle (MM) and two outer chambers (MO) (figure 3.9). Their cells have a width of 101.5 mm and contain 16 (MI, MO) or 24 (MM) signal wires parallel to the beam axis. The hits of the wires within one cell or two adjacent cells are combined to segments. Tracks with segments in all three p-chamber layers are called *triplets*, if only two layers are hit they are referred to as *doublets*.

In addition there are chambers mounted below and on top of the MI and MO chambers to measure the r-θ-coordinates (*z-chambers*). They are built up of two layers of 109 mm wide cells with one signal wire each. These two layers have an overlap of half a cell width. This allows to resolve left-right ambiguities and to measure the polar angle with a precision of 0.3°. The single wire resolutions are ≈220 μm for p-chambers and ≈500 μm for z-chambers [42, 59].

The bending of the muon trajectory in the barrel is caused by the solenoid magnetic field and is used to calculate the transverse momentum, $p_\perp$, of the muon:

$$p_\perp = \frac{Bl^2}{8s},\tag{3.1}$$

with the lever arm, l, and the magnetic field B. The deviation or sagitta, s, of the bent trajectory from a straight line is determined from the coordinates of the track in the three layers of drift chambers. The principle of the measurement is shown in figure 3.10. In case of doublets the bending of the trajectory can be determined from the slope of the two p-segments, but the momentum resolution worsens from 2.5% for triplets to 21.3% [59]. The precise and stable positioning of all p-chambers that is required for a high momentum resolution, is guaranteed by an opto-mechanical alignment system [59].

3.8.2 The forward-backward muon chambers

All forward drift chambers consist of three layers (Y,X,W). The W and X layers that measure the r-Φ-coordinate contain 18 and 19 four-wire cells, respectively (figure 3.11). The Y layers, containing 27 four-wire cells, measure the polar angle. As indicated in figure 3.12, there are two complementary regions, S (36°< θ <
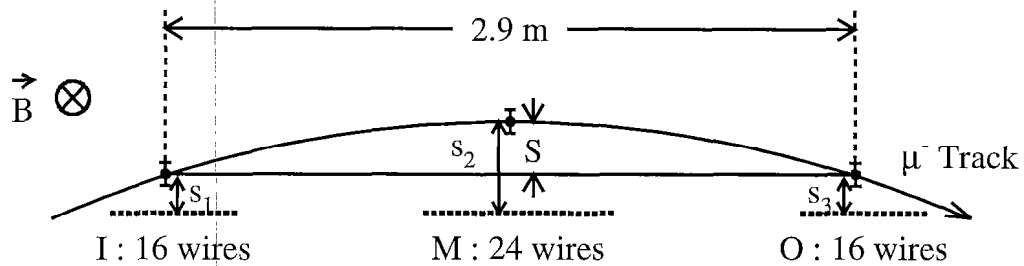
Figure 3.10: Sagitta measurement in the barrel muon chambers.
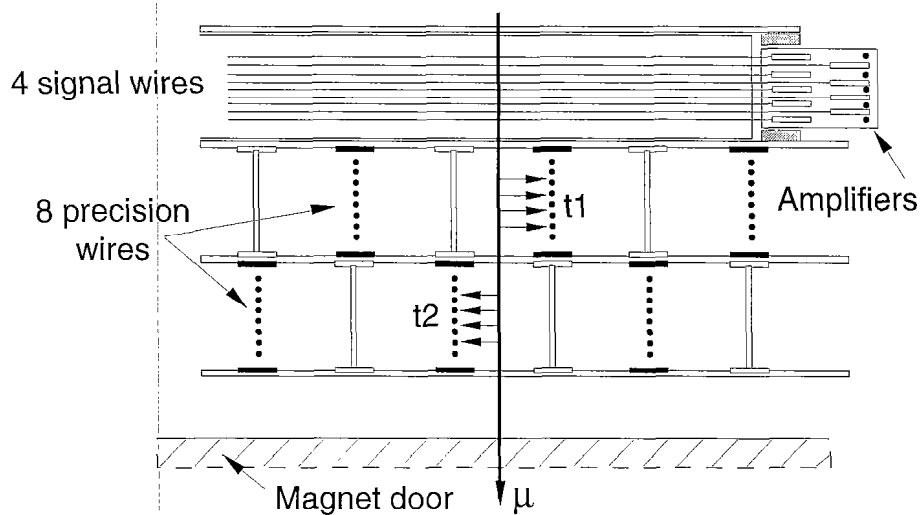
Figure 3.11: A cell of the forward-backward muon chamber.

44°) and T (24°$< \theta < $ 36°). In each region a different method is used to measure the muon momentum.

In the S-region muons are analysed by measuring the bending in the 0.5 T solenoid field with the central chambers MI, MM and the forward FI chamber. The momentum resolution varies from 4% to 23%, depending on the lever arm (i.e. the polar angle) [26]. In the T-region the deflection of the muon trajectory due to the 1.2 T toroidal field in the iron doors is used to measure the muon momentum. Here the momentum resolution is about 30% and is limited by multiple scattering in the 90 cm thick doors. All forward chambers are precisely aligned with respect to each other and with respect to the barrel muon chambers [29].

3.9 Trigger and data acquisition

The task of the trigger system [31] is to decide if an event is interesting from a physics point of view and hence to reduce the amount of data written to tape. It

20
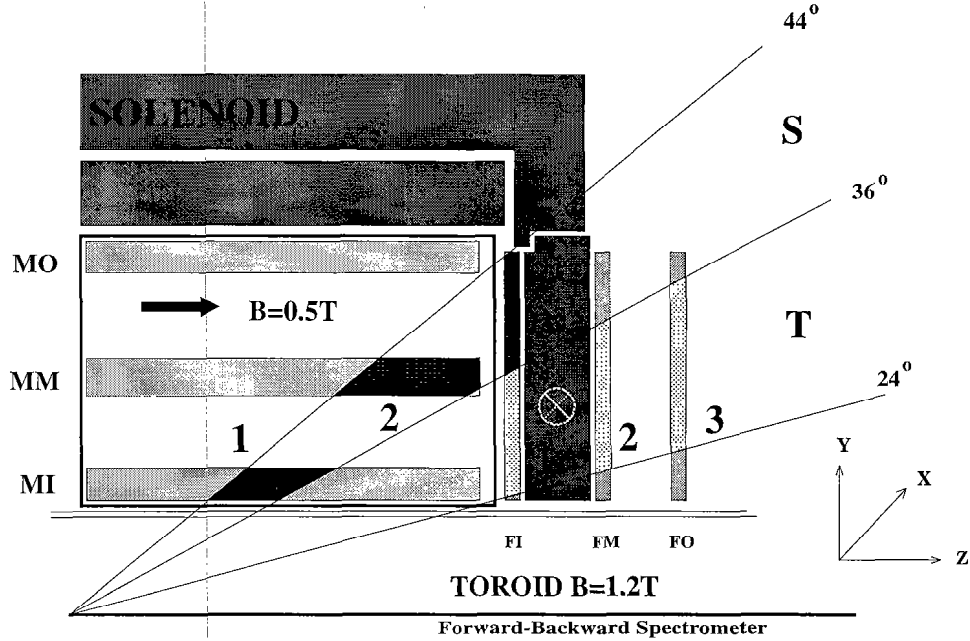
Figure 3.12: Side view of a quarter of the L3 detector and the different polar angular regions.

is a chain of three consecutive levels. The decision has to be made within 22 μs, i.e. between two beam crossings, to prevent dead time in data taking for negative trigger decisions.

The level-1 trigger [32] directly accesses the analog signals of the sub-detectors. The following, independent sub-triggers are important for muon-pair events:

- The Muon Trigger [35] requires a positive decision from at least one out of three sub-triggers:

  a) Single muon trigger: A muon track with a coincidence of all three p-chambers and all four z-chambers in one octant.

  b) Di-muon trigger: A muon track with a coincidence of two p-chambers and two z-chambers. At least two octants should have a track identified and the tracks should satisfy a coplanarity condition.

  c) Small-angle muon trigger: In both hemispheres of the detector a muon track with a coincidence of one p-chamber and two z-chambers has to be present (only in the region between $36° < \theta < 44°$ with respect to the beam axis).

- The TEC Trigger [33] algorithm uses 14 out of 54 wires and sub-divides the r-Φ-plane into 96 Φ-bins. Tracks within one Φ-bin at $\theta > 42°$ must have a transverse momentum $p_t > 600$ MeV. Tracks crossing up to three adjacent Φ-bins have to have a p_t of more than 150 MeV/c. For tracks at $25° < \theta < 42°$ the seven innermost wires are used and a transverse momentum larger than 100 MeV is required.

21

- The Energy Trigger (calorimetric trigger) [34] accepts an event if the sum of the energies deposited in the calorimeters exceeds a pre-defined threshold value. Also a very low energy deposit in the BGO is accepted, provided it accounts almost for the totality of the detected electromagnetic energy and that there is no TEC track in coincidence with this deposit in the r-Φ-projection (single-photon-trigger).

These sub-triggers are combined by a logical OR. Their decisions are uncorrelated since they rely on different sub-detector data. In case the level-1 trigger rejects the event, the detector is ready for the next beam crossing. If the event passes the first level it is sent to the level-2 trigger [37] for further background reduction. The level-3 trigger [38] eventually accesses the completely digitised detector information including a partial reconstruction of the event. It is the last filter to reject background like detector noise or cosmic radiation. Events which successfully pass the level-3 trigger are written onto tape with a rate of about 5 Hz.

3.10   Data reconstruction

The raw data events are reconstructed using the program REL3 [47]. Taking calibration constants into account, the drift times for the chambers, the energy deposits in the calorimeters and the scintillation counter times are calculated. The drift times in the TEC and the muon chambers can be converted to position measurements for the track reconstruction. Adjacent energy measurements in the calorimeters are combined to clusters representing the energy losses of the different observed particles. The time when particle traversed a scintillation counter can be determined from the position information and the time pulse of the scintillator. Eventually tracks are reconstructed based on the information of all sub-detectors.

3.11   Detector simulation

Events are generated according to the prediction of the Standard Model. Interactions with the detector materials are simulated with the program package GEANT [48]. Differences in the comparison of these Monte Carlo events with the data are used to estimate systematic errors in the detector description. Also the detector acceptance and contributions of the background processes are determined from Monte Carlo events.

The following Monte Carlo event generators are used to simulate the various reactions: KORALZ [54] for $e^+e^- \to \mu^+\mu^-(\gamma)$ and $e^+e^- \to \tau^+\tau^-(\gamma)$, DIAG36 [50] for $e^+e^- \to e^+e^-\mu^+\mu^-(\gamma)$, JETSET [51] for $e^+e^- \to q\bar{q}(\gamma)$, KORALW [53] for the process $e^+e^- \to W^+W^-(\gamma)$ and PYTHIA [51] for $e^+e^- \to q\bar{q}(\gamma)$ at $\sqrt{s} > 130$ GeV, for $e^+e^- \to Ze^+e^-(\gamma)$ and $e^+e^- \to ZZ(\gamma)$.

Chapter 4

Event Selection

A muon in the L3 experiment, seen by all sub-detectors, has two hits in the silicon micro vertex detector and a track in the central tracking chamber. The track has ideally 8 hits in the inner TEC and up to 54 hits in the outer TEC depending on the polar angle θ. The muon then leaves a low energy deposition in the electromagnetic calorimeter. The average energy deposition of a muon is about 250 MeV (figure 4.1). A scintillation counter hit is followed by an energy deposition in the hadron calorimeter. The typical energy loss is about 2 GeV (figure 4.1). Finally the muon traverses the muon chamber system, normally hitting three layers in the region of $|\cos\theta|<0.8$ and four layers in the region of $0.8<|\cos\theta|< 0.9$. An example of a muon-pair detected by the L3 experiment is shown in figure 4.2.

4.1   Muon Identification

In this analysis the solid angle is restricted to $|\cos\theta|<0.9$, which is the region covered by the muon spectrometer. A muon can be identified with the muon spectrometer itself or using the central detectors of the L3 experiment only.

The identification of a muon with the muon chamber system requires the reconstruction and matching of the track segments of at least two layers of chambers. It is then possible to determine the direction and momentum of the muon and to track it back to the interaction point. About 90% of the muons are identified in the muon chambers. This number agrees with the expectation since the gaps between the muon chambers represent $\approx$ 7% of the solid angle and for another 3% the muon can, due to non-functioning cells, have at most one reconstructed muon chamber segment.

A muon can also be identified as a *minimum ionising particle* (MIP). A track in the central tracking chamber has to be present. It is combined with energy depositions in the electromagnetic and the hadron calorimeter that are typical for a muon. If present, single muon chamber segments help to identify the particle as a MIP. The background is reduced by applying cuts on the energies deposited in the calorimeters. For both the electromagnetic and hadron calorimeter, the energy depositions in a 24° cone around the MIP candidate are summed. The MIP candidate is assigned to be a muon if the electromagnetic energy is less than 2 GeV and the hadronic energy less than 7 GeV.
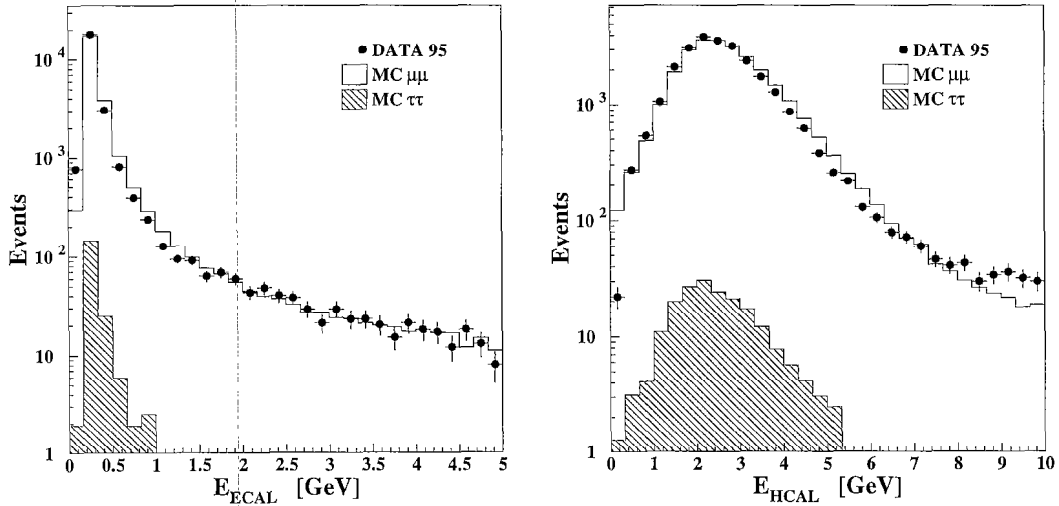
Figure 4.1: The energy deposited by a muon in the electromagnetic calorimeter and in the hadron calorimeter. Only muons of the MM sample whose selection is not based on calorimetric information are shown.

The selected $e^+e^- \to \mu^+\mu^-(\gamma)$ events are divided into three event samples that are treated differently in the analysis (see also table B.1):

- MM sample: two reconstructed muon chamber tracks ($\approx 82\%$)

- MX sample: one reconstructed muon chamber track and one MIP ($\approx 12\%$)

- XX sample: two minimum ionising particles ($\approx 6\%$)

4.2   Muon-pair selection

Events from the muon-pair production $e^+e^- \to \mu^+\mu^-(\gamma)$ have to be separated from other processes with muons in the final state. These background processes are:

- $e^+e^- \to \tau^+\tau^-(\gamma)$,

- $e^+e^- \to e^+e^-\mu^+\mu^-(\gamma)$,

- $e^+e^- \to q\bar{q}(\gamma)$,

- Cosmic muons.

Feynman graphs for the muon-pair production and the most important background processes are shown in figure 4.3. The contamination from the different background processes is determined from Monte Carlo simulations. For muon-pair production at center-of-mass energies, E_{cms}, above the Z resonance, additional background processes have to be taken into account:

- $e^+e^- \to W^+W^-(\gamma)$,
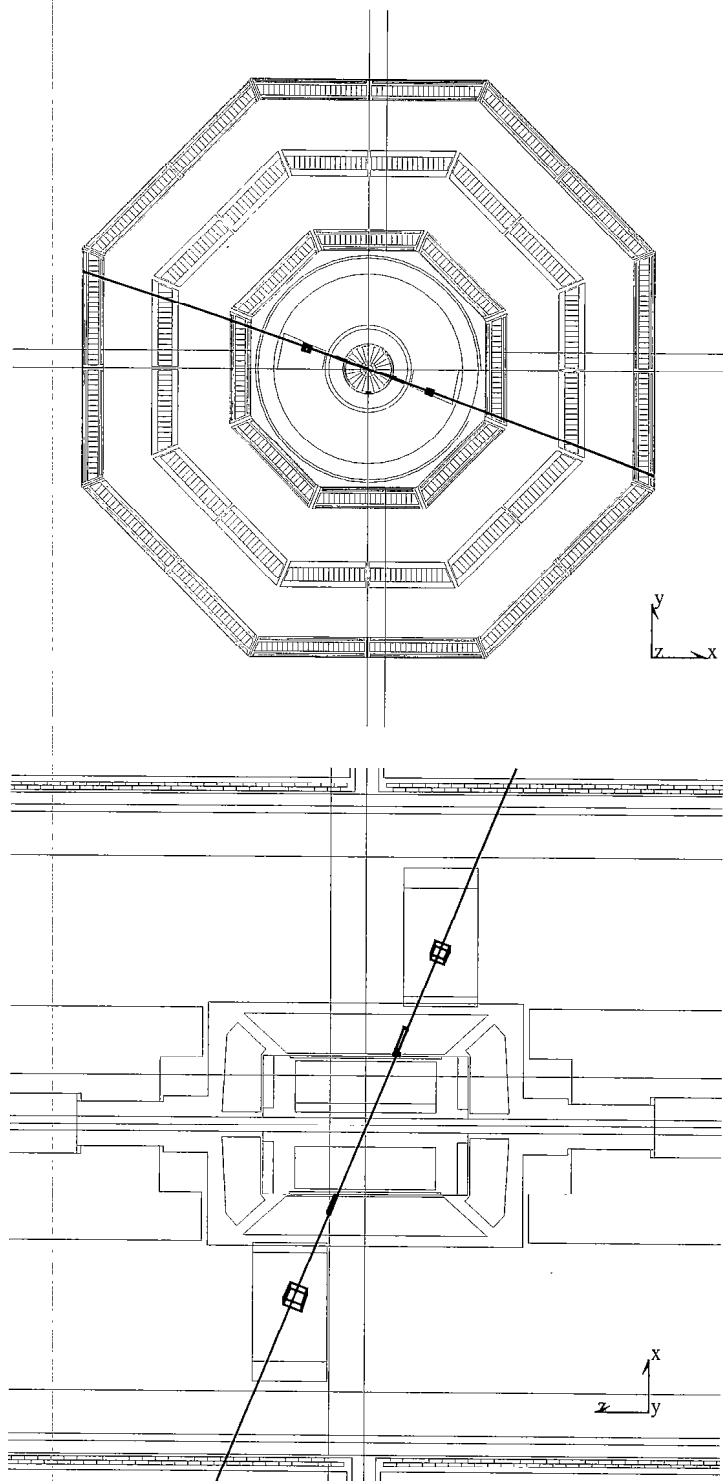
Figure 4.2: The front view of the L3 detector (top) shows two muons both traversing all three layers of muon chambers. The side view (bottom) magnifies the central part. Coming from the interaction point in the center the muons leave a track in the TEC, energy depositions in the electromagnetic and hadron calorimeters and finally reach the muon chambers.
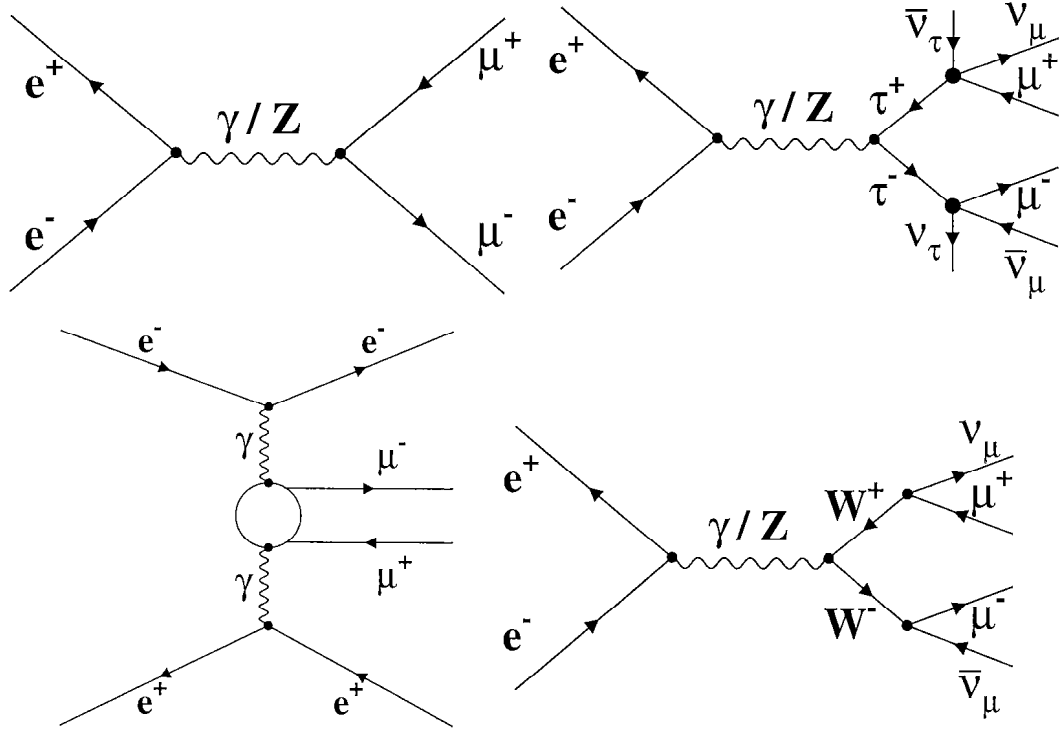
Figure 4.3: The muon-pair production $e^+e^- \to \mu^+\mu^-(\gamma)$ (upper left) and the background processes $e^+e^- \to \tau^+\tau^-(\gamma)$ (upper right), $e^+e^- \to e^+e^-\mu^+\mu^-(\gamma)$ (lower left) and $e^+e^- \to W^+W^-(\gamma)$ (lower right). For the τ-pair and W-pair production, an example containing muons is shown since these events represent the majority of the respective background.

- $e^+e^- \to Ze^+e^-(\gamma)$,

- $e^+e^- \to ZZ(\gamma)$,

- $e^+e^- \to e^+e^-\tau^+\tau^-(\gamma)$.

Most of the background can be removed by applying cuts on various quantities of the muon-pair. All cuts are explained in detail in sections 4.2.1 and 4.2.2. Figures 4.4 through 4.11 show the distributions of the cut quantities with all other selection cuts always applied. The following overview lists the quantities the selection is based on, the cuts and the background they reduce:

quantity	cut	background
scintillator time	one $t_{\text{scin}} < 5$ ns	cosmic muons
r-Φ-dca	one $d_\perp < 1$ mm	cosmic muons
acollinearity	$\xi_{\text{MM}} < 90°$, $\xi_{\text{MX}} < 40°$, $\xi_{\text{XX}} < 5°$	all background
muon momentum (MM,MX)	$p_{\text{max}} > \frac{2}{3}E_{\text{beam}}$	all background
transverse momentum (XX)	two $p_t > 3$ GeV	ee $\to$ eeff
multiplicity	clusters < 16	$e^+e^- \to q\bar{q}(\gamma)$

26
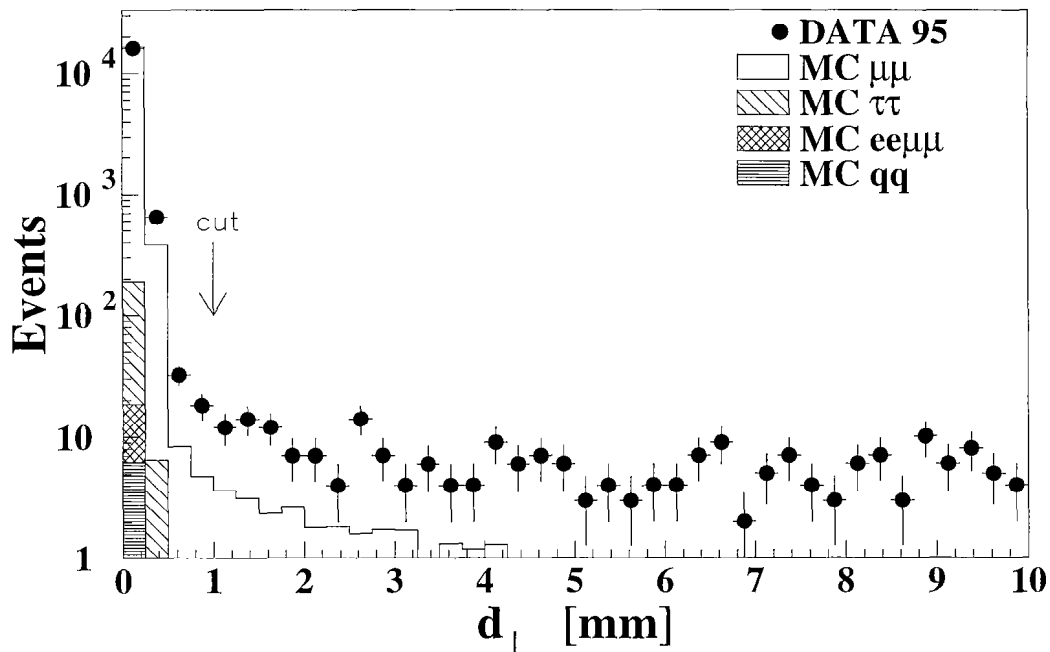
Figure 4.4: Distribution of the distance of closest approach, $d_\perp$, in the r-Φ-plane.

4.2.1 Cosmic muon rejection

Events with muons from cosmic radiation (*cosmics*) can be accepted as muon-pair events. Their rate is constant with time and completely independent of the time and location of the beam collisions. These events are rejected by requiring one of the two muons to have a distance of closest approach to the beam axis in the r-Φ-plane, $d_\perp$, of less than 1 mm. Figure 4.4 shows the minimum $d_\perp$ for selected muon-pair events. The tail of the distribution represents a constant rate of cosmics. In addition at least one scintillator counter time has to be within a 5 ns window around the beam crossing (figure 4.5).

A control sample of cosmic muons is created by selecting all the events of the 1995 data with a distance of closest approach to the beam axis in the r-Φ-plane of 5 mm $< d_\perp <$ 50 mm and a minimum scintillator counter time of 10 ns $< t_{\rm scin} <$ 50 ns around the beam crossing. The sample is used as a Monte Carlo substitute for cosmic muons.

4.2.2 Background reduction

Muon-pair production creates a two-particle final state up to radiative corrections. Due to energy and momentum conservation both muons are expected to have $E_\mu \approx$ $E_{\rm beam}$ since most additional photons have low energy. Background processes like tau-pair production contain muons with lower momenta. The major contribution arises from events where both taus decay into muons $\tau \rightarrow \mu \nu_\mu \nu_\tau$ (figure 4.3). A large fraction of the energy is carried away by the neutrinos and therefore undetectable. Requiring at least $\frac{2}{3}E_{\rm beam}$ for the momentum of one of the muons
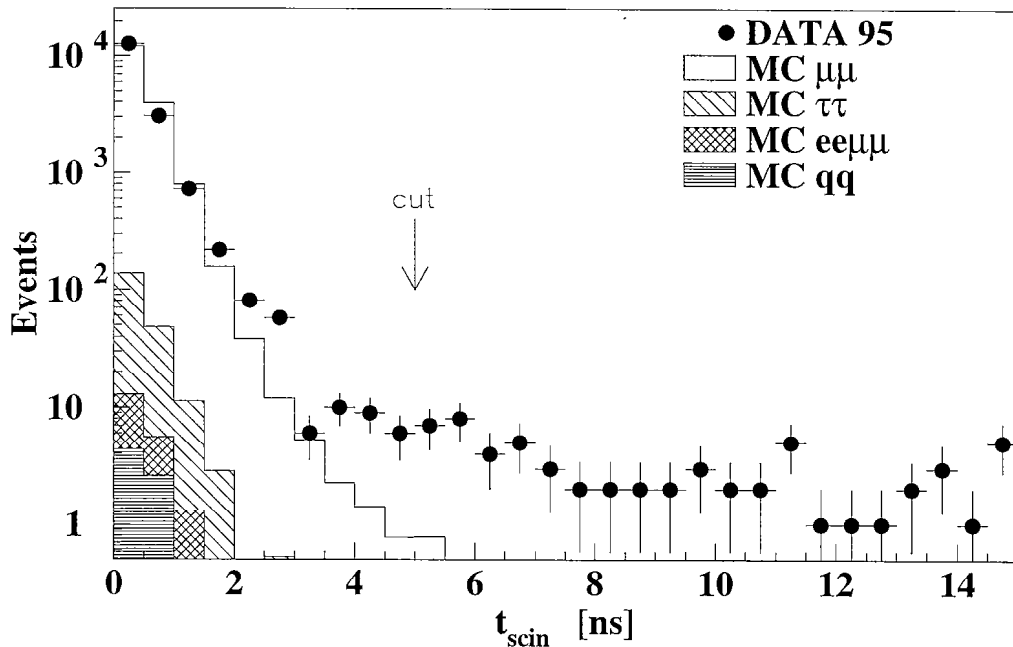
Figure 4.5: Distribution of the minimum scintillation counter time.

in the MM sample and for the muon with a reconstructed muon chamber track in the MX sample permits to separate most of the background from the signal. Figure 4.6 shows the distribution of the maximum momentum of the muons of the MM and MX sample normalised to the beam energy.

Tau-pair events have a different acollinearity[1] than muon-pair events due to the neutrino production in τ-decay. Additional background can thus be rejected by requiring the acollinearity to be less than 90° for events in the MM sample (figure 4.7). The TEC trigger has an implicit restriction on the acollinearity since an event is only accepted if there is a signal from two close to opposite sectors. Therefore a cut on the acollinearity of 40° is applied for events in the MX sample (figure 4.8).

In the XX sample the background from four-fermion final states, ee $\rightarrow$ ee$\bar{\text{ff}}$, can be reduced by requiring both tracks to have a transverse momentum of at least 3 GeV in the central tracking chamber (figure 4.9). The magnification of the range $0 < p_t < 6$ GeV shows that additional background is present for $p_t < 1$ GeV. This has no influence on the cross section measurement since the cut at 3 GeV is sufficiently far away (section 6.5). The remaining background from tau-pair production is rejected by an acollinearity cut at 5°. The acollinearity distribution of the XX sample is shown in figure 4.10.

It is not sufficient to separate the background originating from hadron-pair production and muon pairs by cutting on the momenta of the muons and the acollinearity of the event. Their rejection can be enhanced by introducing a cut on the multiplicity of the event. Figure 4.11 shows the number of energy

---

[1]The acollinearity, ξ, is the difference between the angle between the two muons and 180°.
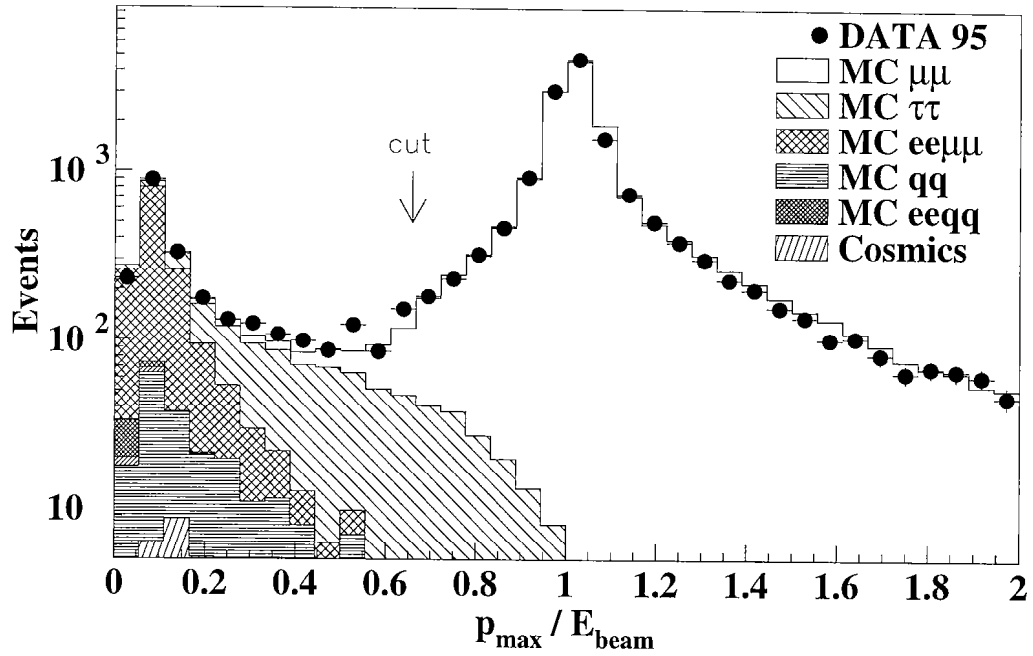
Figure 4.6: Distribution of the maximum muon momentum for the MM and MX samples normalised to the beam energy.
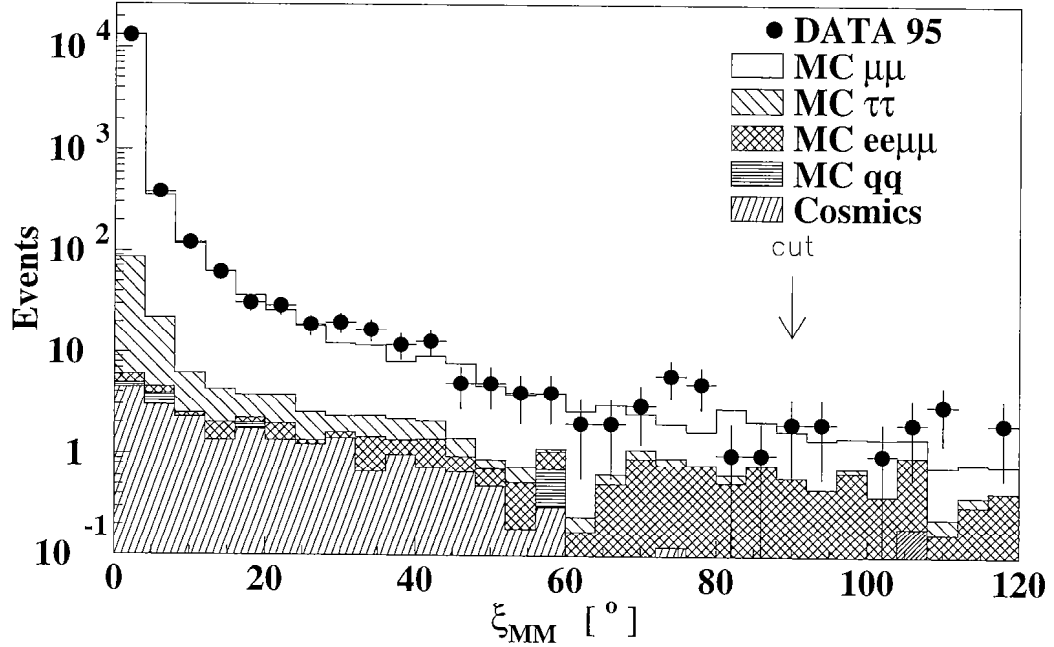
Figure 4.7: The acollinearity distribution for the MM sample.
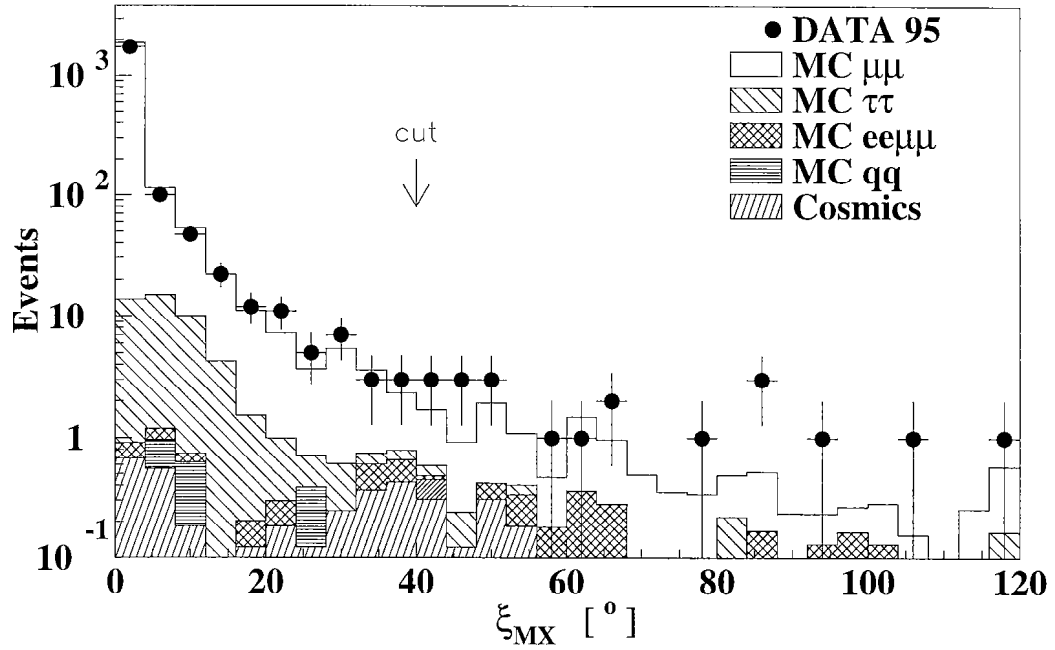
Figure 4.8: The acollinearity distribution for the MX sample.
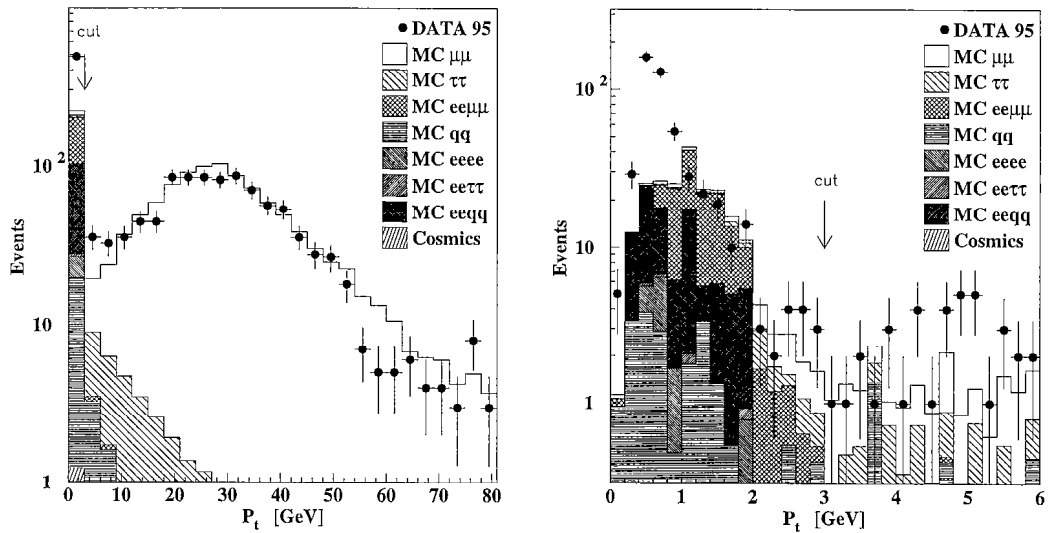
Figure 4.9: Distribution of the minimum transverse momentum of the TEC track for the XX sample. The right plot magnifies the range around the cut. The cut is sufficiently far away from the region below 1 GeV where additional background is present.
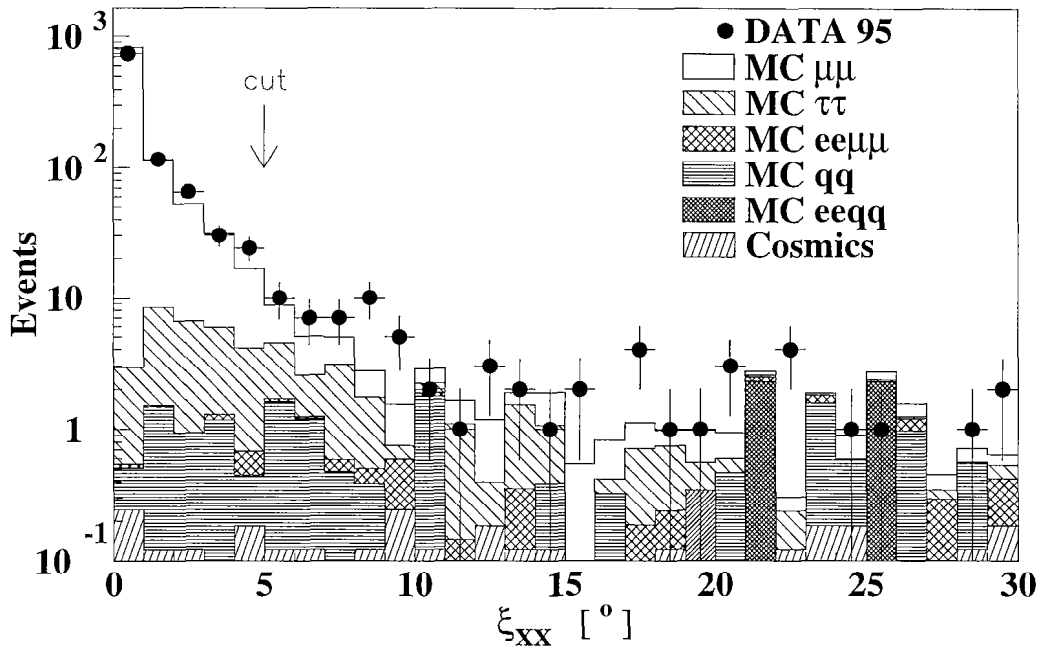
Figure 4.10: The acollinearity distribution for the XX sample.

deposition clusters in the calorimeters per event.

Figure 4.12 shows the distribution of the polar angles $\cos\theta$ of the selected muons and their azimuthal angles Φ within a muon chamber sector. The gap of the muon spectrometer in θ is located at $\cos\theta=0$. There also are gaps between the different chambers in Φ. The angular distributions show clearly how in these regions the muons are identified as minimal ionising particles and thus contribute to the MX and XX samples.

For all distributions there is good agreement between data and Monte Carlo prediction for both signal and background processes. The bulk of the background, including muons from cosmic radiation, is successfully rejected.

4.3 Muon-pair production at $\sqrt{s} > 100$ GeV

4.3.1 Effective center-of-mass energy

In 1995 LEP was operated for the first time at center-of-mass energies, $\sqrt{s}$, above 100 GeV. For a substantial fraction of the muon-pair events, initial-state photons are emitted. They lower the initial center-of-mass energy to an effective center-of-mass energy of the annihilation process, $\sqrt{s'}$. When $\sqrt{s'}$ is close to the Z mass, m_Z, the events are classified as radiative returns to the Z. A cut on $\sqrt{s'}$ allows a separation between events at high effective center-of-mass energies, *high energy events*, and radiative returns to the Z.

Tau-pairs cannot be produced at an effective center-of-mass energy $\sqrt{s'} < 2\ m_\tau$ (≈ 3.6 GeV). To define a consistent phase space for all lepton-pair production
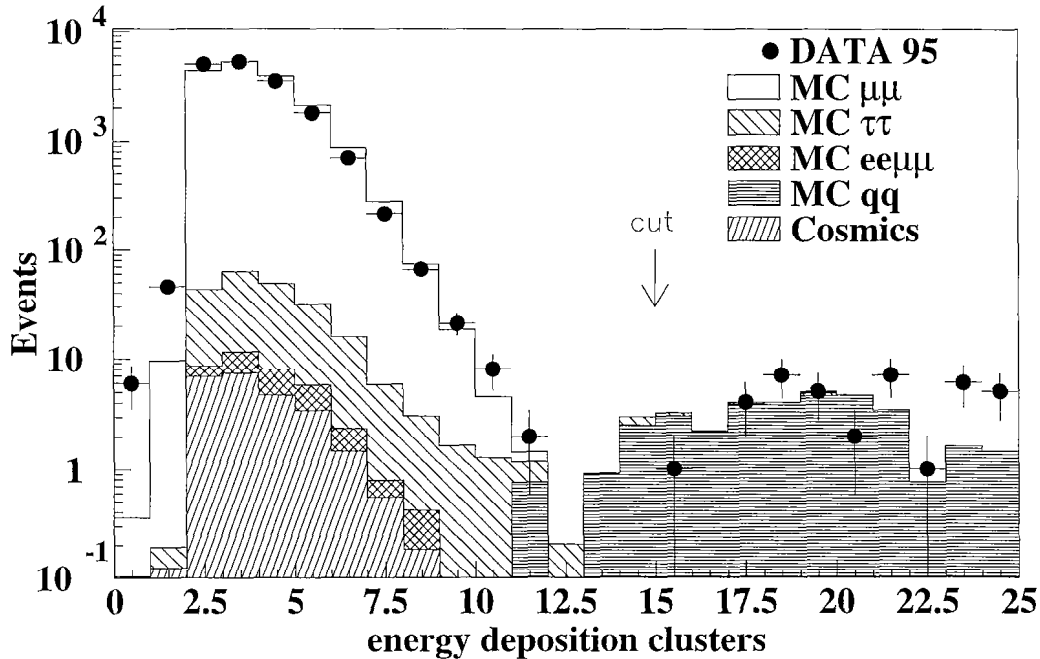
Figure 4.11: The number of energy depositions in the calorimeters.

channels and to reduce uncertainties on radiative corrections in extrapolating to low $\sqrt{s'}$ values, the effective center-of-mass energy, $\sqrt{s'}$, in the total event sample is required to be larger than $0.1\sqrt{s}$. The high energy sample is defined by requiring $\sqrt{s'}>0.85\sqrt{s}$. Assuming the emission of a single initial state photon, γ_{ISR}, and using its energy, E_γ, the $\sqrt{s'}$ value is given by:

$$s' = s - 2E_\gamma\sqrt{s}. \tag{4.1}$$

If the photon is found in the detector it is required to have an energy, E_γ, larger than 15 GeV in the electromagnetic calorimeter and an angular separation to the nearest muon of more than 10°. If it is not detected, the photon is assumed to be emitted along the beam axis and its energy is calculated from the polar angles, θ_1 and θ_2, of the outgoing muons:

$$E_\gamma = \sqrt{s}\frac{|\sin(\theta_1 + \theta_2)|}{\sin\theta_1 + \sin\theta_2 + |\sin(\theta_1 + \theta_2)|}. \tag{4.2}$$

A Monte Carlo study confirms the assumption of only one initial state photon. The fractions of events with zero, one or more ISR photons found in the detector are given in table 4.1. Two or more ISR photons were found for only less than 0.5% of the events. In these cases the higher energy photon is used for the determination of $\sqrt{s'}$. The impact of a possible wrong determination of $\sqrt{s'}$ for these events on the cross section and asymmetry measurement is negligible, most of all regarding the number of selected events (section 6.4). Figure 4.14 shows $\sqrt{s'}$ for 130 GeV$\leq\sqrt{s}\leq$183 GeV. The peaks at 91 GeV are due to muon-pairs produced at $\sqrt{s'}\approx m_Z$. It can be seen that for all energy points the high energy sample ($\sqrt{s'}>0.85\sqrt{s}$) comprises about 50% of the events.

32
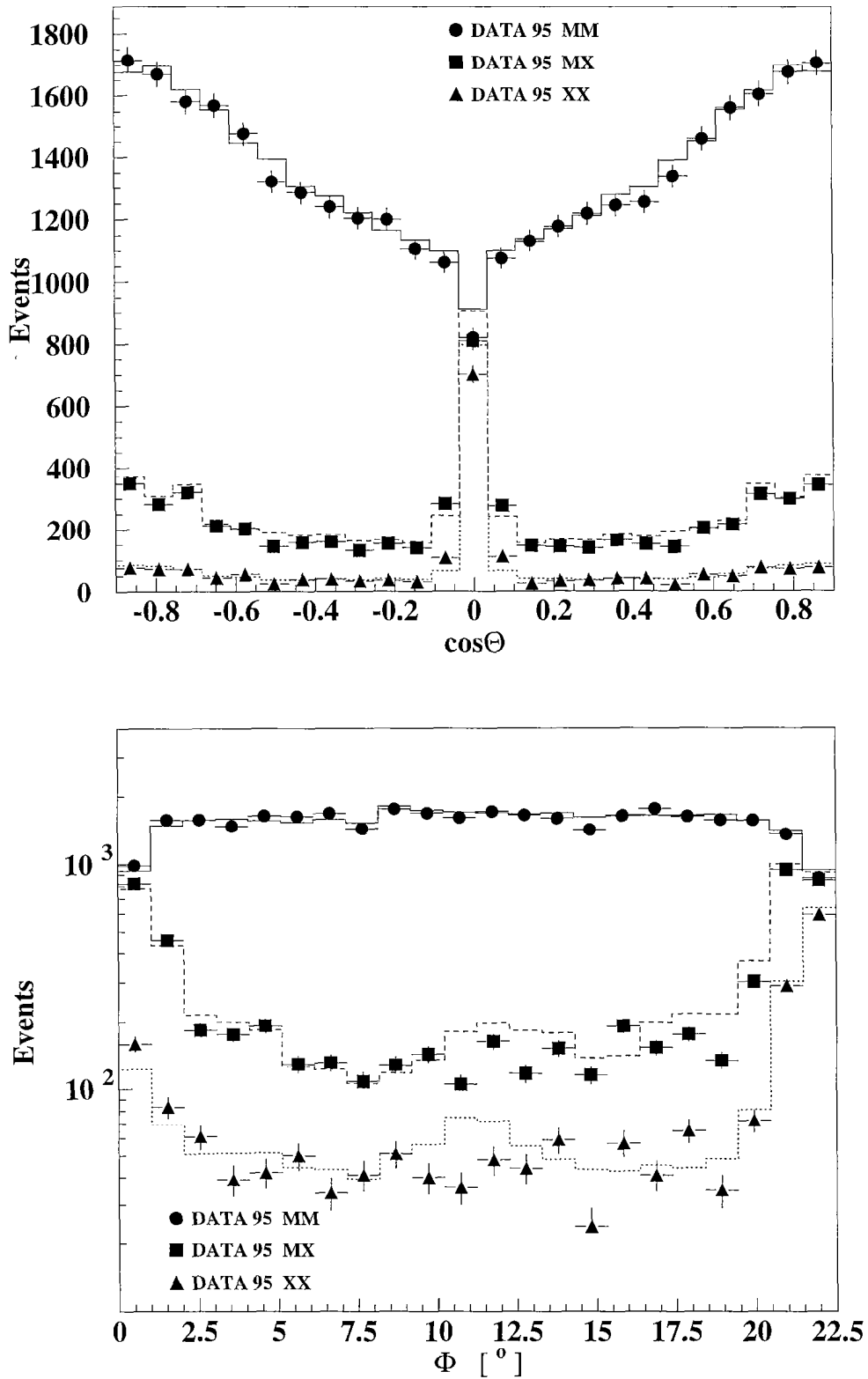
Figure 4.12: The cos θ- (upper) and the Φ-distribution per half-octant (lower) of the selected muons. The lines are the Monte Carlo simulation for the MM (solid), the MX (dashed) and the XX (dotted) samples.

33
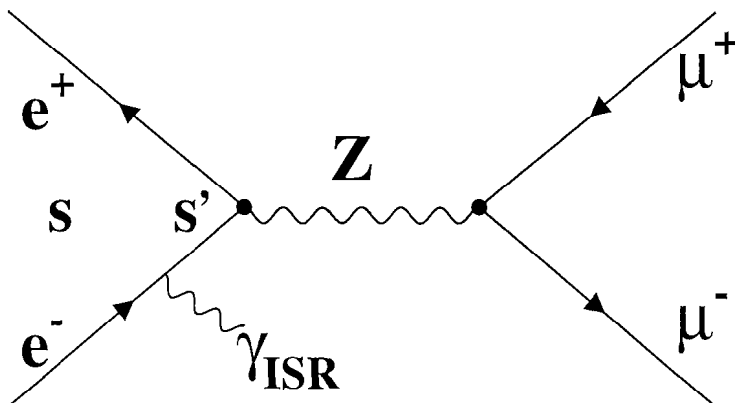
Figure 4.13: Feynman graph for the muon-pair production with an initial state photon. The muons are produced at a lower effective center-of-mass energy, $\sqrt{s'}$.

$\sqrt{s}$ [GeV]	no γ_{ISR} [%]	1 γ_{ISR} [%]	2 γ_{ISR} [%]	3 γ_{ISR} [%]
130.0	90.8±1.0	8.9±0.3	0.2±0.1	0.04±0.02
135.9	90.1±1.0	9.6±0.3	0.3±0.1	0.00±0.01
161.3	90.2±0.7	9.5±0.2	0.3±0.1	0.01±0.01
172.1	90.6±0.7	9.0±0.2	0.4±0.1	0.01±0.01
182.7	92.4±0.7	7.3±0.2	0.3±0.1	0.00±0.01

Table 4.1: The fractions of events with zero, one or more ISR photons found in the detector determined from the Monte Carlo simulation.
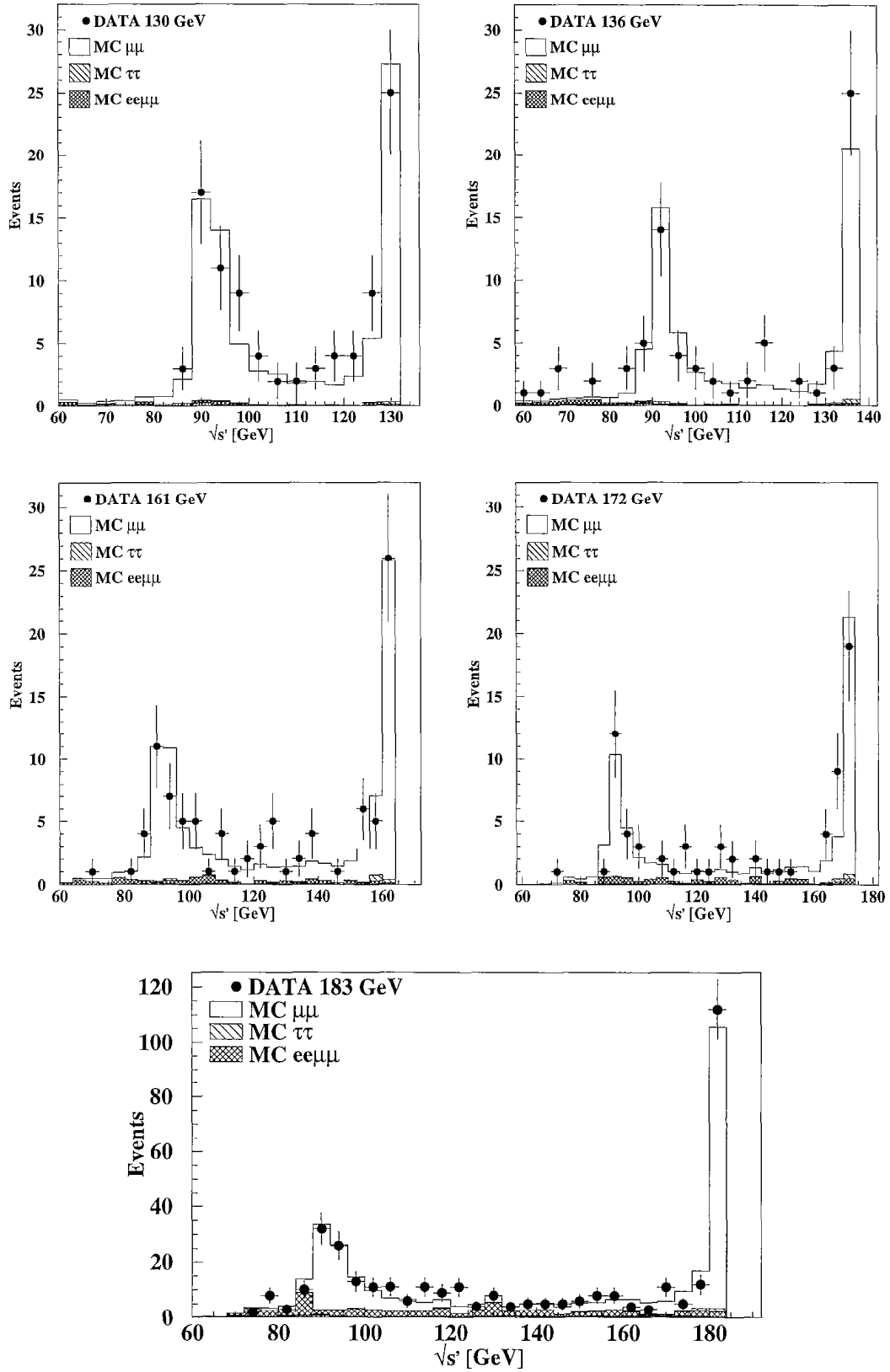
Figure 4.14: The effective center-of-mass energies, $\sqrt{s'}$, for the data taken at 130 GeV$\leq\sqrt{s}\leq$183 GeV. The respective peaks at 91 GeV represent the radiative returns to the Z with $\sqrt{s'}\approx m_Z$.

4.3.2 Event selection

For muon-pairs produced at $\sqrt{s'}>0.85\sqrt{s}$, the event topology is similar to that for events at $\sqrt{s}\approx m_Z$. Radiative returns to the Z emit high-energy ISR photons, mostly along the beam axis. An example of a muon-pair with an initial state photon in the L3 detector, produced at $\sqrt{s}=161$ GeV, is shown in figure 4.15. The ISR photon, that causes the acollinearity of the event, is clearly visible. Figure 4.16 shows the acollinearity for events of the MM sample at $\sqrt{s}=183$ GeV. Muon-pairs with $\sqrt{s'}\approx\sqrt{s}$ have an acollinearity ξ <10° while events produced at $\sqrt{s'}\approx m_Z$ peak at ξ=70°.

For center-of-mass energies above $\sqrt{s}=100$ GeV events of the XX category are no longer considered. Their contribution to the number of selected events is negligible since even the radiative events are already rejected by the cut on the acollinearity ξ <5° (section 4.2.2). The event selection follows the selection for the data of 1995 with minor modifications. They are explained in the following section.

4.3.3 Background rejection

The lower cut on the highest momentum measured in the muon chambers, p_{max}, is set to a fixed value of 35 GeV to ensure high acceptance for events with hard ISR photons. Figure 4.17 shows p_{max} normalised to the beam energy, E_{beam}, for $\sqrt{s}=183$ GeV.

The number of muons from cosmic radiation is constant in time. Due to the lower cross section for muon-pair production at higher energies, the fraction of cosmic events among the selected events is increased. The minimum distance of closest approach is required to be less than 0.5 mm to further reduce the background from cosmic radiation in the final sample. The minimum scintillation counter time, t_{scin}, has to be less than 3.5 ns. In addition, if both muons in the event have a good scintillation or RPC counter hit, the difference between the upper and lower counter is calculated, t_{top}- t_{bottom}. The expected time-of-flight for a cosmic muon is determined from the geometrical position of the two counters. If this expected time-of-flight and the difference in time calculated from the two counters agree within 2 ns the event is identified as an event originating from cosmic radiation and thus rejected (figure 4.18).

Again there is good agreement in all distributions between data and Monte Carlo prediction for both signal and background processes.
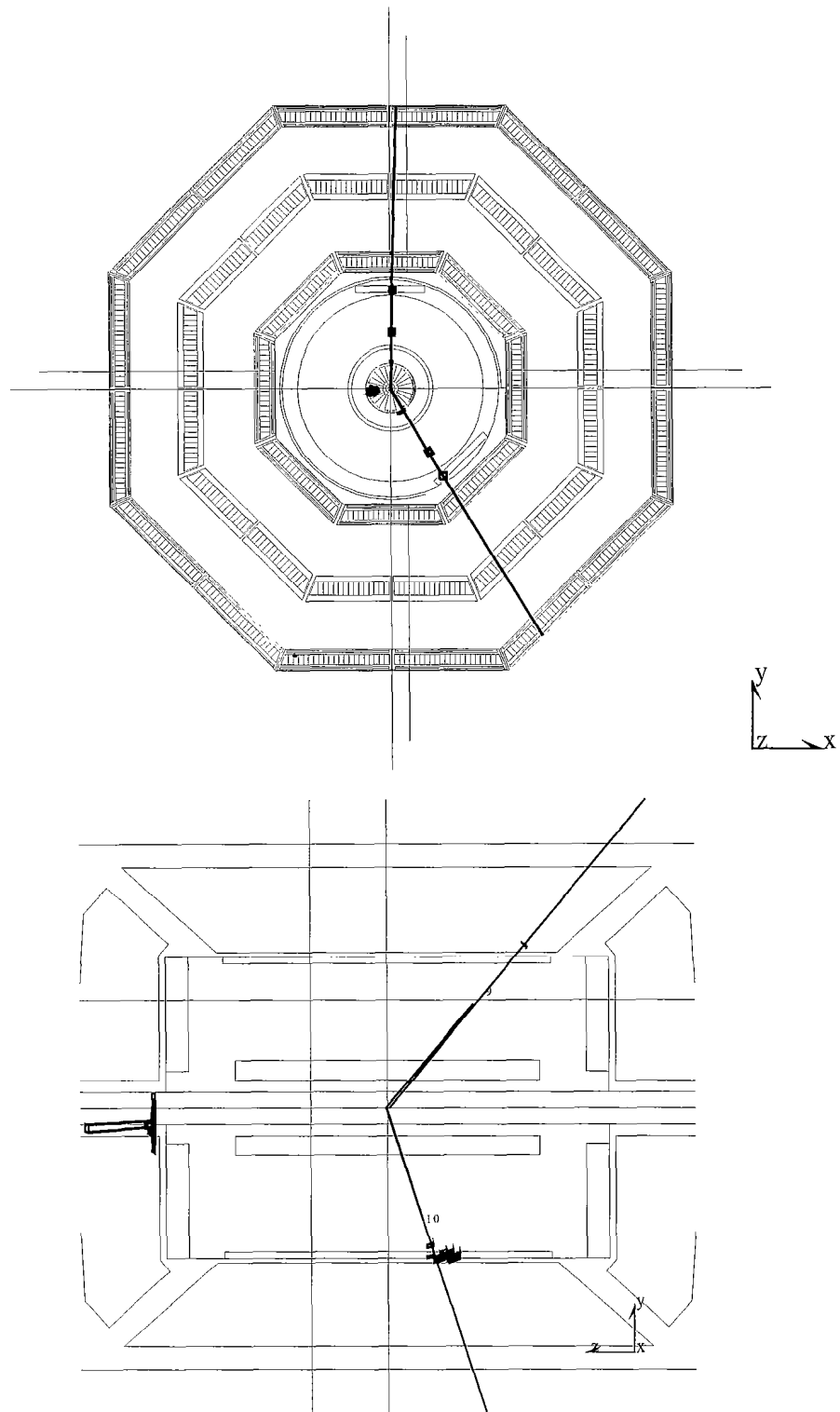
Figure 4.15: The front view of the L3 detector (top) shows two muons traversing the muon chambers. An emitted initial state photon causes the acollinearity of the two muons. The side view (bottom) magnifies the electromagnetic calorimeter and the inner tracking chamber. The ISR photon is clearly visible on the left side. This muon-pair was produced at $\sqrt{s}$=161 GeV.
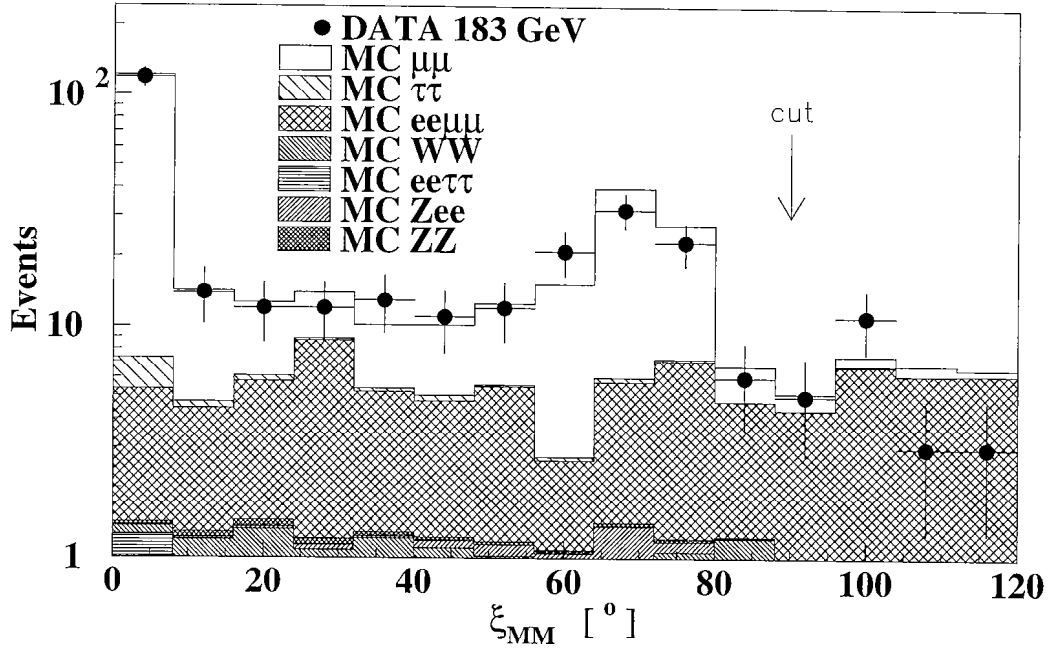
Figure 4.16: The acollinearity distribution for the MM sample at $\sqrt{s}$=183 GeV. The two peaks at 0° and 70° are due to muon-pairs produced at $\sqrt{s'}\approx\sqrt{s}$ and $\sqrt{s'}\approx m_Z$, respectively.
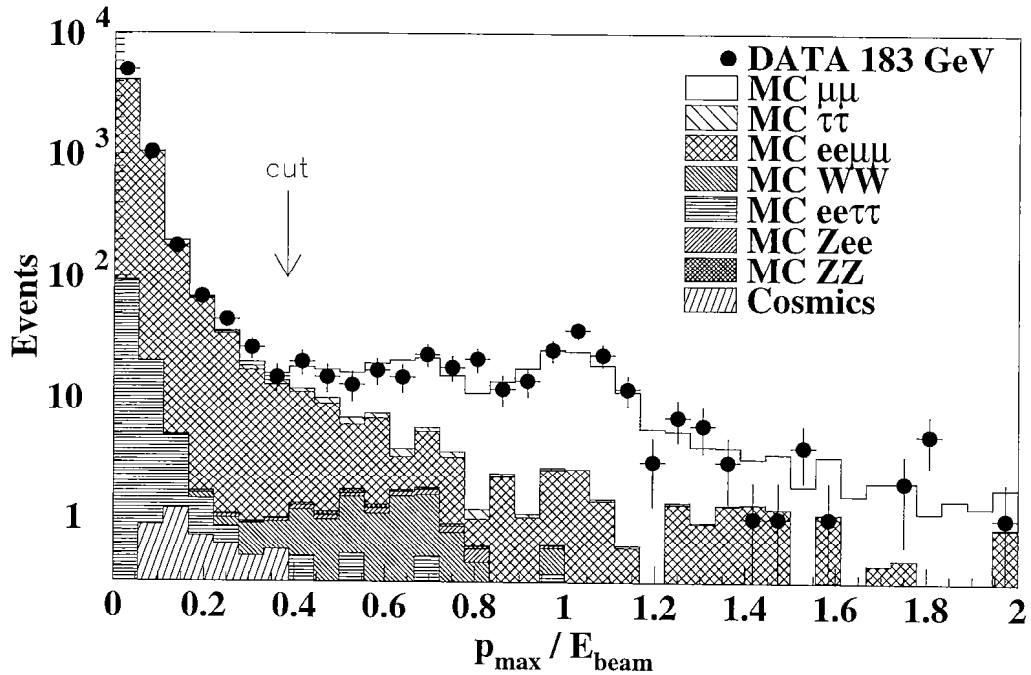
Figure 4.17: The highest momentum measured in the muon chambers, p_{max}, normalised to the beam energy, E_{beam}, for $\sqrt{s}$=183 GeV. The peaks at 1.0 and at 0.7 ($\sqrt{s'}\approx m_Z$) can be distinguished.
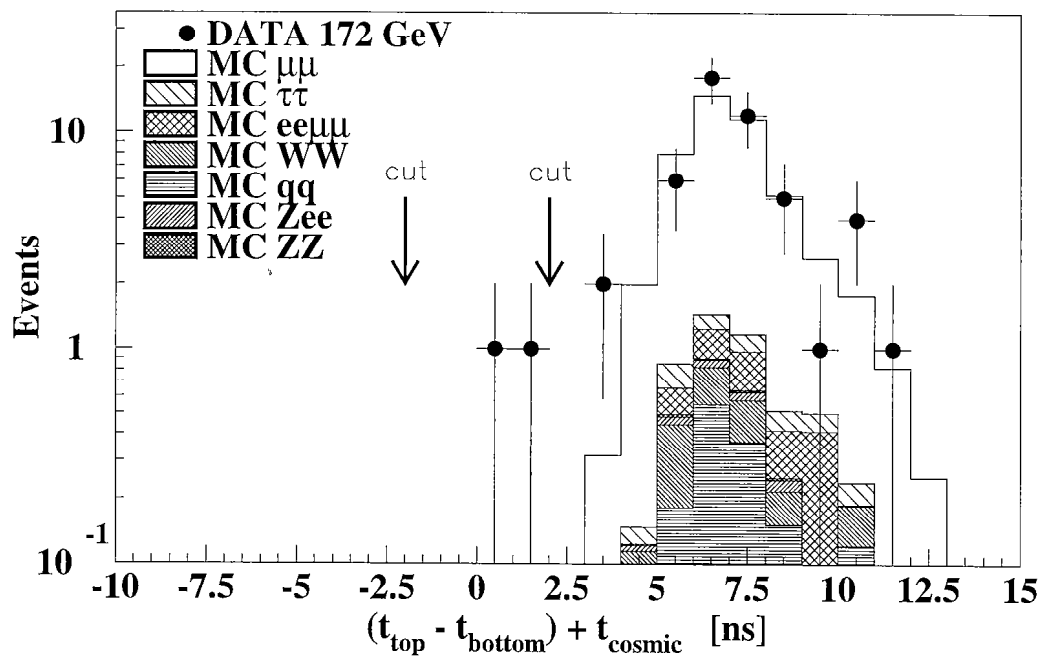
Figure 4.18: The difference between the upper and the lower scintillation counter or RPC added to the expected time-of-flight for a cosmic muon. If both times agree within 2 ns, the event is identified as a cosmic muon and rejected.

Chapter 5

Detector efficiencies

The chapter presents the efficiencies of the muon chambers and other sub-detectors that are important for the muon-pair analysis. The task of the analysis is to determine cross sections and forward-backward asymmetries to such a precision that the statistical error dominates the systematic uncertainties. These systematic uncertainties, described in detail in section 6.5, contain contributions from the detector acceptance and trigger efficiency. Thus it is important to correctly simulate detector inefficiencies. The following sections investigate the efficiencies of the muon chambers, central tracking chamber, scintillators and RPCs as well as the efficiency of the backup (MIP) selection. They compare the efficiencies for data with the Monte Carlo simulation and explain the techniques that are used. Very important is also the quality of the muon momentum reconstruction since most of the background is rejected by the cut on the maximum muon momentum (section 4.2.2). The last section describes the determination of the trigger efficiency.

5.1 Muon chamber efficiency

More than 90% of the muon-pairs are selected using criteria based on the muon chamber information. Cells disconnected from high voltage and their periods of disconnection are taken into account in the Monte Carlo simulation. In case several chambers are non-functional at the same time, the period is excluded from the analysis.

A muon that passes a non-functional cell can still be detected and possibly selected. The failure of a p-chamber cell in the central part of the detector results in a reconstruction with only two track segments. Only if there is a second non-functional cell in another layer on the muon trajectory, two p-chamber segments are lost and the muon track can not be reconstructed. In this case, the muon can still be detected as a MIP. However, the efficiency of the MIP selection is slightly lower than the efficiency for the selection using the muon chamber information (section 5.3).

The efficiency of the muon chambers is determined using a sub-sample of the selected events. Applying the MIP selection of the XX sample to all events and requiring the TEC trigger to be present, one obtains a sample independent of muon chambers and muon trigger. The muon is then tracked through the muon
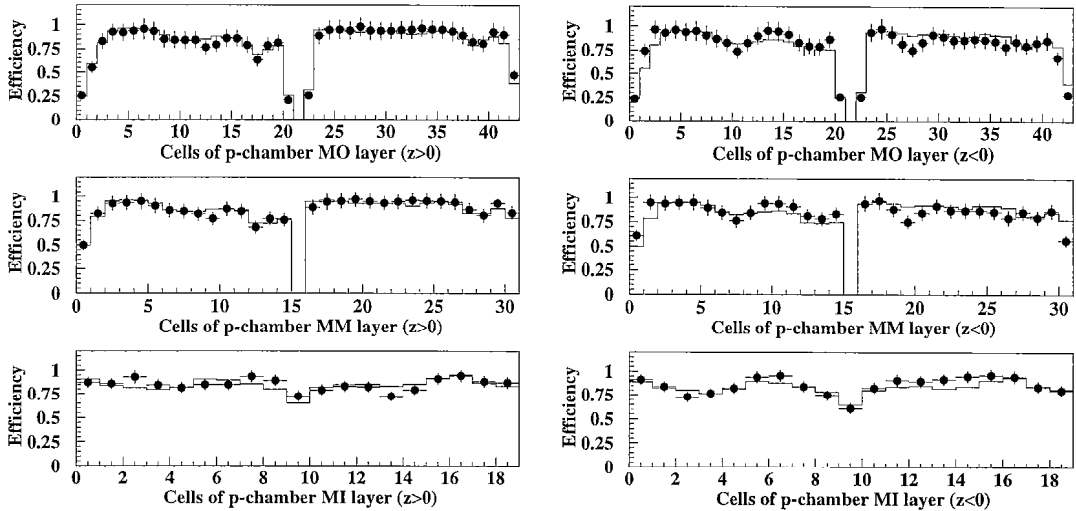
Figure 5.1: The efficiency of the muon p-chambers for 1995 data (dots) and Monte Carlo simulation (solid line). The efficiency shown is the average over all octants in the forward ($z > 0$) and backward ($z < 0$) directions. The gaps between the two MO and two MM chambers per octant are clearly visible.

chambers. If there is no muon chamber segment found in one or more layers, the missing cell is determined from the Φ-angle and considered as inefficient. The efficiency of the p-chambers combined for octants in the forward ($z > 0$) and backward ($z < 0$) directions is shown in figure 5.1. The Monte Carlo simulation describes the data well. The gaps between the two MO and two MM chambers per octant are clearly visible.

Table 5.1 compares the acceptance of the different layers of muon chambers for data with the Monte Carlo simulation. Only reconstructed muon tracks were used to determine the acceptance of the muon chambers. Thus the reconstruction efficiency for muon tracks is included in the acceptance measurement. The acceptance ϵ was determined by counting for each layer the number of reconstructed segments, N_{rec}, and the number of segments which are missing, N_{miss}, but should have been there according to geometry:

$$\epsilon = \frac{N_{rec}}{N_{rec} + N_{miss}}. \tag{5.1}$$

The efficiency of the p-chambers is good and always above 90%. The efficiencies of the z-chambers are not well simulated. The lack of one z-chamber segment leads to a less precise determination of the polar angle of the muon. In this case the measurement of another sub-detector is taken to determine the polar angle. Thus the large discrepancy between data and Monte Carlo simulation does not affect the selection. The small differences between data and the Monte Carlo simulation for the forward-backward chambers have almost no impact on the selection since for the reconstruction of a muon track not all layers have to be hit. The remaining difference contributes to the systematic error (section 6.3). Figure 5.2 shows the occupancy of the forward-backward muon chamber cells for

Layer	Data [%]	MC [%]
MI	90.8±0.2	90.1±0.2
MM	91.8±0.2	91.0±0.2
MO	93.9±0.2	92.8±0.2
Z(MI)	76.7±0.3	87.4±0.2
Z(MO)	69.3±0.4	82.7±0.3
FI-Y	92.7±0.4	96.2±0.3
FI-X	87.8±0.5	89.8±0.4
FI-W	84.7±0.5	89.1±0.4
FM-Y	87.8±0.8	93.9±0.5
FM-X	81.9±0.9	84.7±0.8
FM-W	82.9±0.9	85.2±0.8
FO-Y	82.9±0.9	85.2±0.8
FO-X	81.9±0.9	84.7±0.8
FO-W	87.8±0.8	93.9±0.5

Table 5.1: The efficiencies of the different layers of muon chambers. The measurement was obtained using a selection independent of the muon chambers.

all different kinds of layers in the forward ($z > 0$) and backward ($z < 0$) directions. There is a good agreement between data and Monte Carlo simulation.

5.2 Muon momentum reconstruction

The bending of the trajectory within the muon chambers is used to determine the transverse momentum, p_t, of the muon. It is calculated from the deviation or sagitta, s, of the bent trajectory from a straight line according to equation 3.1. Since the sagitta is a quantity directly measured in the detector, its distribution is expected to be a Gaussian around its true value:

$$\Delta \left(\frac{1}{p_t} \right) \propto \Delta s = const. \tag{5.2}$$

To obtain the momentum at the vertex, the average energy loss of the muon due to detector materials is added to the momentum measured in the muon chambers. This energy loss is determined with the detector simulation program GEANT[48]. The average correction is 2.2 GeV with an average accuracy of 10% .

For muon-pair events without high-energy photons the momenta of the two muons are each expected to be close to the beam energy. Thus the resolution of $1/p_t$ can be determined by comparing the transverse momentum $p_\mu \sin \theta_\mu$ of the muon with its expected value $E_{beam} \sin \theta_\mu$. Figure 5.3 shows the muon momenta resolutions, obtained with a Gaussian fit, for triplets in the three different regions of the muon spectrometer. They are based on a sample of muon-pairs with an acollinearity smaller than 1° and an electromagnetic energy of less than 1 GeV. These cuts reduce the number of events with photon radiation, thus the assumption that the muon momentum is close to the beam energy is valid. The momentum resolution
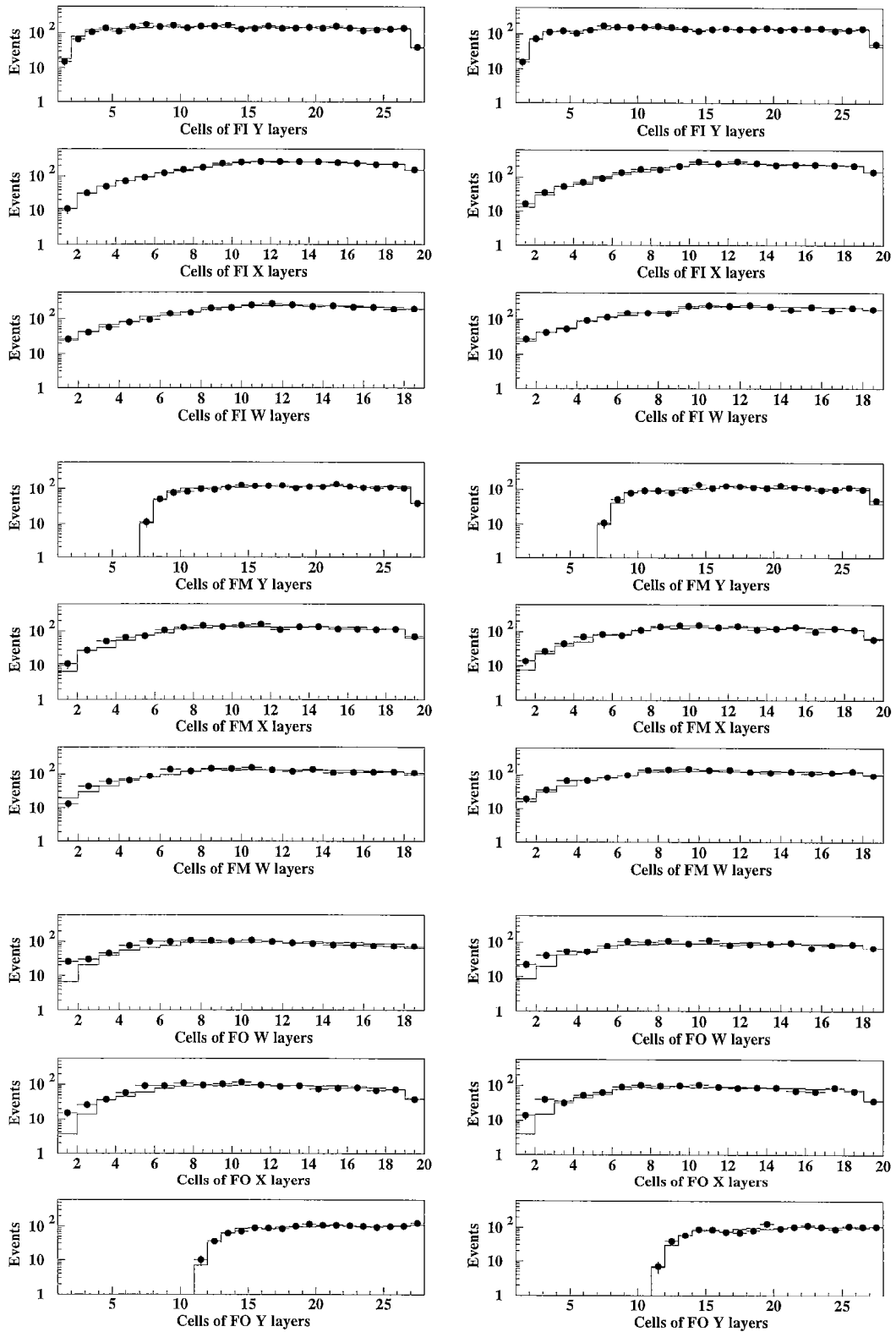
Figure 5.2: The occupancy of the forward-backward muon chambers for the 1995 Data (dots) and the Monte Carlo simulation (solid line). The right side shows the cells for $z > 0$, the left side the cells for $z < 0$.

category	muon chambers						momentum resolution [%]		fraction [%]	
	barrel			forward			MC	Data	MC	Data
1	MI	MM	MO	-	-	-	4.9	4.6	56.4	57.0
2	MI	MM	-	-	-	-	29.1	28.8	6.5	6.0
3	MI	-	MO	-	-	-	28.2	27.8	6.3	6.5
4	-	MM	MO	-	-	-	25.4	25.0	7.8	7.0
5	MI	MM	-	FI	-	-	12.5	11.7	7.2	7.5
6	MI	-	-	FI	-	-	37.7	38.5	1.1	0.9
7	-	MM	-	FI	-	-	28.7	36.6	0.8	0.8
8	MI	MM	-	FI	FM	-	24.6	25.1	1.5	1.5
9	MI	-	-	FI	FM	-	60.4	76.1	2.2	2.4
10	-	MM	-	FI	FM	-	-	-	0.1	0.1
11	-	-	-	FI	FM	-	-	-	0.3	0.3
12	MI	-	-	FI	-	FO	44.1	47.7	0.1	0.3
13	-	-	-	FI	-	FO	-	-	<0.1	0.1
14	MI	-	-	FI	FM	FO	31.9	32.4	8.6	8.7
15	-	-	-	FI	FM	FO	61.8	54.7	1.1	0.9

Table 5.2: The momentum resolution for each possible combination of muon chambers for the 1995 data and the Monte Carlo simulation. Also shown is the fraction of each combination with respect to all selected muons.

of 4.2% for barrel triplets does not agree with the design value of 2.5% (section 3.8.1) since all non-radiative muons are used for the determination, regardless of their location inside the fiducial volume. All muons in regions with an inhomogeneous electric or magnetic field, that is close to disconnected cells or chamber edges, have to be rejected to reach the design value.

Including also events with radiative muons leads to a momentum resolution of 4.6% for barrel triplets. The momentum resolutions for all muons are given in table 5.2 for all possible combinations of muon chambers. Also shown is the fraction of muons of a certain category with respect to all selected muons. The results for the data agree very well with the Monte Carlo simulation.

For barrel doublets the momentum resolution varies between 25.0% and 28.8% depending on the combination of chamber segments used for the reconstruction. In the S-region the momentum resolution is not constant but increases smoothly from 43° to 36°. The θ-dependence is due to the decrease of the lever arm as a function of θ:

$$\frac{\Delta p_\mu}{p_\mu} = \frac{1}{LS}\sqrt{(L\delta S)^2 + (2S\delta L)^2}. \qquad (5.3)$$

The momentum resolutions of 8.7% for S-region triplets in non-radiative events and 11.7% for all muons are determined regardless of the polar angle of the muon. In the T-region $\Delta p_\mu/p_\mu$ is limited by multiple scattering in the 90 cm thick iron door:

$$\frac{\Delta p_\mu}{p_\mu} = \frac{\alpha_{MS}}{\alpha_{bend}}, \qquad (5.4)$$
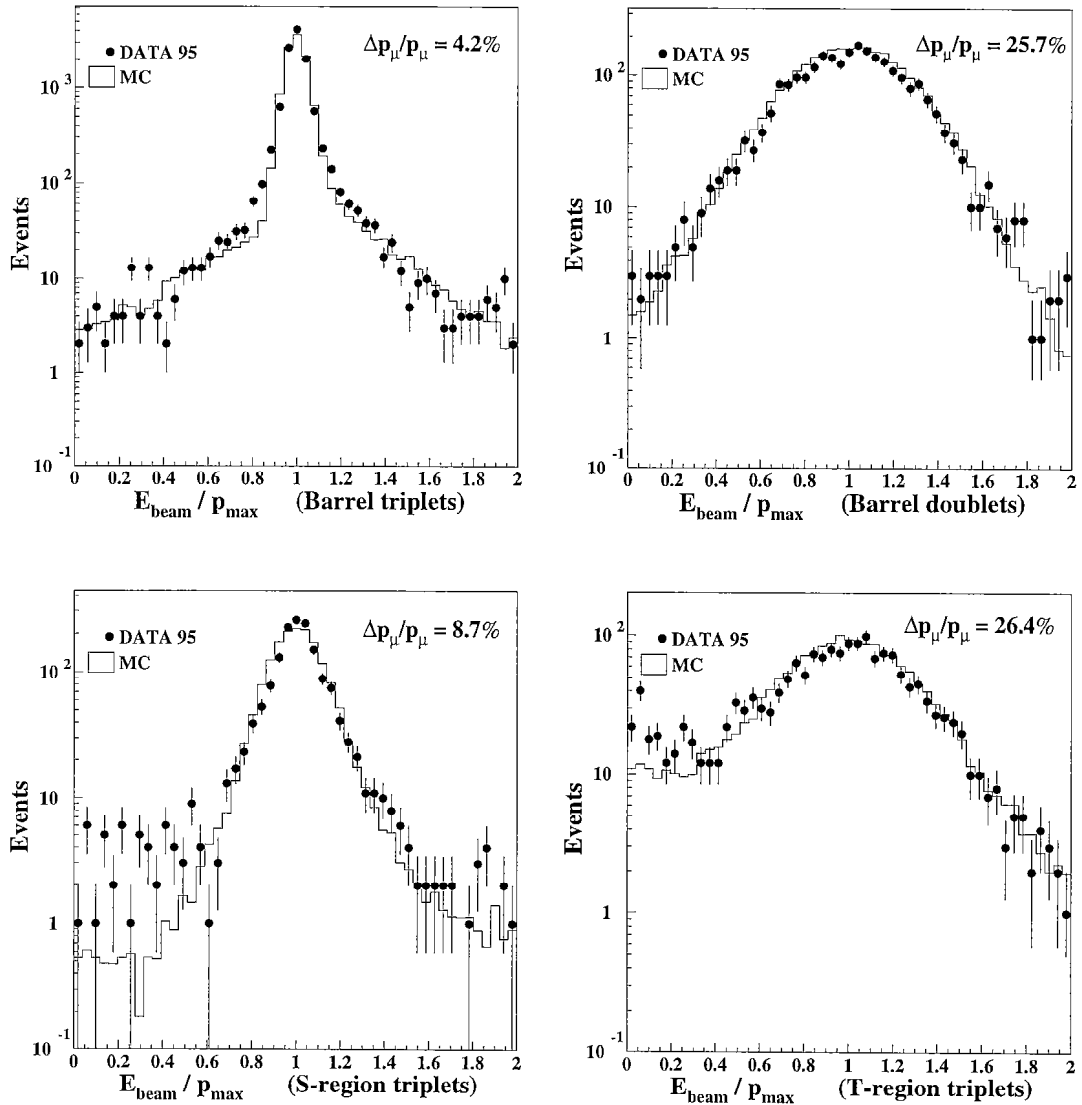
Figure 5.3: The resolution of the muon momentum based on 1995 data for barrel triplets and doublets and the two forward regions S and T. Only events with non-radiative muons are considered.
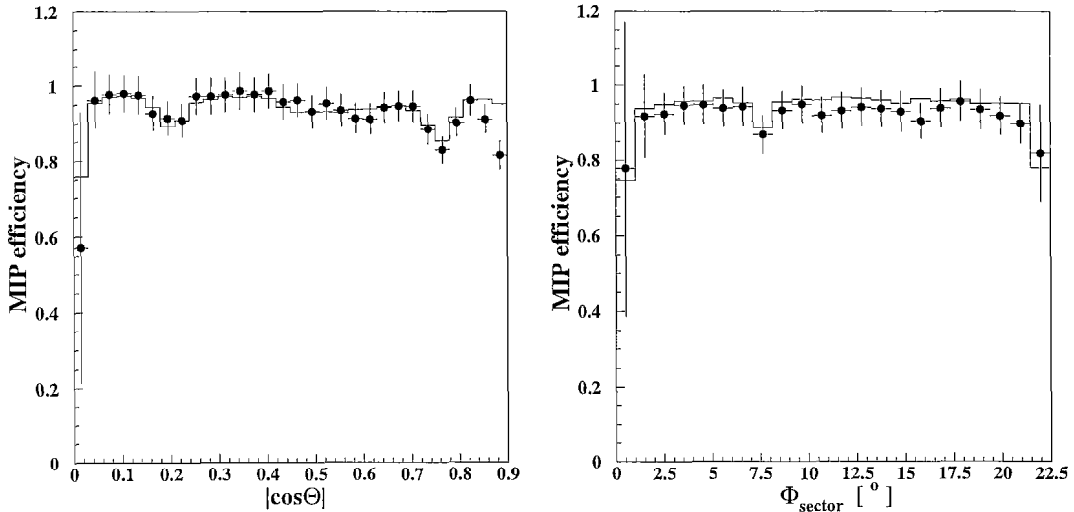
Figure 5.4: The efficiency of the MIP selection of the 1995 data (dots) and the Monte Carlo simulation. The left side shows the dependence on the polar angle θ, on the right side the dependence on Φ in the muon chamber sector.

where $\alpha_{\rm MS}$ is the average multiple scattering angle and $\alpha_{\rm bend}$ the bending angle due to the magnetic field. They are determined as follows:

$$\alpha_{\rm bend} \approx \frac{DB}{p_\mu K \cos\theta},\tag{5.5}$$

$$\alpha_{\rm MS} = \frac{0.0136}{p_\mu}\sqrt{\frac{D}{X_0\cos\theta}}\left[1 + 0.038\ln\left(\frac{D}{X_0\cos\theta}\right)\right],\tag{5.6}$$

with B the magnetic field, D the thickness of the door, p_μ the muon momentum, K=3.336 (unit conversion constant), X_0=1.76 cm the radiation length of iron and θ the polar angle of the track [30]. For B=1.2 T, D=0.9 m, p_μ=45.6 GeV and θ=30° this leads to an $\alpha_{\rm MS}$ of 2.7 mrad and an $\alpha_{\rm bend}$ of 8.3 mrad. Thus the momentum resolution $\Delta p_\mu/p_\mu$ is 32.3% . This is in very good agreement with the resolution for T-region triplets of 32.4% determined from data (table 5.2).

5.3 Efficiency of the MIP selection

The efficiency of the MIP selection is determined using the MM sample whose selection criteria are based on the muon spectrometer and not the calorimeters. For every event it is checked if it would also be selected by a selection based on calorimeter information. The result is shown in figure 5.4. The left plot shows the dependence of the MIP efficiency on the polar angle θ, the right plot the dependence on Φ in the coordinate system of the muon chamber sectors. There is a very good agreement between data and Monte Carlo.

The inner part of the tracking chamber consists of 12 sectors, the outer part 24 sectors, each covering 30° and 15° in Φ, respectively. Thus the wire planes of the

	MIP selection efficiency [%]		
	all	barrel	endcap
Data 1995	93.47±0.15	95.08±0.15	89.07±0.36
Monte Carlo	94.02±0.03	94.62±0.03	92.35±0.06
$\sqrt{s}$=130 GeV	92.1±2.2	92.2±2.6	91.8±4.0
Monte Carlo	94.2±0.2	94.5±0.2	93.2±0.3
$\sqrt{s}$=136 GeV	93.2±2.3	96.6±2.0	83.9±6.6
Monte Carlo	94.7±0.2	95.2±0.2	93.5±0.4
$\sqrt{s}$=161 GeV	91.7±2.3	91.3±2.8	92.7±4.1
Monte Carlo	93.5±0.1	94.3±0.1	91.4±0.3
$\sqrt{s}$=172 GeV	85.5±3.2	92.9±2.8	69.2±7.4
Monte Carlo	91.8±0.1	92.5±0.2	90.2±0.3
$\sqrt{s}$=183 GeV	91.0±1.2	93.8±1.3	85.5±2.6
Monte Carlo	94.8±0.1	95.4±0.1	93.3±0.2

Table 5.3: The efficiency of MIP selection for data and Monte Carlo simulation. Efficiencies are given for the complete fiducial volume as well as for the barrel and endcap region separately.

tracking chamber are located at $0°$, $7.5°$, $15°$ and $22.5°$ in the coordinate system of the muon chamber sector. The loss of efficiency at these angles is clearly visible. In addition, there are gaps between the hadron calorimeter modules at the ends and the center of the sector. They also result in a reduced efficiency. The efficiency of the MIP selection for data and Monte Carlo is shown in table 5.3. In general data and Monte Carlo simulation agree well within the errors. The impact on the selection due to small discrepancies in the overall MIP efficiency for some energy points is negligible. Only a small fraction of the selected events relies on the MIP selection and most of the muons in the MX and XX sample are already identified by means of muon singlets (section 6.5).

5.4 Efficiencies of the scintillators and RPCs

A muon-pair event is only selected if one of the muons has a scintillation counter time within a window of ±5 ns around the beam crossing. The different combinations of scintillators and RPCs, with $|t_{\text{scin}}| <5$ ns, belonging to a muon track in the forward region are shown in figure 5.5 for the 1995 data. The fractions of selected muons with a certain combination of matched scintillators and RPCs can be seen in table 5.4. These muons have to have at least one endcap scintillator or RPC time $|t_{\text{scin}}| <5$ ns. An agreement between data and Monte Carlo is not important for the combinations with two or three matched scintillators or RPCs. For the categories with only one matched scintillator or RPC there is only a very small discrepancy between data and Monte Carlo. The impact on the selection is negligible since only one muon of a muon-pair is required to have a $|t_{\text{scin}}| <5$ ns.

For the determination of the inefficiencies of the scintillation counters the complete sample of selected events is used. No MIPs are used for the determination
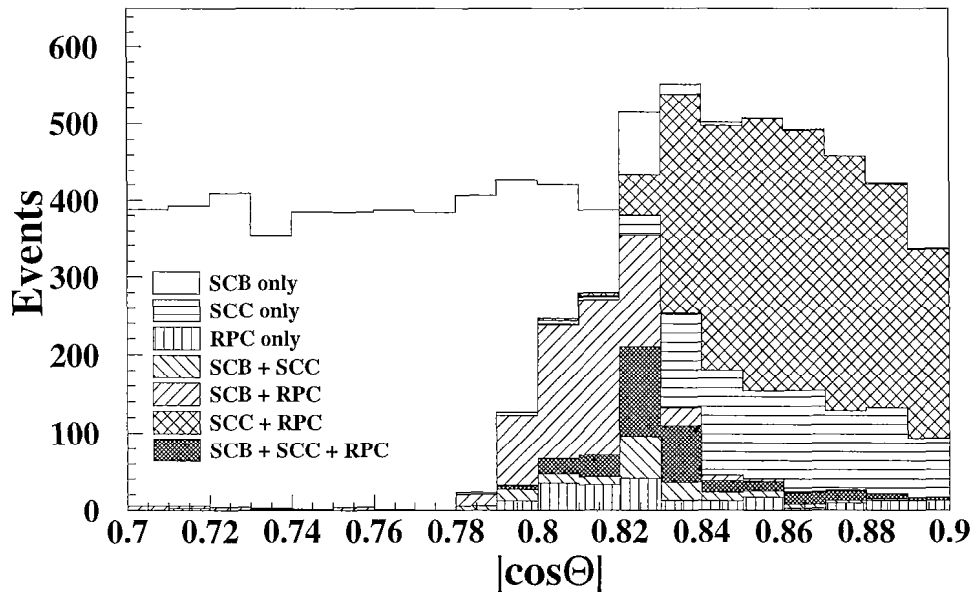
Figure 5.5: The different combinations of scintillators and RPCs, with $|t_{\text{scin}}|$ <5 ns, belonging to a muon track in the forward region for the 1995 data. (SCB: barrel scintillator; SCC: endcap scintillator)

Combination	Data 1995 [%]	MC [%]
SCC only	18.2±0.6	23.6±0.1
RPC only	5.0±0.3	3.6±0.1
SCB + SCC	3.3±0.3	2.4±0.1
SCB + RPC	18.3±0.6	17.7±0.1
SCC + RPC	48.5±0.7	50.3±0.1
SCB + SCC + RPC	6.7±0.4	2.4±0.1

Table 5.4: The fractions of different combinations of counters for muons that have at least one endcap scintillator or RPC time $|t_{\text{scin}}|$ <5 ns. (SCB: barrel scintillator; SCC: endcap scintillator)

	Efficiency [%]		
	all	$z > 0$	$z < 0$
Barrel Scintillator (Data)	85.9±0.2	-	-
Barrel Scintillator (M.C.)	87.6±0.0	-	-
Endcap Scintillator (Data)	88.5±0.5	88.3±0.7	88.7±0.7
Endcap Scintillator (M.C.)	86.5±0.1	87.2±0.1	85.8±0.1
RPC (Data)	74.2±0.7	76.3±1.0	72.0±1.1
RPC (M.C.)	69.1±0.2	71.1±0.2	67.0±0.2

Table 5.5: The efficiency of the scintillation counters and the RPC for the 1995 data and the Monte Carlo simulation. Here, efficiency refers to how often the respective counters provide a time signal within a window of ±5 ns around the beam crossing that is matched to a selected muon. Efficiencies are given for the complete fiducial volume as well as for the barrel and endcap region separately.

of the RPC efficiency, since they do not reach the RPCs. It is counted how often the track of a muon points to a counter with, $N_{\rm sig}$, or without, $N_{\rm miss}$, timing signal of $|t_{\rm scin}| < 5$ ns. The efficiency is then calculated as:

$$\epsilon = \frac{N_{\rm sig}}{N_{\rm sig} + N_{\rm miss}}. \tag{5.7}$$

The efficiencies of the scintillation counters and the RPCs are shown in figure 5.6. Table 5.5 shows the overall efficiencies for the barrel and the endcap region. There is a very good agreement between data and the Monte Carlo simulation. The efficiencies of the barrel and endcap scintillators are high with almost 90%. As figure 5.6 shows, all endcap scintillators contribute to the overall inefficiency while the inefficiency of the barrel scintillators mainly arises from two counters. The efficiency for the RPCs is low and due to the requirement $|t_{\rm scin}| < 5$ ns. The RPCs have a time resolution of 2.9 ns, that is many RPC signals are not matched because they exceed the cut value of 5 ns. In this analysis the RPC times are only used as a backup for the endcap scintillator. As figure 5.5 and table 5.4 show, there are only few muons with a matched RPC and no scintillator signal. As part of the forward-backward muon trigger, the RPCs have an efficiency of more than 99% [36].

Due to the geometry of the counters there are gaps in Φ every 11.25° in the barrel and every 22.5° in the forward region. The azimuthal distributions of the selected events for the scintillators and RPCs are shown in figure 5.7. The gaps at 0° in Φ for the barrel scintillation counters and on both edges of the endcap scintillators and the RPC are clearly visible and well reproduced in the Monte Carlo simulation.

5.5 Efficiency of the central tracking chamber

A muon-pair candidate has to have at least one TEC track with a distance of closest approach (DCA) in the r-Φ-plane of less than 1 mm. Missing high voltage
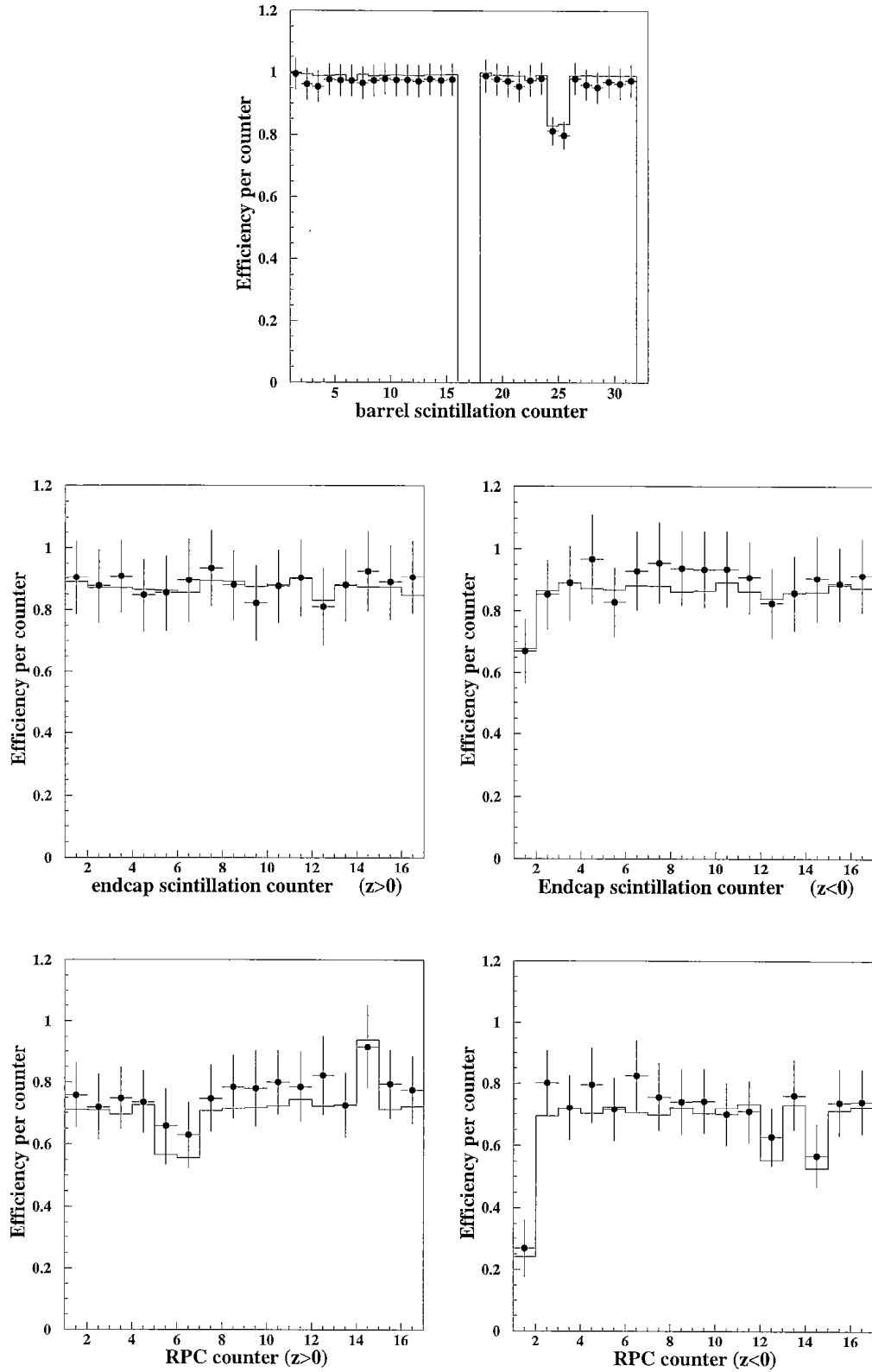
Figure 5.6: The efficiencies of scintillation counters and the RPCs for the 1995 data (dots) compared to the Monte Carlo simulation (solid line). Here, efficiency refers to how often the respective counters provide a time signal within a window of ±5 ns around the beam crossing that is matched to a selected muon.
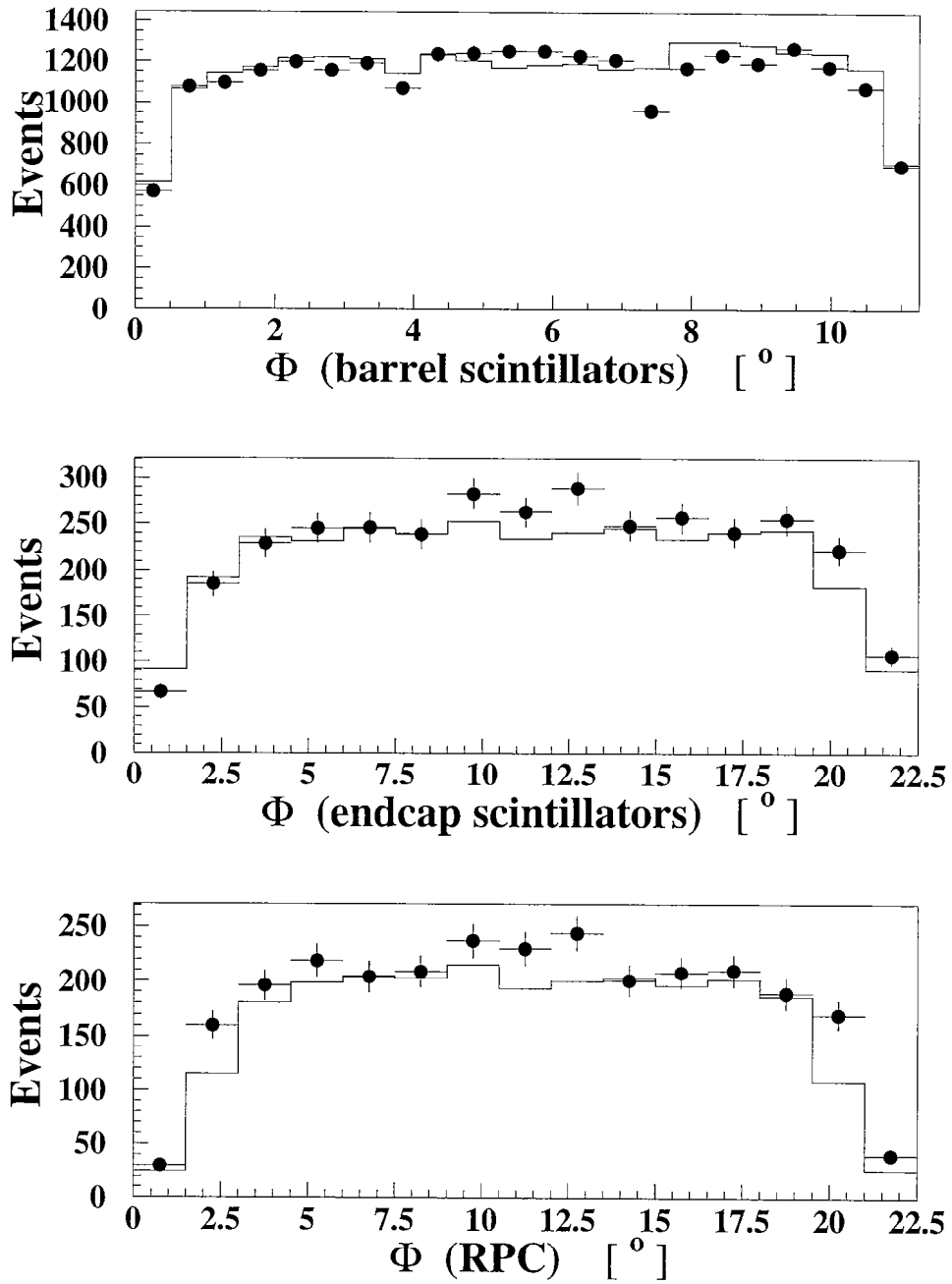
Figure 5.7: The azimuthal distributions of the selected events for the scintillators and RPCs for the 1995 data (dots) compared to the Monte Carlo simulation (solid line). The entries of all counters are projected onto the angular coverage of one counter.

		Probability [%]		
		all	$|\cos\theta|<0.7$	$|\cos\theta|>0.7$
2 tracks:	Data 1995	98.6±0.1	99.3±0.1	96.6±0.4
	Monte Carlo	97.6±0.1	97.8±0.2	97.2±0.3
1 track only:	Data 1995	1.4±0.1	0.7±0.1	3.4±0.4
	Monte Carlo	2.4±0.1	2.2±0.2	2.8±0.3

Table 5.6: The probabilities to find two tracks or one track only in the inner tracking chamber for data and Monte Carlo simulation. The probabilities are given for the complete fiducial volume as well as for the barrel and the endcap region separately.

in one or more sectors of the inner tracking chamber may lead to the loss of one or both TEC tracks and thus the event might not be selected. The status of the high voltage is, therefore, taken into account in the Monte Carlo simulation.

The events of the MM sample are used to determine the track efficiency of the TEC. The number of events with two TEC tracks is compared to the number of events with only one track. The probabilities to find two tracks or one track only in the inner tracking chamber is shown in table 5.6. There is good agreement between data and the Monte Carlo simulation. The impact on the selection of the small discrepancy in the probability of finding one track only can be neglected (section 6.5).

5.6 Trigger efficiencies

The L3 trigger system consists of three different decision levels and is described in section 3.9.

5.6.1 Level-2 and level-3 trigger

The level-2 and level-3 trigger reduce the amount of background such as detector noise and cosmic radiation. A certain number of events which would be rejected by the algorithms are nevertheless kept (*pre-scaled events*). The pre-scaling factors, f_{ps}, are 10 for the level-2 and 100 for the level-3 trigger. The efficiency, $\epsilon_{lev2,3}$, of the triggers is given by:

$$\epsilon_{lev2,3} = \frac{N_{sel}}{N_{sel} + N_{ps}(f_{ps} - 1)}, \tag{5.8}$$

where N_{sel} is the number of selected events including the number of pre-scaled events, N_{ps}. The error on the trigger efficiency is calculated as follows (see equation A.2):

$$\Delta\epsilon_{lev2,3} = \sqrt{\frac{\epsilon_{lev2,3}\left(1 - \epsilon_{lev2,3}\right)}{N_{sel}}}. \tag{5.9}$$

In the data samples of 1995 through 1997, no event was found that had been rejected by the level-2 or the level-3 trigger. Thus the level-2 and level-3 triggers are 100% efficient for events originating from muon-pair production.

5.6.2 Level-1 trigger

A muon-pair event is triggered by either the muon trigger, the TEC trigger, the energy trigger or by any combination of these triggers. The trigger referred to as the *muon trigger* is either the barrel muon trigger [35], the forward muon trigger [36] or both of these, depending on the polar angles of the muons. The determination of the level-1 trigger efficiency is based on the fact that all three possible trigger decisions are uncorrelated. The trigger efficiency determination is performed in 18 bins for $0.0 < \cos\theta < 0.9$.

Two methods are used to determine the trigger efficiency. The first method determines the trigger efficiency of each trigger according to:

$$\epsilon_i = \frac{N_{jk+i}}{N_{jk}}, \tag{5.10}$$

with number of selected events, N_{jk}, triggered by either trigger j or k and N_{jk+i} the number of events triggered in addition by trigger i. The letters i, j and k represent any permutation of the muon, TEC and energy trigger. The level-1 trigger efficiency, ϵ_{lev-1} is then given by:

$$\epsilon_{lev-1} = 1 - (1 - \epsilon_i)(1 - \epsilon_j)(1 - \epsilon_k). \tag{5.11}$$

The second method is based on Poisson statistics. It takes statistical fluctuations in the data into account by fitting the three single trigger efficiencies. For the fitting procedure the data sample is sub-divided into classes representing the different combinations of the three triggers. Each trigger has two possible states (yes/no), thus there are $2^3 = 8$ classes. The eighth class would contain the events that have no trigger at all. The number of expected events, μ_i, for the class i is calculated as:

$$\mu_i = N_{all} \prod_j \epsilon_j \prod_k (1 - \epsilon_k), \tag{5.12}$$

with N_{all} the total number of events in all eight classes for each bin in $\cos\theta$. The index j loops over all triggers the event is triggered by while k loops over all other triggers. Poisson statistics are used to calculate for each class the probability, $P(\mu_i, N_i)$, to find N_i events while μ_i are expected. The three single trigger efficiencies and the total number of muon-pair events are obtained by maximising the logarithm of the total likelihood to select N_i events while μ_i are expected using the following log-likelihood function:

$$\ln L = \ln \prod_i P(\mu_i, N_i) = \sum_i \ln P(\mu_i, N_i). \tag{5.13}$$

The total level-1 trigger efficiency is then determined using equation 5.11. Table 5.7 compares the results on the total level-1 trigger efficiencies obtained by the

$\sqrt{s}$ [GeV]	$\epsilon_{\text{lev}-1}$ [%] (calculated)	$\epsilon_{\text{lev}-1}$ [%] (fit)
91.31	99.56±0.08	99.57±0.08
89.45	99.89±0.06	99.90±0.06
91.29	99.90±0.05	99.90±0.05
92.98	99.83±0.06	99.83±0.06

Table 5.7: The efficiencies of the level-1 trigger for the different data taking periods of 1995 determined using two different methods.

$\sqrt{s}$ [GeV]	ϵ_{muon} [%]	ϵ_{TEC} [%]	ϵ_{energy} [%]	$\epsilon_{\text{lev}-1}$ [%]
91.31	90.42±0.43	93.33±0.35	41.47±1.27	99.57±0.08
89.45	93.09±0.51	93.24±0.51	44.17±1.77	99.90±0.06
91.29	93.55±0.42	93.73±0.41	42.68±1.51	99.90±0.05
92.98	92.66±0.43	93.01±0.42	44.64±1.41	99.83±0.06
130.0	98.8±0.5	87.6±2.8	50.5±6.4	99.9±0.1
$\sqrt{s'}$>110.5	98.8±0.72	88.7±3.6	47.1±9.5	99.9±0.1
135.9	97.8±1.1	93.6±2.4	50.0±7.3	99.9±0.1
$\sqrt{s'}$>115.5	96.7±2.6	96.7±2.6	43.3±11.5	99.9±0.1
161.3	93.6±1.8	91.5±2.7	41.7±6.9	99.7±0.1
$\sqrt{s'}$>137.1	98.5±1.2	88.5±5.9	34.3±10.5	99.9±0.1
172.1	96.9±0.9	89.6±2.8	52.3±7.6	99.8±0.1
$\sqrt{s'}$>146.3	98.4±1.2	95.1±2.0	46.8±11.2	99.9±0.1
182.7	97.01±0.94	79.70±2.63	43.96±4.98	99.84±0.21
$\sqrt{s'}$>155.3	97.42±1.30	87.24±3.03	45.85±7.29	99.97±0.13

Table 5.8: The efficiencies of the level-1 sub-triggers and the overall trigger efficiencies for the different data taking periods.

two different methods. They are in perfect agreement. For data at $\sqrt{s}$>100 GeV, except for $\sqrt{s}$=183 GeV, the level-1 trigger efficiencies are only calculated as explained above and no longer fitted since there is not at least one entry per $\cos\theta$-bin and trigger combination.

The efficiencies of the different level-1 sub-triggers determined with the fit method are shown in table 5.8. The efficiencies of the muon trigger are always, for the TEC trigger almost always above 90% while the efficiencies of the energy trigger are in the order of 40%. The trigger efficiencies are determined using all selected events. However, most of the events in XX sample do not have the muon trigger. It can be seen that for the data at $\sqrt{s}$>100 GeV the muon trigger efficiency is higher than for the data at $\sqrt{s}\approx m_Z$, since for higher energies the XX sample is no longer considered (section 4.3.2). Determining the muon trigger efficiency, ϵ_{muon}, from the MM sample only, one obtains efficiencies higher than 99%.

Figure 5.8 shows the $\cos\theta$-dependence of the trigger inefficiencies for all three single triggers and the combined trigger inefficiency. The inefficiency of the energy trigger is flat in $\cos\theta$ while the largest inefficiencies of TEC and muon trigger are at the outer and inner edge, respectively. This results in a combined inefficiency
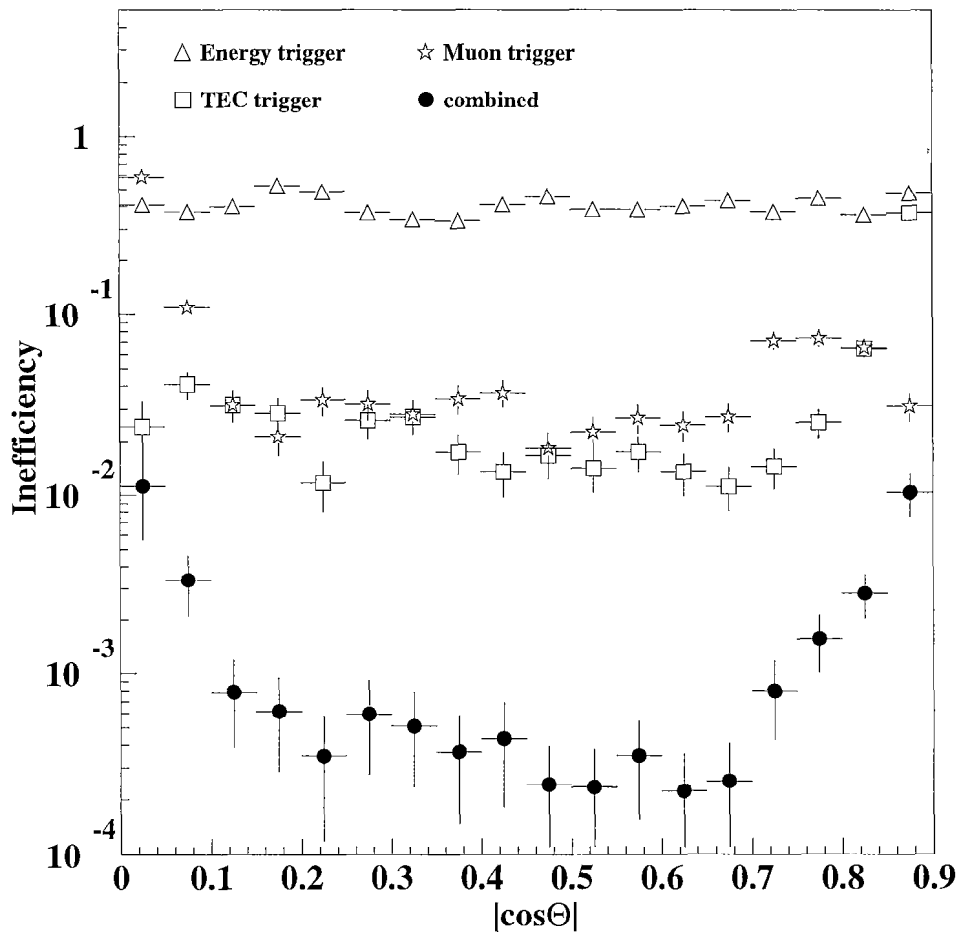
Figure 5.8: The $\cos\theta$-dependence of the trigger inefficiencies for the 1995 data. Shown are the inefficiencies for the three single triggers and the combined trigger inefficiency.

with its largest values around 0.0 and 0.9 in $\cos\theta$.

The combined trigger efficiency, ϵ_{trig}, is calculated from the trigger efficiencies of the different levels to:

$$\epsilon_{\text{trig}} = \epsilon_{\text{lev}-1} \times \epsilon_{\text{lev}-2} \times \epsilon_{\text{lev}-3}, \qquad (5.14)$$

$$\Delta\epsilon_{\text{trig}} = \sqrt{\Delta\epsilon_{\text{lev}-1}^2 + \Delta\epsilon_{\text{lev}-2}^2 + \Delta\epsilon_{\text{lev}-3}^2}. \qquad (5.15)$$

The combined trigger efficiencies are for all analysed periods equal to the efficiencies of the level-1 trigger since no event was rejected by the level-2 or level-3 trigger. They are shown in table 5.8 for all data taking periods. Combining three uncorrelated triggers, two of these with a high trigger efficiency, leads to a very high combined trigger efficiency which is known to high precision. A well known trigger efficiency is one of the conditions that allow a precise cross section measurement (see chapter 6).

Chapter 6

Cross section

The cross section is defined as the ratio of the number of selected muon-pair events, N_{sel}, and the appropriate integrated luminosity $\mathcal{L}$:

$$\sigma_{\text{tot}} = \frac{N_{\text{sel}} - N_{\text{bkgd}}}{\mathcal{L} \epsilon_{\text{MC}} \epsilon_{\text{trig}}}, \tag{6.1}$$

where N_{bkgd} is the number of background events expected from the Monte Carlo simulation and ϵ_{MC} and ϵ_{trig} take into account the limited detector acceptance and trigger efficiency, respectively.

6.1 Luminosity determination

The integrated luminosity is determined using Bhabha events $e^+e^- \rightarrow e^+e^-(\gamma)$ at small scattering angles (section 3.2). Their theoretical cross section does not depend on the Z parameters since the photon exchange in the t-channel is dominant for small angles. The integrated luminosity, $\mathcal{L}$, is calculated from:

$$\mathcal{L} = \frac{N_{\text{lumi}} - N_{\text{bkgd}}}{\sigma_{\text{lumi}}}, \tag{6.2}$$

by correcting the number of luminosity events, N_{lumi}, for background events, N_{bkgd}, and dividing by the visible cross section, σ_{lumi}, expected from theory.

The integrated luminosities for the different data taking periods and their errors [64, 65, 66] are shown in table 6.1. The errors are sufficiently small to have a negligible contribution to the systematic error (table 6.5).

6.2 Background

Selection cuts reduce the number of background events contaminating the sample of selected muon-pair events as much as possible. The background processes are given in section 4.2. At center-of-mass energies larger than 100 GeV, also the process $e^+e^- \rightarrow \mu^+\mu^-\gamma_{\text{ISR}}$ has to be taken into account for the high energy sample ($\sqrt{s'} > 0.85\sqrt{s}$).

$\sqrt{s}$ [GeV]	$\mathcal{L}$ [nb^{-1}]	$\Delta\mathcal{L}/\mathcal{L}$ [%]
91.3088	5083.59	0.137
89.4516	7353.89	0.137
91.2921	3465.51	0.137
92.9833	7824.26	0.137
129.96	6112.70	0.3
135.92	5888.51	0.3
161.34	10904.95	0.6
172.13	10250.38	0.6
182.68	55490.66	0.5

Table 6.1: Integrated luminosities and their errors for the different data taking periods.

6.2.1 Background from cosmic radiation

The number of background events with muons originating from cosmic radiation is determined from the side bands of the distributions for $d_\perp$ and t_{scin} (section 4.2.1). Assuming a flat distribution for cosmic muons, for both side-bands the entries, N^i_{int}, in a certain interval, L^i_{cos}, are counted and then extrapolated to obtain the number of background events in the interval L^i_{data}, with the selected events:

$$N^i_{\text{cos}} = N^i_{\text{int}}\frac{L^i_{\text{data}}}{L^i_{\text{cos}}}, \qquad \Delta N^i_{\text{cos}} = \sqrt{N^i_{\text{int}}}\frac{L^i_{\text{data}}}{L^i_{\text{cos}}}. \qquad (6.3)$$

The weighted average of the number of events obtained from the $d_\perp$ and t_{scin} distributions yields the number of cosmic background events, N_{cosmic}, (see equations A.5 and A.6).

6.2.2 Background from events with ISR photons

For data taken at $\sqrt{s}>100$ GeV the sample referred to as the *high energy sample*, i.e. with $\sqrt{s}>0.85\sqrt{s}$ (section 4.3), contains events with a wrongly determined effective center-of-mass energy, $\sqrt{s'}$. The number of events from ISR background, $N^{\text{isr}}_{\text{bkgd}}$, is determined from the Monte Carlo simulation. The number of selected events, $N^{\text{sel}}_{\text{MCisr}}$, with the calculated $\sqrt{s'}$ larger and the generated $\sqrt{s'}$ lower than the threshold of $0.85\sqrt{s}$, is compared to all selected MC events, $N^{\text{sel}}_{\text{MC}}$:

$$N^{\text{isr}}_{\text{bkgd}} = \epsilon_{\text{isr}}N_{\text{sel}} = \frac{N^{\text{sel}}_{\text{MCisr}}}{N^{\text{sel}}_{\text{MC}}}N_{\text{sel}}, \qquad (6.4)$$

with N_{sel} the number of all selected data events. The error is (see also equations A.7 and A.8):

$$\Delta N^{\text{isr}}_{\text{bkgd}} = \sqrt{N^2_{\text{sel}}\Delta\epsilon^2_{\text{isr}} + \epsilon^2_{\text{isr}}\Delta N^2_{\text{sel}}}. \qquad (6.5)$$

6.2.3 Background from e^+e^- annihilation processes

The number of background events, N^i_{bkgd}, from other e^+e^- annihilation processes is determined from Monte Carlo simulation:

$$N^i_{\text{bkgd}} = N^{\text{bkgd}}_{\text{sel}} \frac{\mathcal{L}\sigma_{\text{MC}}}{N^{\text{gen}}_{\text{MC}}}, \tag{6.6}$$

$$\Delta N^i_{\text{bkgd}} = \sqrt{\frac{N^{\text{bkgd}}_{\text{sel}}\left(N^{\text{gen}}_{\text{MC}} - N^{\text{bkgd}}_{\text{sel}}\right)}{N^{\text{gen}}_{\text{MC}}}}, \tag{6.7}$$

where $N^{\text{gen}}_{\text{MC}}$ is the number of generated and $N^{\text{bkgd}}_{\text{sel}}$ the number of selected Monte Carlo events, σ_{MC} the theoretical prediction of the cross section for the process i and $\mathcal{L}$ the delivered luminosity (see also equations A.3 and A.4).

The number of background events among the selected events can then be calculated as follows where the error is obtained by adding the errors on the single processes in quadrature:

$$N_{\text{bkgd}} = N^{\tau\tau}_{\text{bkgd}} + N^{\gamma\gamma}_{\text{bkgd}} + N^{q\bar{q}}_{\text{bkgd}} + N^{WW}_{\text{bkgd}} + N^{Zee}_{\text{bkgd}} + N^{ZZ}_{\text{bkgd}} + N^{\text{isr}}_{\text{bkgd}} + N_{\text{cosmic}}, \tag{6.8}$$

$$\Delta N_{\text{bkgd}} = \sqrt{\sum_i \Delta N^{i2}_{\text{bkgd}}}. \tag{6.9}$$

6.2.4 Background determination

Table 6.2 shows the background contamination for each data taking period. The contributions from different processes can be found in table B.2. The background amounts to $\approx 1.2\%$ for $\sqrt{s} = m_Z$ and $\approx 1.5\%$ for $\sqrt{s} \approx m_Z \pm 1.8$ GeV. The largest contribution arises from tau-pair production, with 67% from processes where both taus decay into muons.

The simulation of the tau-pair background can be verified by means of events in the momentum range of $0.5 < p_{\text{max}}/E_{\text{beam}} < 0.7$ GeV. There the background from tau-pair production is enriched to 38% . Comparing the distributions for the acollinearity ξ and the acoplanarity ζ for data and Monte Carlo shows that the process $e^+e^- \rightarrow \tau^+\tau^-(\gamma)$ is correctly simulated (figure 6.1). Since the distributions are normalised to luminosity, also the rate of tau-pair background is correctly simulated.

At center-of-mass energies $\sqrt{s} > 100$ GeV the dominating background arises from the process $e^+e^- \rightarrow e^+e^-\mu^+\mu^-(\gamma)$ (table B.2). The large background for $\sqrt{s} = 183$ GeV is caused by the lack of the toroidal magnetic field for most of the data taking in 1997. The trajectories of the muons in the region $0.8 < |\cos\theta| < 0.9$ are not bent anymore and a very high momentum is measured even for low momentum muons. Thus the cut on the highest muon momentum (section 4.2.2) does not reject a large fraction of the $e^+e^- \rightarrow e^+e^-\mu^+\mu^-(\gamma)$ background in this region.

$\sqrt{s}$ [GeV]	Σ background [%]
91.31	1.22±0.05
89.45	1.47±0.06
91.29	1.15±0.04
92.98	1.36±0.06
130.0	4.4±0.6
$\sqrt{s'}$>110.5	10.7±1.5
135.9	5.5±0.8
$\sqrt{s'}$>115.5	10.5±1.8
161.3	9.5±1.0
$\sqrt{s'}$>137.1	11.1±1.5
172.1	14.7±1.6
$\sqrt{s'}$>146.3	13.0±1.8
182.7	24.0±1.4
$\sqrt{s'}$>155.3	16.1±1.4

Table 6.2: Background contamination for the different data taking periods.
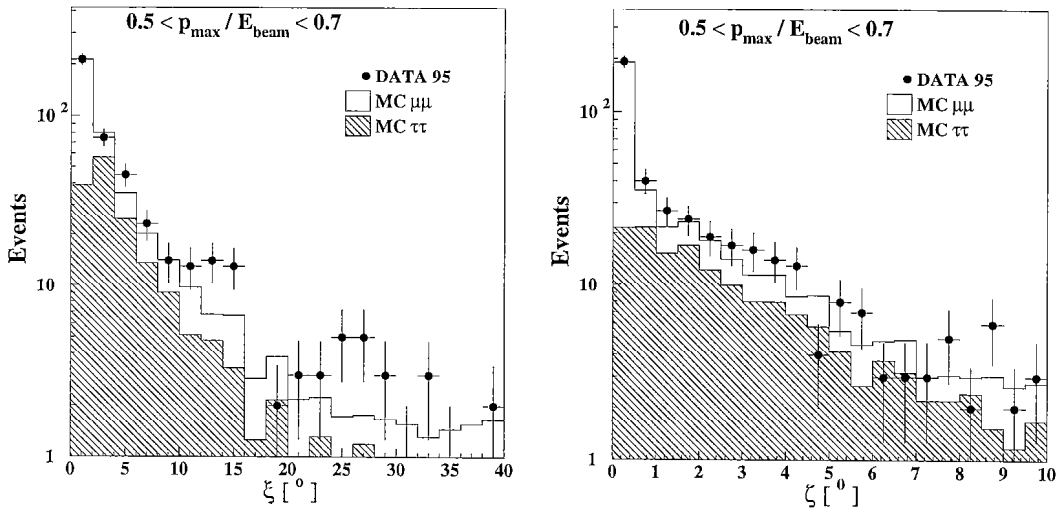
Figure 6.1: The tau-pair background can be increased using events in the momentum interval $0.5 < p_{\mathrm{max}}/E_{\mathrm{beam}} < 0.7$ GeV. The comparison of the acollinearity ξ and the acoplanarity ζ for data and Monte Carlo shows that the tau-pair events are correctly simulated.
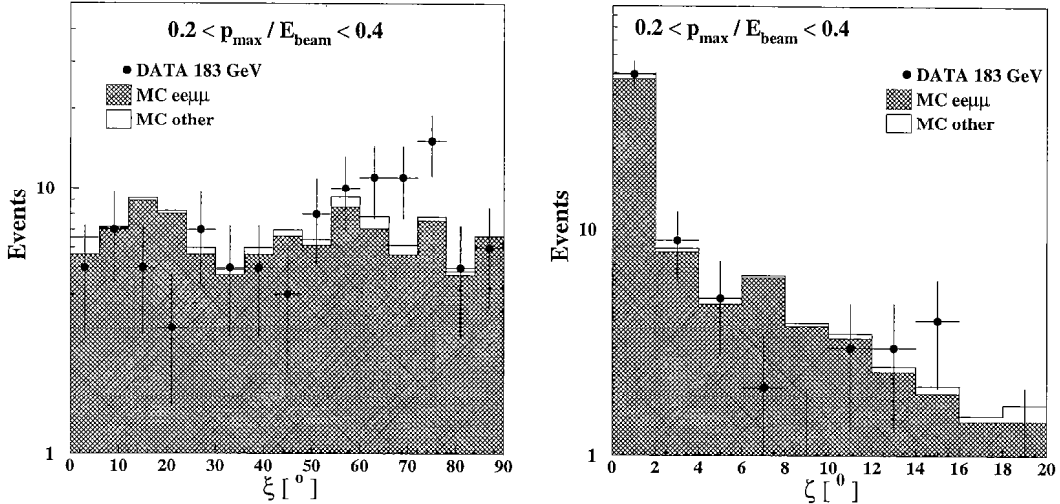
Figure 6.2: The background from the process $e^+e^- \rightarrow e^+e^-\mu^+\mu^-(\gamma)$ can be increased using events in the momentum interval $0.2 < p_{max}/E_{beam} < 0.4$ GeV. The comparison of the acollinearity ξ and the acoplanarity ζ for data and Monte Carlo shows that rate and events of the process $e^+e^- \rightarrow e^+e^-\mu^+\mu^-(\gamma)$ are correctly simulated.

The lack of the toroidal magnetic field is taken into account in the Monte Carlo simulation. The simulation of the $e^+e^-\mu^+\mu^-(\gamma)$ background is verified similarly to the tau-pair background. Taking events in the momentum range of $0.2 < p_{max}/E_{beam} < 0.4$ GeV enriches the background from $e^+e^-\mu^+\mu^-(\gamma)$ production to 95% (figure 4.17). Comparing the distributions for the acollinearity ξ and the acoplanarity ζ for data and Monte Carlo at $\sqrt{s}$=183 GeV shows that the process $e^+e^- \rightarrow e^+e^-\mu^+\mu^-(\gamma)$ is correctly simulated (figure 6.2). Again the distributions are normalised to luminosity so that also the rate of $e^+e^-\mu^+\mu^-(\gamma)$ background is correct.

6.3   Selection efficiency and acceptance

The selection efficiency is determined using simulated events. They are generated by the program KORALZ [54] according to the prediction of the Standard Model for the appropriate center-of-mass energies. The radiation of soft and collinear photons is calculated to all orders, hard initial and final state bremsstrahlung is simulated to $\mathcal{O}(\alpha^2)$.

The selection efficiency is determined from the generated number of muon-pair events, N_{MC}^{tot}, and the number of these events that pass the selection, N_{MC}^{sel}:

$$\epsilon_{MC} = \frac{N_{MC}^{sel}}{N_{MC}^{tot}}, \qquad \Delta\epsilon_{MC} = \sqrt{\frac{\epsilon_{MC}(1-\epsilon_{MC})}{N_{MC}^{tot}}}. \qquad (6.10)$$

The efficiencies of the selection in the full solid angle for the different data taking periods are given in table 6.3. The selection efficiencies for the total event sample

$\sqrt{s}$ [GeV]	efficiency [%]
91.31	76.85±0.16
89.45	76.05±0.18
91.29	76.42±0.13
92.98	77.21±0.18
130.0	65.6±0.5
$\sqrt{s'}$>110.5	78.9±0.7
135.9	62.8±0.5
$\sqrt{s'}$>115.5	74.3±0.7
161.3	57.6±0.4
$\sqrt{s'}$>137.1	72.6±0.5
172.1	57.8±0.4
$\sqrt{s'}$>146.3	75.4±0.5
182.7	56.6±0.4
$\sqrt{s'}$>155.3	73.9±0.5

Table 6.3: The selection efficiencies for the different data taking periods with respect to the full solid angle. The statistical error is due to the limited Monte Carlo statistics.

at $\sqrt{s}$>100 GeV are lower since about 50% of these events radiate an ISR photon. Most of these photons are radiated along the beam axis (section 4.3) and thus the muons are boosted in the opposite direction. Muon-pairs with at least one muon close to the beam axis in the polar angular range of $|\cos\theta|$>0.9 escape detection.

The cut on the acceptance at $|\cos\theta|$<0.9 for both muons is an implicit cut on the acollinearity for events close to the edge of the fiducial volume. The events concerned are mainly events with large photon radiation which causes the muons to be acollinear. Muons close to an edge of a muon chamber in Φ or θ may still have a reconstructed track in the muon chambers or just be selected as a MIP. However, the selection efficiency for MIPs is lower than for muons with reconstructed muon tracks and also the cut on the acollinearity is different for the three event samples MM, MX and XX. It is therefore important that the edges of the muon chambers are described correctly in the simulation.

Figure 6.3 shows the variation of the cross section along the different edges of the muon chambers for 1995. It can be seen that the cross section is stable around both, the Φ-edges of the muon chamber sectors and the central gap at $|\cos\theta|$<0.07 . In addition the cut on the acceptance at $|\cos\theta|$=0.9 is varied and does not have a large impact on the cross section. A systematic error of 0.3% is assigned. However, it is the largest contribution to the part of the systematic error that arises from the cut variations (section 6.5). It is due to an imperfect simulation of the end of the fiducial volume. This variation of the acceptance is also an indirect test for the parts of the detector that have their gaps at the same angles like the scintillation counters and the RPCs.
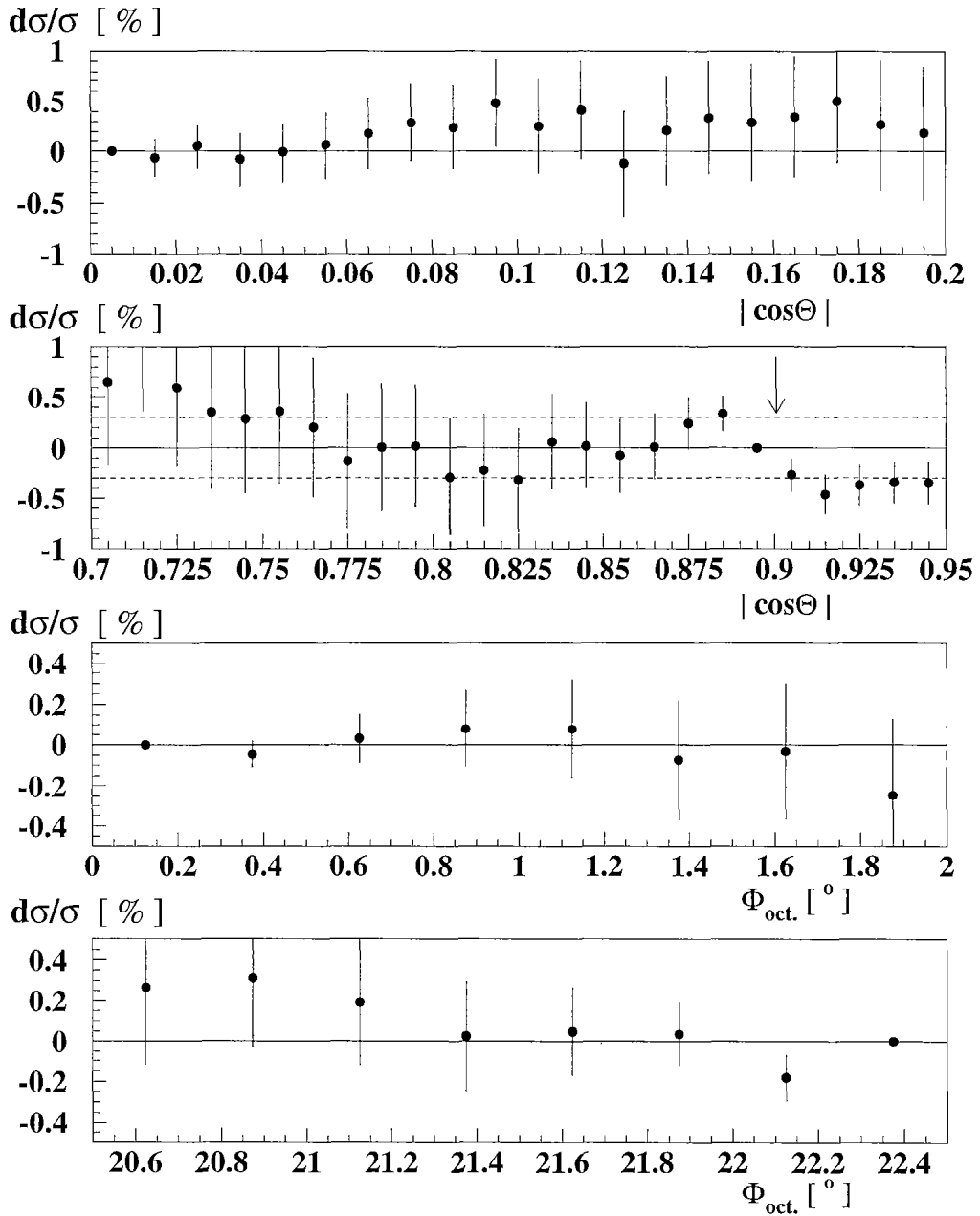
Figure 6.3: The variation of the cross section along the edges of the muon chamber sectors in Φ and $\cos\theta$. The cut on the acceptance at $|\cos\theta|$=0.9 is represented by the arrow. Shown are the results for $\sqrt{s}$=91.29 GeV.

$\sqrt{s}$ [GeV]	$\mathcal{L}$ [nb^{-1}]	$N_{\rm sel}$	$\sigma_{\rm tot}\pm$(stat.)$\pm$(syst.) [nb]	$\sigma_{\rm SM}$ [nb]
91.31	5083.59	5772	1.4657$\pm$0.0195$\pm$0.0065	1.4868
89.45	7353.89	2789	0.4917$\pm$0.0094$\pm$0.0024	0.5021
91.29	3465.51	3967	1.4818$\pm$0.0238+0.0061	1.4873
92.98	7824.26	4305	0.7039$\pm$0.0109$\pm$0.0034	0.7022

$\sqrt{s}$ [GeV]	$\mathcal{L}$ [nb^{-1}]	$N_{\rm sel}$	$\sigma_{\rm tot}\pm$(stat.)$\pm$(syst.) [pb]	$\sigma_{\rm SM}$ [pb]
130.0	6069.1	95	22.8$\pm$2.5$\pm$0.6	22.3
$\sqrt{s'}$>110.5	6069.1	43	8.0$\pm$1.4$\pm$0.2	8.2
135.9	5775.6	78	20.4$\pm$2.4$\pm$0.5	19.0
$\sqrt{s'}$>115.5	5775.6	34	7.1$\pm$1.4$\pm$0.2	7.1
161.3	10905.0	95	13.7$\pm$1.6$\pm$0.4	11.2
$\sqrt{s'}$>137.1	10905.0	40	4.5$\pm$0.8$\pm$0.1	4.4
172.1	10250.4	71	10.2$\pm$1.4$\pm$0.4	9.6
$\sqrt{s'}$>146.3	10250.4	34	3.8$\pm$0.7$\pm$0.1	3.8
182.7	55490.7	353	8.6$\pm$0.7$\pm$0.3	8.2
$\sqrt{s'}$>155.3	55490.7	157	3.2$\pm$0.3$\pm$0.1	3.3

Table 6.4: The cross sections for the different data taking periods and their comparison with the Standard Model prediction. The results for center-of-mass energies $\sqrt{s}$>100 GeV are given for two samples: $\sqrt{s'}$>0.1$\sqrt{s}$ and $\sqrt{s'}$>0.85$\sqrt{s}$. The statistical and systematic errors on the cross section measurement are shown separately.

6.4 Results of the measurement

Table 6.4 shows the results of the cross section measurements for the different data taking periods. The statistical error is determined according to:

$$\Delta\sigma^{\rm stat} = \frac{\sqrt{N_{\rm sel}}}{\mathcal{L}\epsilon_{\rm MC}\epsilon_{\rm trig}} \tag{6.11}$$

The error arising from systematic uncertainties is explained in section 6.5.

The program ZFITTER [55] was used for the theoretical prediction. For the Z mass the value measured at LEP, m_Z=91.19 GeV, is taken [57]. Its determination is dominated by the process $e^+e^-\to q\bar{q}(\gamma)$. Other input parameters are the top mass, m_t=175 GeV, measured at Fermilab [58] and a Higgs mass of m_H=300 GeV.

The cross sections for muon-pair production are measured for nine different center-of-mass energies between 89 and 183 GeV. For energies $\sqrt{s}$>100 GeV the cross sections are given for the total and the high energy sample ($\sqrt{s'}$>0.85$\sqrt{s}$). All measurements are in good agreement with the Standard Model. The cross sections are determined with a precision of about 1.5% for center-of-mass energies around the Z mass and to about 10% for higher $\sqrt{s}$. For all measurements the statistical error dominates the error arising from systematic uncertainties.

The comparison with the standard model can be seen in figure 6.4. The measurements for effective center-of-mass energies $\sqrt{s'}$>0.85$\sqrt{s}$ are included in the
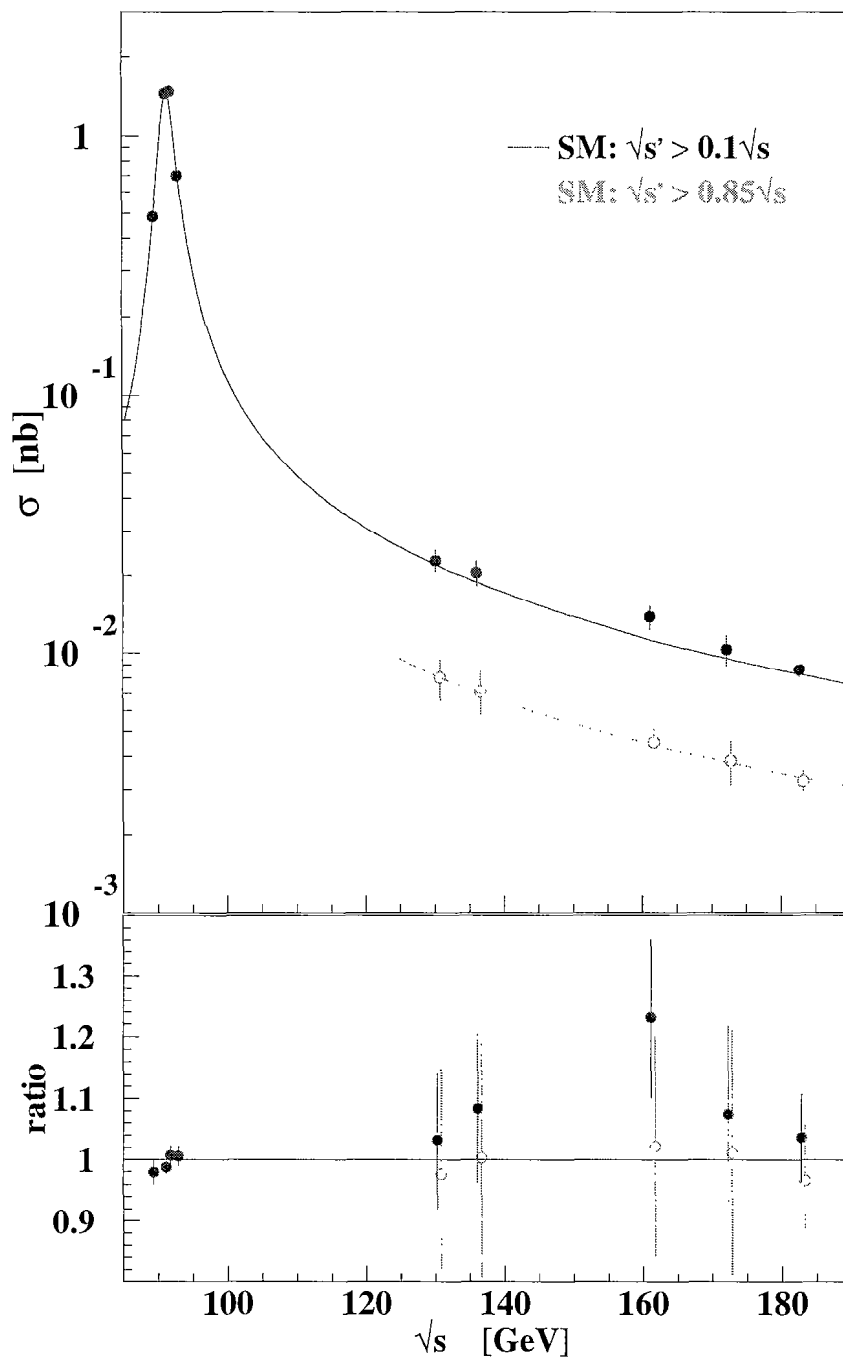
Figure 6.4: Comparison of the standard model predictions for the process $e^+e^- \to \mu^+\mu^-(\gamma)$ to the cross sections measured at nine different center-of-mass energies. The solid and dashed lines are the Standard Model predictions for $\sqrt{s'}>0.1\sqrt{s}$ and $\sqrt{s'}>0.85\sqrt{s}$, respectively. The solid and open symbols represent the respective measurements. The measurements at center-of-mass energies around the Z resonance have been corrected to correspond to $\sqrt{s'}>0.1\sqrt{s}$. The ratios of the measured and the predicted cross sections are shown below.

65

figure. The lower figure shows the ratios of the measured and the predicted cross sections. A good agreement between measurements and Standard Model predictions is found. Further L3 cross section measurements of the muon-pair production at center-of-mass energies around the Z resonance are published in [63, 64]. The results presented here are in excellent agreement with these previous measurements.

6.5 Systematic errors

The measurement of the total cross section contains systematic uncertainties. They originate from the limited knowledge of efficiency, acceptance and background corrections. Also the uncertainty from the placement of the selection cuts contributes to the systematic error:

$$\Delta\sigma^{\text{syst}} = \sqrt{\Delta\sigma_{\text{bkgd}}^{\text{syst}^2} + \Delta\sigma_{\text{lumi}}^{\text{syst}^2} + \Delta\sigma_{\text{MCeff}}^{\text{syst}^2} + \Delta\sigma_{\text{TReff}}^{\text{syst}^2} + \Delta\sigma_{\text{cuts}}^{\text{syst}^2}}$$

(6.12)

The single contributions to the systematic error are derived in equations A.9 to A.14. The different contributions to the overall systematic errors assigned to the different data taking periods are listed in table 6.5. The systematic uncertainty arising from the luminosity measurement is taken from table 6.1. The systematic error on the trigger efficiency is obtained as described in section 5.6.

The systematic error due to the selection cuts is the result from the impact of the variation of the different cuts on the cross section. Figure 6.5 shows the change of the cross section for the variation of the selection cuts for $\sqrt{s}$=91.29 GeV. The results for the other data taking periods are similar. The largest contribution to the systematic error arises from the selection cuts. They are again dominated by the error due to the cut on the acceptance in $\cos\theta$ (see section 6.3).

The probability to select a muon-pair independently from the muon chambers is 93.5% for the 1995 data (table 5.3). This is 0.5% lower than in the simulation. Most of the muons in the MX and XX sample are already identified by means of muon singlets (one p chamber segment). Therefore the contribution of the MIP selection to the systematic error is negligible. Taking the errors into account there is a difference of $\approx$3% for the MIP efficiency between the simulation and the data at $\sqrt{s}$=172.1 GeV. This difference, applied to 13% of the selected events that are based on the MIP selection (table B.1), yields a negligible contribution to the systematic error on the cross section measurement.

For the data of 1995 the probability to have only one TEC track is 1.4% for data and 2.4% for Monte Carlo (table 5.6). Thus the probability to lose both TEC tracks is 0.020% for data and 0.058% for Monte Carlo. The contribution of the difference of 0.038% between data and Monte Carlo to the systematic error is negligible.
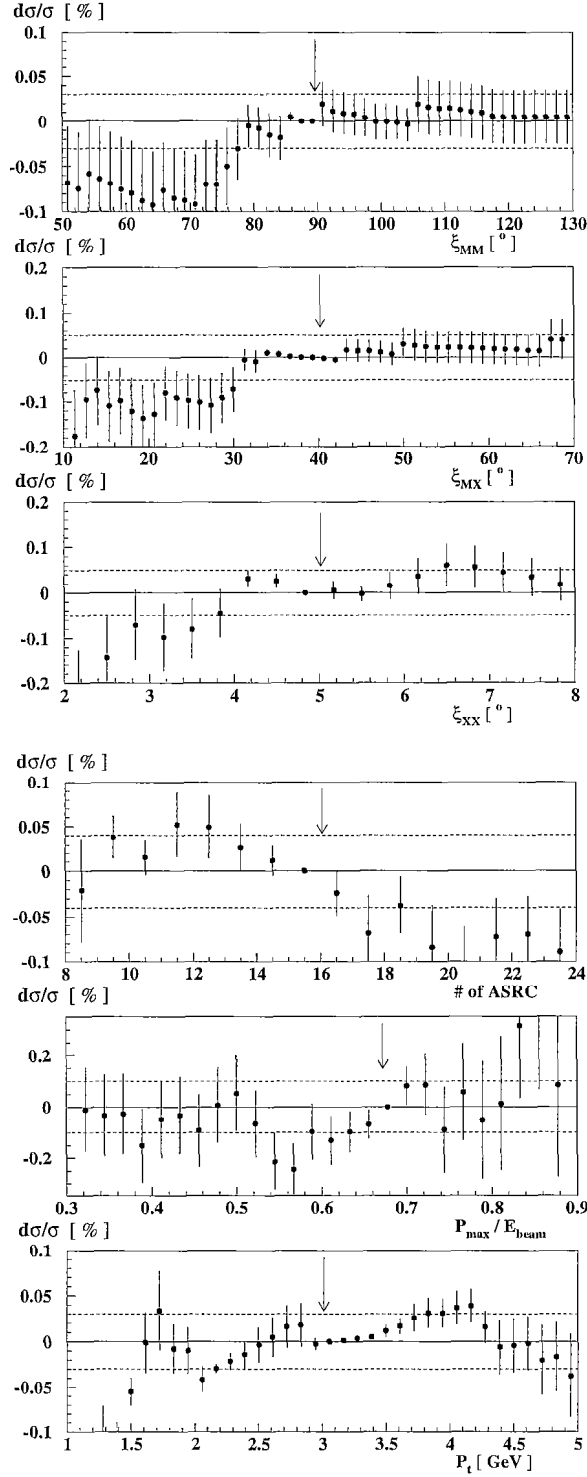
Figure 6.5: The change of the cross section for variations of the selection cuts. First the cuts on the acollinearity for the different samples are shown. Below are the cuts on the number of clusters in the calorimeters, on the maximum momentum of the muon for the MM and MX sample and the cut on the transverse momentum for the XX sample. The placement of the cut is marked by an arrow. The dashed line represents the systematic error assigned for each cut. Shown are the results for $\sqrt{s}$=91.29 GeV.

$\sqrt{s}$ [GeV]	systematic error [%]					
	sel. cuts	trigger eff.	bkgd. subtr.	MC stat.	$\mathcal{L}$ meas.	Σ
91.31	0.37	0.09	0.05	0.20	0.14	0.45
89.45	0.38	0.06	0.06	0.24	0.14	0.48
91.29	0.34	0.05	0.04	0.17	0.14	0.41
92.98	0.38	0.06	0.06	0.24	0.14	0.48
130.0	2.2	0.1	0.4	0.8	0.3	2.4
$\sqrt{s'}$>110.5	2.2	0.1	1.5	0.9	0.3	2.9
135.9	2.1	0.1	0.6	0.8	0.3	2.4
$\sqrt{s'}$>115.5	1.8	0.1	1.5	1.0	0.3	2.7
161.3	2.3	0.1	1.1	0.6	0.6	2.7
$\sqrt{s'}$>137.1	2.6	0.1	1.6	0.7	0.6	3.2
172.1	3.4	0.1	1.7	0.6	0.6	3.9
$\sqrt{s'}$>146.3	2.3	0.1	1.8	0.7	0.6	3.1
182.7	3.2	0.2	1.8	0.6	0.5	3.8
$\sqrt{s'}$>155.3	3.2	0.1	1.6	0.7	0.5	3.7

Table 6.5: The contributions to the overall systematic errors for the different data taking periods. They arise from the selection cuts, the trigger efficiency, the background subtraction, the Monte Carlo statistics and the luminosity measurement.

Chapter 7

Forward-backward asymmetry

The forward-backward asymmetry, A_{fb}, is defined as:

$$A_{\text{fb}} = \frac{\sigma_f - \sigma_b}{\sigma_f + \sigma_b}, \tag{7.1}$$

where $\sigma_f(\sigma_b)$ is the cross section for events with the fermion, μ^-, scattered into the hemisphere which is forward (backward) with respect to the e^--beam direction (figure 2.3). Events with hard initial state photons are removed from the sample by requiring that the acollinearity angle of the event is less than 15°. The differential cross section in the angular region $|\cos\theta| < 0.9$ can be approximated by the lowest order angular dependence to sufficient precision:

$$\frac{d\sigma}{d\cos\theta} \propto \frac{3}{8}\left(1 + \cos^2\theta\right) + A_{\text{fb}}\cos\theta, \tag{7.2}$$

with $\cos\theta$ being the polar angle of the final state fermion with respect to the e^--beam direction.

For each data set the forward-backward asymmetry is determined from a maximum likelihood fit where the likelihood function is defined as the product over the selected events i of the differential cross section evaluated at their respective scattering angle $\cos\theta_i$:

$$L = \prod_i \left(\frac{3}{8}\left(1 + \cos^2\theta_i\right) + \left(1 - 2\kappa_i\right) A_{\text{fb}}\cos\theta_i\right). \tag{7.3}$$

The probability of charge confusion for a specific event, κ_i, is included in the fit. The determination of κ_i is explained in the following section.

7.1 Charge Assignment

The bending direction of the trajectory in the muon chambers yields the charge of the muon. Besides its dependence on the transverse momentum the charge measurement strongly depends on the number of muon chamber segments used in the reconstruction. If both muons of the MM sample are assigned the same charge but have a different number of muon chamber segments, the charge of the muon with the lower number of used segments is flipped and the event can be

	P_{cc_M} (triplets) [%]		
	barrel	S-region	T-region
Data 1995	0.31±0.21	3.24±1.71	5.91±2.15

	P_{cc_M} (doublets) [%]	
	barrel	endcap
Data 1995	0.99±1.04	16.13±5.51

	P_{cc_X} [%]	
	barrel	endcap
Data 1995	4.32±0.35	5.42±0.79

Table 7.1: The charge confusion for triplets and doublets and for muons identified as MIPs. The charge confusions are given for different polar angular regions.

classified as either forward or backward. The fraction of events where both muons are assigned the same charge and have the same number of segment is used to determine the probability, P_{cc_M}, that one muon is assigned the wrong charge [61]. This is performed separately for triplets and doublets in different polar angular regions (table 7.1):

$$P^i_{cc_M} = \frac{1}{2} \frac{N^i_{cc}}{N^i_{all}}, \qquad (7.4)$$

where N^i_{all} are all events of a certain category (e.g. barrel triplets) and N^i_{cc} is the corresponding number of events where both muons were assigned the same charge.

For muons without a muon chamber track, the measured curvature in the muon chambers cannot be used to determine the charge. Therefore the orientation of the event is determined by means of the inner tracking chamber [62]. A straight line is fitted to each of the two tracks. The quantity $\Delta\Phi = \sin(\Phi_1 - \Phi_2)$ is then obtained using the azimuthal angles, Φ_i, of these straight lines. The sign of $\Delta\Phi$ is equal the charge of the first track. The reliability of the method is verified taking events of the MM sample with an acollinearity ξ <5°, in accordance with the ξ-cut on the XX sample. In addition both muons have to be triplets and have to have opposite charges. Figure 7.1 shows $\Delta\Phi$ for this sub-sample. It can be seen that the muon charges are well separated. The charges for this MM sub-sample are well known, since the charge confusion for triplets is sufficiently small. The fraction of events with a different event orientation given by the two methods, N_{cc}, can be used to determine the probability, P_{cc_X}, that one muon is assigned the wrong charge:

$$P_{cc_X} = \frac{1}{2} \frac{N_{cc}}{N_{all}}. \qquad (7.5)$$

The probability, that one muon of the XX category is assigned the wrong charge is shown in table 7.1. In the barrel the probability of charge confusion for triplets is about seven times smaller than for muons identified as MIPs with the charge determined using $\Delta\Phi$. In the T-region the $\Delta\Phi$ method is more precise than the
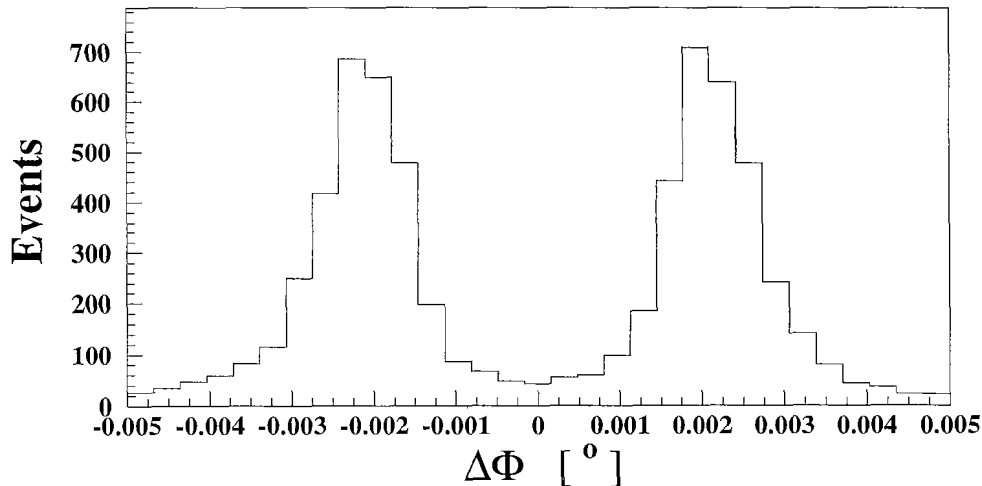
Figure 7.1: The separation of muon charges using $\Delta\Phi$ of the inner tracking chamber.

charge determination from the curvature of the trajectory in the muon chambers. This is due to the multiple scattering in the iron door.

Figure 7.2 shows the dependence of the charge confusion of an event on its position in the inner tracking chamber. For events that are closer to the wire planes $\Delta\Phi$ has a higher probability for charge confusion.

The probability, P_{cc}, that both measurements are wrong, but are consistent with each other can be derived from the product of the single probabilities:

$$P_{\mathrm{cc}} = P_{\mathrm{cc}}^{i} \cdot P_{\mathrm{cc}}^{j}. \tag{7.6}$$

The fraction of charge confused events, κ, is calculated from the probability, P_{cc}, that both measurements are wrong, divided by the fraction of events remaining for the measurement:

$$\kappa = \frac{P_{\mathrm{cc}}}{1 - \dfrac{N_{\mathrm{cc}}}{N_{\mathrm{all}}}} = \frac{P_{\mathrm{cc}}^{i} P_{\mathrm{cc}}^{j}}{1 - \left(P_{\mathrm{cc}}^{i} + P_{\mathrm{cc}}^{j} \right)}. \tag{7.7}$$

In the case where both muons of an event are from the same category, e.g. both are barrel triplets, equation 7.7 reduces to:

$$\kappa = \frac{P_{\mathrm{cc}}^{i\,2}}{1 - 2P_{\mathrm{cc}}^{i}}. \tag{7.8}$$

The probability of mis-assignment of the event orientation, κ_{i}, is then calculated for the different event samples:

$$\kappa_{\mathrm{MM}} = \frac{P_{\mathrm{cc_M}}^{i} P_{\mathrm{cc_M}}^{j}}{1 - P_{\mathrm{cc_M}}^{i} - P_{\mathrm{cc_M}}^{j}}, \tag{7.9}$$

$$\kappa_{\mathrm{MX}} = \frac{P_{\mathrm{cc_M}}^{i} P_{\mathrm{cc_X}}^{j}}{1 - P_{\mathrm{cc_M}}^{i} - P_{\mathrm{cc_X}}^{j}}, \tag{7.10}$$

71
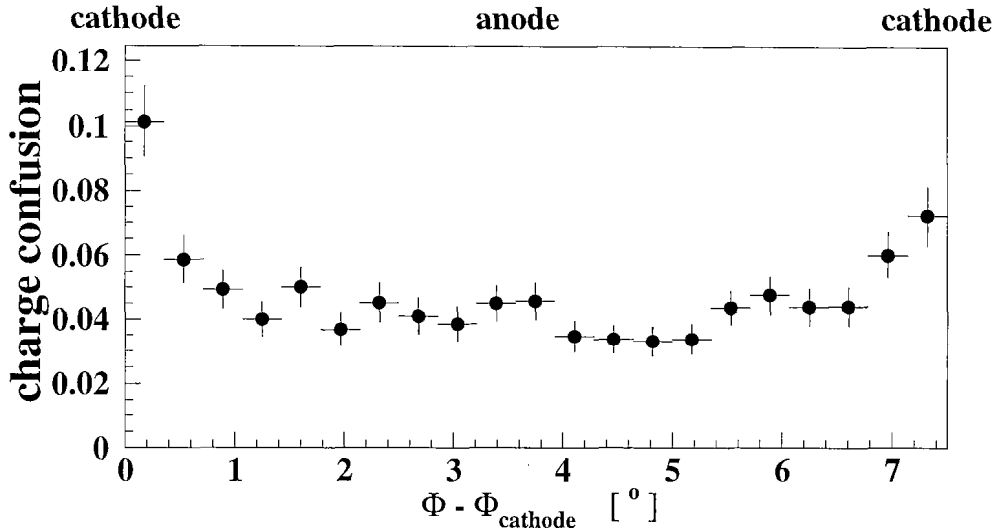
Figure 7.2: The dependence of the charge confusion on the position of the event in the inner tracking chamber. Shown is the probability for charge confusion with respect to the next cathode wire plane. The largest probability for charge confusion is close the cathode wire planes.

$$\kappa_{XX} = \frac{P^i_{cc_X} P^j_{cc_X}}{1 - P^i_{cc_X} - P^j_{cc_X}}. \tag{7.11}$$

The probability for charge confusion of a specific event is given in table 7.2 for different event categories. They are determined from the data of 1995. The charge confusion increases for the data taken at $\sqrt{s} > 100$ GeV. Due to the higher momentum of the muon, its trajectory is less bent and thus the probability for charge confusion is much larger than for center-of-mass energies around the Z mass. Still it is only of the order of $0.04 \pm 0.03\%$ at $\sqrt{s} \approx m_Z$ and about $0.5 \pm 1.0\%$ at $\sqrt{s} > 100$ GeV.

7.2 Background subtraction

The background contribution of other processes to the muon-pair selection has been discussed in section 6.2. Due to the tighter acollinearity cut at 15° the contributions of the different processes are partially changed. The background from the process $e^+e^- \to e^+e^-\mu^+\mu^-(\gamma)$ and from cosmic muons is reduced by $\approx 50\%$. Cosmic muons generally do not traverse the detector at $z=0$ and thus appear to be kinked in the r-θ-plane. The major fraction of the background arises from tau-pair production. The forward-backward asymmetry of tau-pairs has been measured to be the same as for muon-pairs [63], in agreement with lepton universality. However, the tau-pair events passing the selection for muon-pairs have a slightly different forward-backward asymmetry. The asymmetries of the background were determined using the same fitting procedure as for muon-pairs. The asymmetry for muon-pairs obtained from the fit, A^{fit}_{fb}, is combined with the forward-backward asymmetries, $A^{bkgd^i}_{fb}$, of the different background processes and

Data 1995	probability of charge confusion, κ [%]		
	barrel	S-region	T-region
MM triplets	< 0.01	0.11±0.09	0.40±0.22
MM doublets	0.01±0.02	3.84±2.30	
MX triplet	0.01±0.01	0.19±0.11	0.36±0.15
XX	0.20±0.02	0.33±0.07	

$\sqrt{s}$ [GeV]	charge confusion [%]
91.31	0.04±0.03
89.45	0.08±0.04
91.29	0.05±0.03
92.98	0.05±0.04
130.0	0.4±0.7
$\sqrt{s'}$>110.5	0.4±0.7
135.9	0.4±0.7
$\sqrt{s'}$>115.5	0.8±1.4
161.3	0.6±1.2
$\sqrt{s'}$>137.1	0.3±0.6
172.1	1.0±1.8
$\sqrt{s'}$>146.3	1.4±2.6
182.7	0.4±0.8
$\sqrt{s'}$>155.3	0.4±0.8

Table 7.2: Above: The probability of charge confusion for a specific event in the different polar angular regions for the data of 1995. Below: The overall charge confusion per data taking period.

$\sqrt{s}$ [GeV]	C_{bkgd}	C_{ex}
91.31	0.998±0.010	-
89.45	1.009±0.002	-
91.29	1.001±0.008	-
92.98	1.001±0.002	-
130.0	1.03±0.02	0.839±0.012
$\sqrt{s'}$>110.5	1.10±0.02	-
135.9	1.07±0.02	0.838±0.012
$\sqrt{s'}$>115.5	1.07±0.02	-
161.3	1.07±0.06	0.828±0.012
$\sqrt{s'}$>137.1	1.11±0.05	-
172.1	1.18±0.19	0.817±0.012
$\sqrt{s'}$>146.3	1.17±0.11	-
182.7	1.31±0.08	0.826±0.013
$\sqrt{s'}$>155.3	1.15±0.03	-

Table 7.3:   The background correction factors for the different data taking periods and the extrapolation factors for the total event sample at $\sqrt{s}$>100 GeV. The extrapolation factor correct for a distortion of the differential cross section due to events with hard initial state photons.

their weight, ω_i. The background-corrected forward-backward asymmetry is then calculated as:

$$A_{\mathrm{fb}}^{\mathrm{BgC}} = \frac{A_{\mathrm{fb}}^{\mathrm{fit}} - \sum_i \omega_i A_{\mathrm{fb}}^{\mathrm{bkgd}^i}}{1 - \sum_i \omega_i}. \qquad (7.12)$$

The error is derived in equation A.19. The ratio of the background-corrected asymmetry, $A_{\mathrm{fb}}^{\mathrm{BgC}}$, and the fitted asymmetry, $A_{\mathrm{fb}}^{\mathrm{fit}}$, yields the background correction factor:

$$C_{\mathrm{bkgd}} \equiv \frac{A_{\mathrm{fb}}^{\mathrm{BgC}}}{A_{\mathrm{fb}}^{\mathrm{fit}}}. \qquad (7.13)$$

This factor is not used for any calculation but to illustrate the impact of the background on the asymmetry and to compare the background corrections of different energy points. The background correction factors for the different data taking periods are shown in table 7.3. The background correction for $\sqrt{s} \approx m_Z$ is almost negligible, for $\sqrt{s}$>100 GeV it is of the order of 1.1±0.1 .

7.3 A_{fb} for muon-pairs at $\sqrt{s}$ >100 GeV

The determination of the forward-backward asymmetry for muon pairs at $\sqrt{s}$>100 GeV follows the procedure described in the sections above. However, as with the cross section measurement, the forward-backward asymmetry is calculated for both the total and the high energy sample. The cut of 15° on the acollinearity of the event is not applied since events with hard initial state photons are already

rejected in the high energy sample requiring the effective center-of-mass energy, $\sqrt{s'}$, to be higher than $0.85\sqrt{s}$.

For energies of $\sqrt{s'}>0.85\sqrt{s}$ also the background originating from events with ISR photons has to be taken into consideration. This background asymmetry, $A_{\mathrm{fb}}^{\mathrm{isr}}$, is determined by counting events in the forward, $N_{\mathrm{f}}^{\mathrm{isr}}$, and backward, $N_{\mathrm{b}}^{\mathrm{isr}}$, hemispheres (see also equation A.18) is:

$$A_{\mathrm{fb}}^{\mathrm{isr}} = \frac{N_{\mathrm{f}}^{\mathrm{isr}} - N_{\mathrm{b}}^{\mathrm{isr}}}{N_{\mathrm{f}}^{\mathrm{isr}} + N_{\mathrm{b}}^{\mathrm{isr}}}, \tag{7.14}$$

$$\Delta A_{\mathrm{fb}}^{\mathrm{isr}} = 2\sqrt{\frac{N_{\mathrm{f}}^{\mathrm{isr}} N_{\mathrm{b}}^{\mathrm{isr}}}{(N_{\mathrm{f}}^{\mathrm{isr}} + N_{\mathrm{b}}^{\mathrm{isr}})^3}}. \tag{7.15}$$

For the total event sample the differential cross section (equation 7.2) is distorted by hard ISR photons. For the high energy sample the measured and background-corrected quantity, $A_{\mathrm{fb}}^{\mathrm{BgC}}$, directly gives the forward-backward asymmetry for the full solid angle, A_{fb}. To extract A_{fb} for the total event sample a correction, $C_{\mathrm{ex}} \equiv A_{\mathrm{fb}}/A_{\mathrm{fb}}^{\mathrm{BgC}} \approx 0.83 \pm 0.01$, obtained from Monte Carlo is applied. The exact correction factors are given table 7.3.

7.4   Results of the measurement

The method used to extract the forward-backward asymmetry, $A_{\mathrm{fb}}^{\mathrm{fit}}$, from the data is a likelihood fit of the angular distribution in first order Born approximation (equation 7.2). The likelihood for a single event is defined as:

$$P_i = \frac{3}{8}\left(1 + \cos^2\theta_i\right) + A_{\mathrm{fb}}^{\mathrm{fit}}\cos\theta_i.$$

The likelihood function L is then given as the product of the single probabilities. In the fitting procedure the logarithm of the likelihood function is formed to determine the value of the $A_{\mathrm{fb}}^{\mathrm{fit}}$ for which $\ln L$ reaches its maximum:

$$\ln L = \sum_{i=1}^{n} \ln P_i(A_{\mathrm{fb}}^{\mathrm{fit}}) = \sum_{i=1}^{n} \ln\left(\frac{3}{8}\left(1 + \cos^2\theta_i\right) + A_{\mathrm{fb}}^{\mathrm{fit}}\cos\theta_i\right)$$

A limited detector acceptance and charge confusion change the likelihood function. It can be corrected for these effects by using:

$$\ln L = \sum_{i=1}^{n} \frac{1}{\epsilon_i} \ln\left((1 - \kappa_i)P_i(A_{\mathrm{fb}}^{\mathrm{fit}}) + \kappa_i P_i(-A_{\mathrm{fb}}^{\mathrm{fit}})\right),$$

with ϵ_i the acceptance and κ_i the probability of charge confusion for the event. An acceptance correction is not necessary in the case of a symmetric or charge-independent acceptance $\epsilon_i(q\cos\theta) = \epsilon_i(-q\cos\theta)$. The likelihood function is then given by equation 7.3.
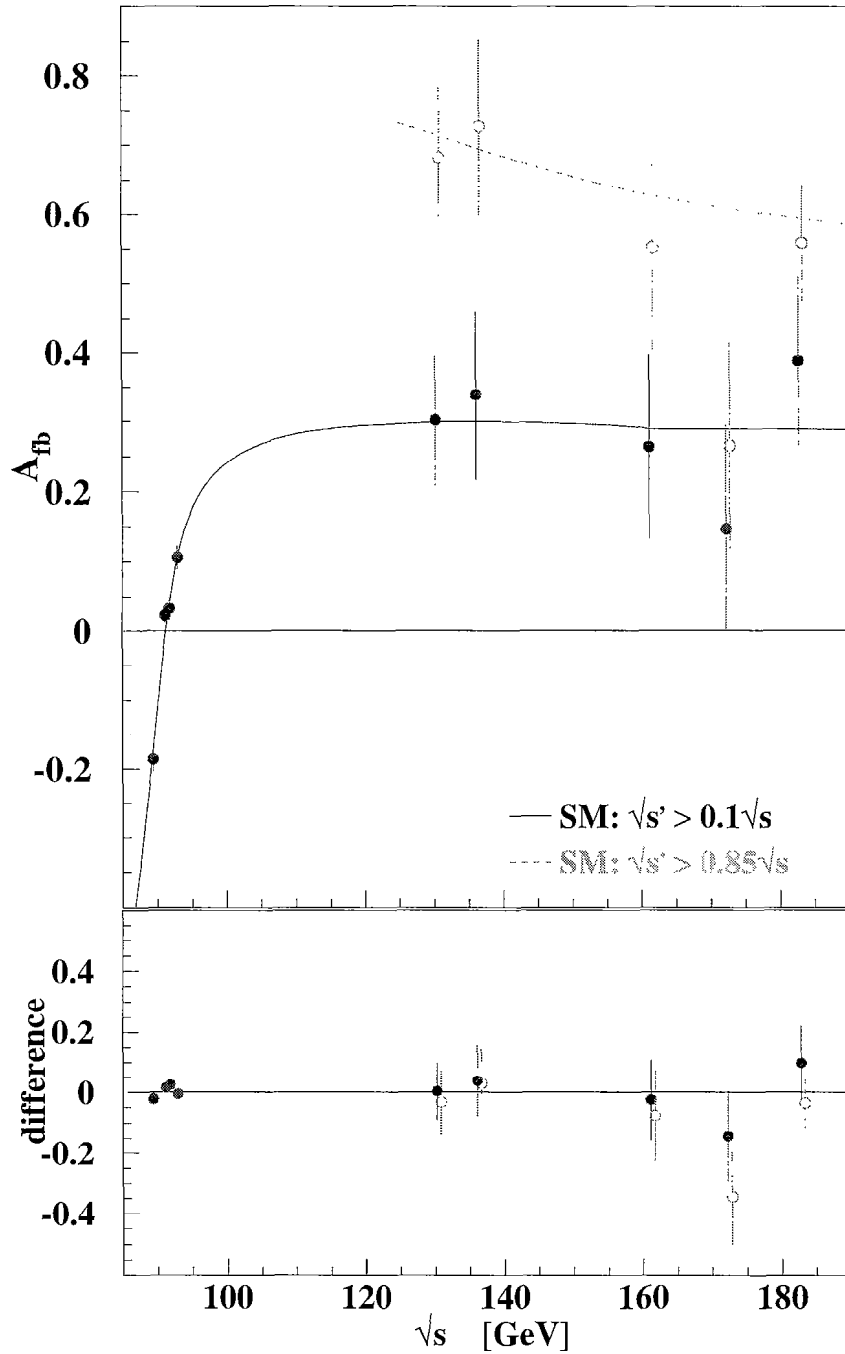
Figure 7.3: The comparison of the standard model predictions for the process $e^+e^- \to \mu^+\mu^-$ (γ) to the forward-backward asymmetries measured at nine different center-of-mass energies. The solid and dashed lines are the Standard Model predictions for $\sqrt{s'}>0.1\sqrt{s}$ and $\sqrt{s'}>0.85\sqrt{s}$, respectively. The solid and open symbols represent the respective measurements. The measurements at center-of-mass energies around the Z resonance have been corrected to correspond to $\sqrt{s'}>0.1\sqrt{s}$. The differences between the measured and the predicted forward-backward asymmetries are shown below.

$\sqrt{s}$ [GeV]	$N_{\rm f}$	$N_{\rm b}$	$A_{\rm fb}\pm$(stat.)$\pm$(syst.)	$A_{\rm fb}^{\rm SM}$
91.31	2904	2739	$0.0224^{+0.0133}_{-0.0133}\pm0.0007$	0.0086
89.45	1130	1556	$-0.1752^{+0.0190}_{-0.0188}\pm0.0012$	-0.1623
91.29	2004	1854	$0.0300^{+0.0161}_{-0.0161}\pm0.0009$	0.0076
92.98	2311	1882	$0.1042^{+0.0154}_{-0.0155}\pm0.0026$	0.1099
130.0	64	30	$0.303^{+0.092}_{-0.099}\pm0.016$	0.297
$\sqrt{s'}{>}110.5$	39	5	$0.682^{+0.099}_{-0.125}\pm0.036$	0.716
135.9	51	25	$0.338^{+0.107}_{-0.116}\pm0.014$	0.297
$\sqrt{s'}{>}115.5$	29	5	$0.726^{+0.095}_{-0.133}\pm0.036$	0.696
161.3	56	33	$0.264^{+0.114}_{-0.121}\pm0.020$	0.286
$\sqrt{s'}{>}137.1$	28	11	$0.552^{+0.146}_{-0.173}\pm0.042$	0.628
172.1	39	30	$0.146^{+0.139}_{-0.145}\pm0.028$	0.286
$\sqrt{s'}{>}146.3$	20	13	$0.265^{+0.171}_{-0.184}\pm0.035$	0.609
182.7	230	105	$0.387^{+0.117}_{-0.118}\pm0.029$	0.287
$\sqrt{s'}{>}155.3$	113	36	$0.559^{+0.085}_{-0.091}\pm0.022$	0.594

Table 7.4: The forward-backward asymmetries for the different data taking periods and their comparison with the Standard Model prediction. $N_{\rm f}$ and $N_{\rm b}$ are the number of events in the forward and backward hemisphere, respectively.

The number of events in the forward and backward directions and the measured forward-backward asymmetries are given in table 7.4.

The forward-backward charge asymmetries of the muon-pair production are measured for nine different center-of-mass energies between 89 and 183 GeV. For energies $\sqrt{s}{>}100$ GeV the asymmetries are given for the total and the high energy sample ($\sqrt{s'}{>}0.85\sqrt{s}$). All measurements are in good agreement with the Standard Model. The forward-backward asymmetries are determined with a precision better than 0.02 for center-of-mass energies around the Z mass and to about 0.15 for higher $\sqrt{s}$. For all measurements the statistical error dominates the error arising from systematic uncertainties.

A comparison with the standard model can be seen in figure 7.3. The measurements for effective center-of-mass energies $\sqrt{s'}{>}0.85\sqrt{s}$ are included in the figure. The lower figure shows the difference between the measured and the predicted forward-backward asymmetries. A good agreement between measurements and Standard Model predictions is found. Further L3 forward-backward asymmetry measurements of the muon-pair production at center-of-mass energies around the Z resonance are published in [63, 64]. The results presented here are in excellent agreement with these previous measurements.

7.5 Systematic errors

The uncertainties of the trigger efficiency, the selection cuts and of the luminosity determination have no influence on the measurement of the forward-backward asymmetry. The systematic uncertainty of the background correction is obtained from the errors on the background correction factor, $C_{\rm bkgd}$, and on the extrap-

$\sqrt{s}$ [GeV]	background correction	charge confusion	detector acceptance	momentum reconstruction	systematic error
91.31	0.0002	0.00002	0.0007	0.00002	0.0007
89.45	0.0004	0.00028	0.0011	0.00018	0.0012
91.29	0.0002	0.00003	0.0009	0.00002	0.0009
92.98	0.0002	0.00010	0.0026	0.00010	0.0026
130.0	0.007	0.003	0.013	0.003	0.016
$\sqrt{s'}{>}110.5$	0.013	0.005	0.029	0.015	0.036
135.9	0.009	0.003	0.008	0.006	0.014
$\sqrt{s'}{>}115.5$	0.014	0.011	0.009	0.030	0.036
161.3	0.018	0.004	0.006	0.006	0.020
$\sqrt{s'}{>}137.1$	0.026	0.003	0.017	0.028	0.042
172.1	0.026	0.003	0.009	0.003	0.028
$\sqrt{s'}{>}146.3$	0.026	0.006	0.020	0.011	0.035
182.7	0.028	0.003	0.003	0.004	0.029
$\sqrt{s'}{>}155.3$	0.015	0.004	0.007	0.015	0.022

Table 7.5: The contributions to the systematic error on the measurement of the forward-backward asymmetry for all data taking periods.

olation factor, C_{ex} (table 7.3). For center-of-mass energies around the Z mass, this contribution amounts to about 0.0003 . The probability of charge confusion for an event amounts to $\approx$ 0.05% for the peak of the scan in 1995 (table 7.2). The correction of the asymmetry is $2\kappa A_{\mathrm{fb}}^{\mathrm{fit}}$ and yields an systematic uncertainty of 0.00003 .

The event orientation of the charge confused MM events is determined using the inner tracking chamber as for the XX sample. For the peak of the scan in 1995 an asymmetry of 0.1089±0.0888 is measured which is compatible with the determined asymmetry in table 7.4. Thus the charge confused events do not prefer a certain polar angular range and the detector acceptance is symmetric in $\cos\theta$. The uncertainty due to the detector acceptance is estimated to be half of the error weighted with the number of charge confused events. For the peak of the scan in 1995 this yields a systematic uncertainty of 0.0009 .

The influence of the reconstruction of the muon momentum on the asymmetry is checked using the MM-class events with a momentum of $0.4{<}p_{\mathrm{max}}{<}\frac{2}{3}E_{\mathrm{beam}}$ and an acollinearity of less than 2° to reject the background from tau-pair production. For the peak of the scan in 1995, these events represent 0.24±0.08% (forward) and 0.27±0.08% (backward) of all selected events in the MM and MX samples, i.e. the samples where the cut on p_{max} is applied. Since both numbers agree within their statistical error, the influence of the p_{max}-cut on the asymmetry is restricted to $0.0008 A_{\mathrm{fb}}$.

The different contributions to the systematic error on the forward-backward asymmetry are listed in table 7.5 for all data taking periods. For all data points at $\sqrt{s}\approx m_{\mathrm{Z}}$ the systematic error of <0.01 is smaller than the statistical error of about 0.015. Also for center-of-mass energies larger than 100 GeV the systematic error is much smaller than the statistical error.

7.6   Differential cross section

The differential cross section $d\sigma/d\cos\theta$ can be determined taking the scattering angles θ of all selected events. For center-of-mass energies, $\sqrt{s}$, around the mass of the Z, events with hard initial state photons are removed from the sample by requiring that the acollinearity angle of the event is less than 15°. The background subtraction and the acceptance correction, ϵ, are applied separately for each bin in $\cos\theta$. Only not charge confused events are taken for the measurement. The necessary acceptance correction is determined from the data. The differential cross section in a certain $\cos\theta$-bin i is given by:

$$\frac{d\sigma}{d\cos\theta}(\cos\theta^i) = \frac{N^i_{\text{sel}} - N^i_{\text{bkgd}}}{\epsilon^i \mathcal{L}} \cdot \frac{1}{\left|\cos\theta^i_{\text{max}} - \cos\theta^i_{\text{min}}\right|}, \tag{7.16}$$

where $\cos\theta^i_{\text{max}}$ and $\cos\theta^i_{\text{min}}$ are the borders of the $\cos\theta$-bin, N^i_{sel} and N^i_{bkgd} are the number of selected events and background events per bin, respectively.

The contributions to the systematic error arise from the muon-pair selection (0.6%), the luminosity measurement (0.1%) and the limited number of Monte Carlo events per $\cos\theta$-bin (1.5%). The systematic error per bin is estimated to be 1.6% . The statistical error depends on the number of selected events per $\cos\theta$-bin and is of the order of 8%. The differential cross sections are given in table 7.6 and their comparison with the Standard Model prediction is shown in figure 7.4. The measurements for the center-of-mass energies $\sqrt{s}$=91.31 GeV and $\sqrt{s}$=91.29 GeV are combined. There is good agreement between data and the Standard Model prediction. The Standard Model prediction was determined using the program ZFITTER [55] with the theory parameters m_Z=91.19 GeV, m_t=175 GeV and α_S=0.123 .
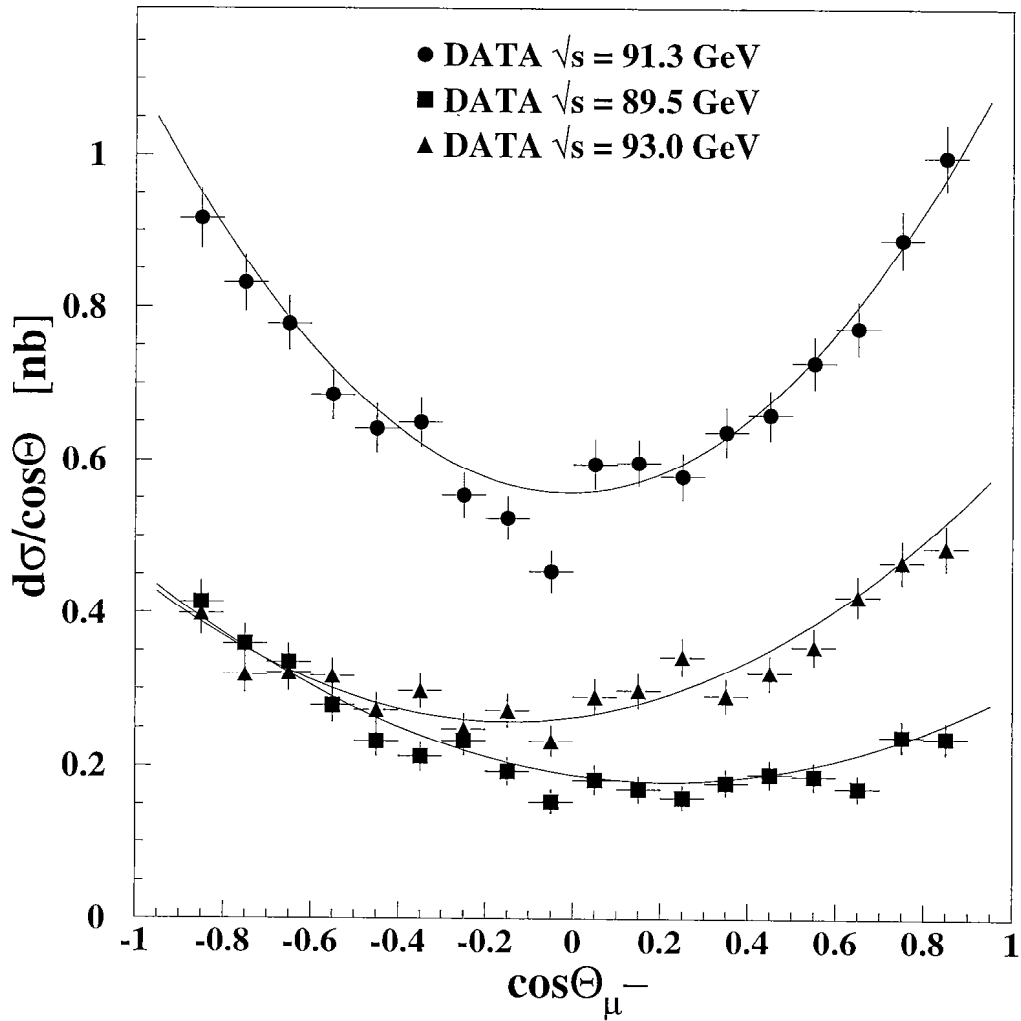
Figure 7.4: The differential cross section at center-of-mass energies around the Z mass for the process $e^+e^- \to \mu^+\mu^-(\gamma)$ and comparison with the Standard Model.

	differential cross section [nb]		
	$\sqrt{s}$= 89.452 GeV	$\sqrt{s}$= 91.302 GeV	$\sqrt{s}$= 92.983 GeV
-0.9<cos θ<-0.8	0.414±0.029	0.916±0.0366	0.399±0.028
-0.8<cos θ<-0.7	0.359±0.026	0.831±0.0335	0.319±0.024
-0.7<cos θ<-0.6	0.335±0.025	0.778±0.0326	0.321±0.024
-0.6<cos θ<-0.5	0.279±0.022	0.685±0.0310	0.316±0.024
-0.5<cos θ<-0.4	0.233±0.020	0.641±0.0297	0.272±0.022
-0.4<cos θ<-0.3	0.213±0.019	0.650±0.0296	0.298±0.023
-0.3<cos θ<-0.2	0.233±0.020	0.554±0.0279	0.248±0.021
-0.2<cos θ<-0.1	0.193±0.018	0.524±0.0265	0.272±0.022
-0.1<cos θ<0.0	0.153±0.016	0.454±0.0240	0.233±0.020
0.0<cos θ<0.1	0.182±0.019	0.595±0.0300	0.290±0.024
0.1<cos θ<0.2	0.170±0.017	0.597±0.0281	0.298±0.023
0.2<cos θ<0.3	0.159±0.017	0.577±0.0282	0.342±0.025
0.3<cos θ<0.4	0.178±0.017	0.637±0.0301	0.291±0.022
0.4<cos θ<0.5	0.189±0.018	0.659±0.0302	0.321±0.026
0.5<cos θ<0.6	0.187±0.018	0.727±0.0316	0.356±0.025
0.6<cos θ<0.7	0.171±0.017	0.773±0.0329	0.422±0.028
0.7<cos θ<0.8	0.239±0.021	0.889±0.0351	0.467±0.029
0.8<cos θ<0.9	0.237±0.021	0.997±0.0383	0.486±0.031

Table 7.6: The differential cross sections for the center-of-mass energies around the mass of the Z. The measurements at $\sqrt{s}$=91.31 GeV and $\sqrt{s}$= 91.29 GeV are combined. The errors contain the statistical error and an systematic error of 1.6%.

Chapter 8

Determination of electroweak parameters

The measurements of all visible Z decay channels are used to calculate the electroweak parameters. For the determination of mass and width of the Z boson the measurement of the hadron cross section is the most sensitive one since its statistical and systematic uncertainties are the smallest of all decays. The determination of the electroweak parameters is based on the measurements of the cross sections and forward-backward asymmetries for the processes $e^+e^- \to e^+e^-(\gamma)$, $e^+e^- \to \mu^+\mu^-(\gamma)$, $e^+e^- \to \tau^+\tau^-(\gamma)$ and $e^+e^- \to q\bar{q}(\gamma)$ (cross sections only). The results are taken from [63, 64, 65, 66, 67]. The cross sections and forward-backward asymmetries for the muon-pair production since 1995 are taken from sections 6.4 and 7.4.

For the theoretical calculations the program ZFITTER [55] is used. It takes both the electroweak and the QED radiative corrections into account. The fitting of the theory parameters to the data is carried out with the EWAPIC program [60]. The χ^2 minimization is achieved using the package MINUIT [52]. The Standard Model predictions are calculated with the following parameters: m_t=175 GeV [58], m_H=300 GeV, α_S=0.123 [22] and α=1/128.896 [9].

The theoretical values for cross sections and forward-backward asymmetries obtained with any given set of electroweak parameters are first corrected for the effect of the LEP beam spread. The average beam spread is about 55$\pm$5 MeV [60]. The vector Δ then contains all differences between the measurements and the theoretical predictions and the χ^2 value is given as:

$$\chi^2 = \Delta^{\mathrm{T}} C^{-1} \Delta, \tag{8.1}$$

where the covariance matrix C takes all correlations into account. Finally the χ^2 is minimized with MINUIT. The electroweak parameters are the set of parameters that yield the smallest χ^2.

parameter	L3	L3 (muon channel)	Standard Model
m_Z [MeV]	91190 ± 3	91198 ± 13	-
Γ_Z [MeV]	2502 ± 4	2491 ± 20	2496
Γ_{had} [MeV]	1748 ± 4	-	1743
Γ_l [MeV]	84.07 ± 0.19	83.71 ± 0.64	83.92
χ^2 / DoF	89 / 96	26 / 22	

Table 8.1: Result on the fitting of the widths assuming lepton universality.

8.1 Mass and width of the Z boson

The Z-contribution to the total cross section is described by a Breit-Wigner function:

$$\sigma_{tot}(s) = 12\pi \frac{\Gamma_e \Gamma_f}{m_Z^2} \frac{s}{(s - m_Z^2)^2 + s^2 \Gamma_Z^2 / m_Z^2} \qquad (8.2)$$

The free parameters to be determined from the measured cross section are the mass of the Z, m_Z, its total width, Γ_Z, and the partial widths Γ_e, Γ_μ, Γ_τ and Γ_{had}. This ansatz sets the photon exchange as well as the interference between γ and Z exchange to their Standard Model values.

Table 8.1 shows mass, width and the partial decay widths of the Z boson, obtained first using the cross section measurements of all four processes and then using the cross sections of the muon-pair production only. In the second case, it is possible to derive the lepton decay width of the Z boson, Γ_l, from the product $\Gamma_e \Gamma_\mu$ of equation 8.2 by assuming lepton universality. The parameters, obtained using the muon channel only, are:

$$m_Z = 91198 \pm 13 \text{MeV},$$
$$\Gamma_Z = 2491 \pm 20 \text{MeV},$$
$$\Gamma_l = 83.71 \pm 0.64 \text{MeV}.$$

The errors contain both statistical and systematic uncertainties. The results obtained using the data of the muon channel are in good agreement with the general L3 results. Both agree well with the Standard Model prediction.

The partial decay width Γ_μ can also be fitted without the assumption of lepton universality. The partial widths for this case are shown in table 8.2. All three partial widths agree within their statistical errors and thus support the hypothesis of lepton universality of the electroweak neutral current.

8.2 Vector and axial-vector couplings

A second ansatz parametrizes the leptonic decay widths of the Z boson by means of its couplings to the leptons:

$$\Gamma_\mu = \frac{G_F \, m_Z^3}{6\pi\sqrt{2}} \left(\bar{g}_V^{\mu^2} + \bar{g}_A^{\mu^2} \right) (1 + \delta_{QED}), \qquad (8.3)$$

parameter	L3	Standard Model
Γ_e [MeV]	84.05±0.24	83.92
Γ_μ [MeV]	83.93±0.45	83.92
Γ_τ [MeV]	84.24±0.61	83.73
χ^2 / DoF	89 / 94	

Table 8.2: Result on the fitting of the partial leptonic decay widths assuming no lepton universality.

parameter	L3	L3 (muon channel)	Standard Model
m_Z [MeV]	91190±3	91196±13	-
Γ_Z [MeV]	2502±4	2488±20	2496
Γ_{had} [MeV]	1748±4	-	1743
$\bar{g}_A^l$	-0.5013+0.0006	-0.4999+0.0019	-0.5012
$\bar{g}_V^l$	-0.0399±0.0018	-0.0395±0.0020	-0.0360
χ^2 / DoF	145 / 171	42 / 48	

Table 8.3: Result on the fitting of the couplings assuming lepton universality.

where $\bar{g}_A$ and $\bar{g}_V$ are the effective vector and axial-vector coupling, respectively, and G_F is the Fermi coupling constant [3]. Having introduced the effective couplings, the forward-backward asymmetries can be calculated and included in the fit:

$$A_{fb} = 3\frac{\bar{g}_V^e \bar{g}_A^e}{\bar{g}_V^{e^2} + \bar{g}_A^{e^2}} \frac{\bar{g}_V^\mu \bar{g}_A^\mu}{\bar{g}_V^{\mu^2} + \bar{g}_A^{\mu^2}}. \tag{8.4}$$

Table 8.3 shows the vector and axial-vector couplings assuming lepton universality, obtained using first the measurements of all four processes and then the results of the muon-pair production only. The couplings, determined from muon-pair production only, are:

$$\bar{g}_A^l = -0.4999 \pm 0.0019,$$
$$\bar{g}_V^l = -0.0395 \pm 0.0022.$$

To determine the couplings separately for all leptons, the results of the process $e^+e^- \rightarrow e^+e^-(\gamma)$ have to be included since not only the $Z\mu\mu$ vertex but also the Zee vertex contributes to the muon-pair production $e^+e^- \rightarrow \mu^+\mu^-(\gamma)$. Table 8.4 shows the couplings for the different leptons disregarding lepton universality. In the case of the τ-lepton, the τ-polarization is taken into account to determine the vector coupling $\bar{g}_V^\tau$. The values used are $\mathcal{A}_\tau$=0.152±0.012 and $\mathcal{A}_e$=0.158±0.014 [12]. All results are in good agreement with each other and the Standard Model prediction.

Figure 8.1 shows the 68% confidence level contours in the $\bar{g}_A$-$\bar{g}_V$-plane at 68% confidence level for electrons, muons and taus. The contours for the three different leptons agree well and support the hypothesis of lepton universality.
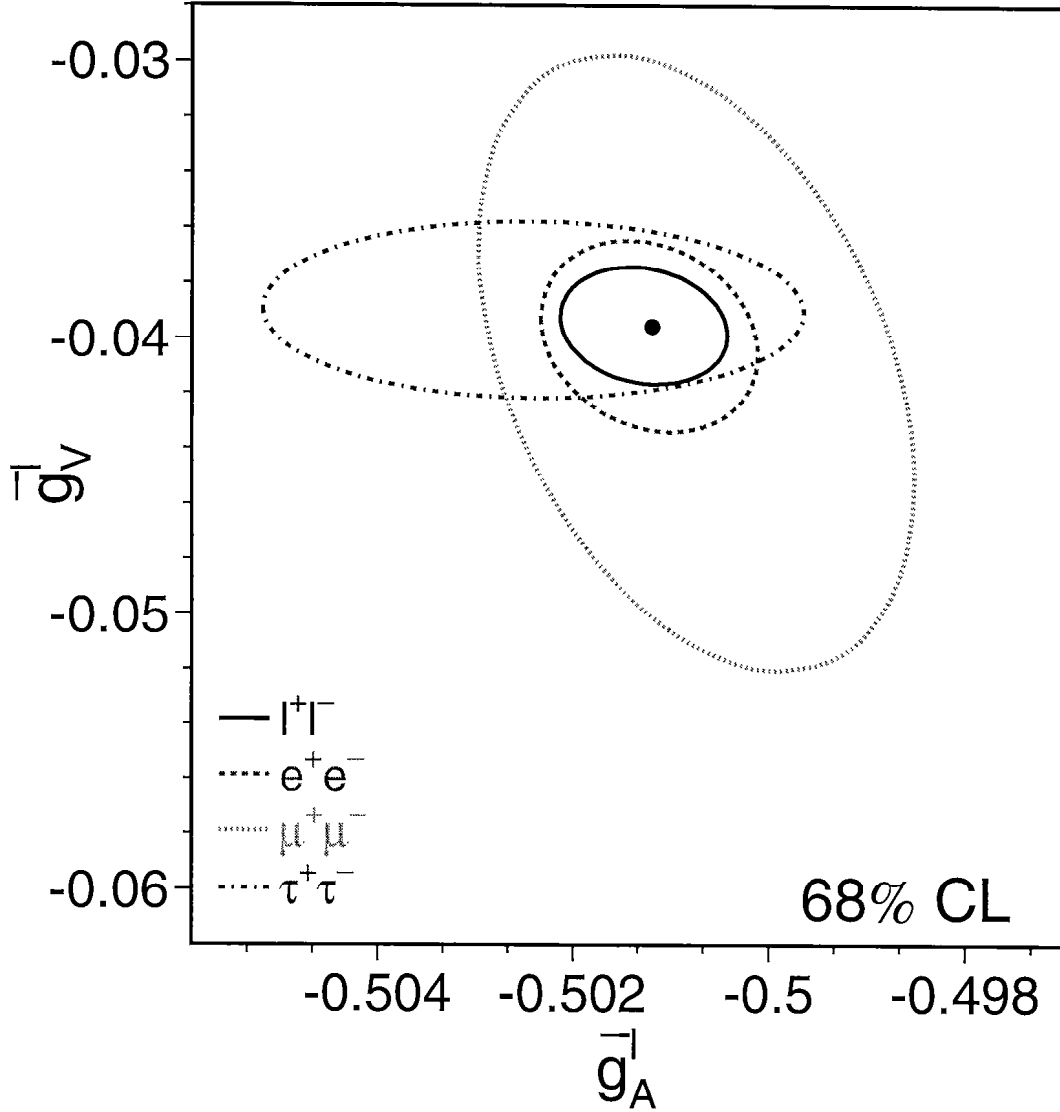
Figure 8.1: Contours in the $\bar{g}_A$-$\bar{g}_V$-plane at 68% confidence level for electrons, muons and taus, obtained from a fit to total cross sections, forward-backward and tau polarisation asymmetries. The solid line shows the contour assuming lepton universality and the solid circle indicates the central value.

parameter	L3	Standard Model
$\bar{g}_A^e$	-0.5012±0.0007	-0.5012
$\bar{g}_A^\mu$	-0.5007±0.0015	-0.5012
$\bar{g}_A^\tau$	-0.5024±0.0018	-0.5012
$\bar{g}_V^e$	-0.0400±0.0030	-0.0360
$\bar{g}_V^\mu$	-0.0409±0.0076	-0.0360
$\bar{g}_V^\tau$	-0.0395±0.0029	-0.0360
χ^2 / DoF	144 / 167	

Table 8.4: Result on the fitting of the couplings assuming no lepton universality.

8.3 Determination of γZ interference

The data are interpreted in the framework of an S-matrix ansatz [10, 66], which makes a minimum of theoretical assumptions. The programs SMATASY [56] together with ZFITTER [55] are used for the theoretical predictions and QED radiative corrections of cross sections and forward-backward asymmetries.

The lowest-order total cross section, σ_{tot}^0, and forward-backward asymmetry, A_{fb}^0, for $e^+e^- \to f\bar{f}$ [10] are:

$$\sigma_a^0(s) = \frac{4}{3}\pi\alpha^2 \left[\frac{g_f^a}{s} + \frac{j_f^a(s - \overline{m}_Z^2) + r_f^a s}{(s - \overline{m}_Z^2)^2 + \overline{m}_Z^2 \overline{\Gamma}_Z^2} \right] \quad \text{for } a = \text{tot}, \text{fb}$$

$$A_{\text{fb}}^0(s) = \frac{3}{4} \frac{\sigma_{\text{fb}}^0(s)}{\sigma_{\text{tot}}^0(s)}.$$

The S-matrix ansatz defines the Z resonance using a Breit-Wigner denominator with s-independent width. In other approaches usually a Breit-Wigner denominator with s-dependent width is used which implies the following transformation of the values of the Z boson mass and width [10]: $m_Z = \overline{m}_Z + 34.1$ MeV and $\Gamma_Z = \overline{\Gamma}_Z + 0.9$ MeV. In the following the fit results are quoted after applying these transformations. The S-matrix parameters r_f, j_f and g_f scale the Z exchange, γZ interference and γ exchange contributions. Here the γ exchange contributions are fixed to their QED predictions.

The S-matrix parameters are determined in a χ^2 fit to all measurements from [63, 64, 65, 66, 67]. The cross sections and forward-backward asymmetries for the muon-pair production since 1995 are taken from sections 6.4 and 7.4. The fitted S-matrix parameters for electrons, muons, taus and hadrons are listed in table 8.5. The fits are performed with and without the assumption of lepton universality. The parameters obtained for the individual leptons are compatible with each other and support this assumption. Under the assumption of lepton universality the fitted hadronic γZ interference term is:

$$j_{\text{had}}^{\text{tot}} = 0.19 \pm 0.17,$$

which agrees with the Standard Model prediction of 0.22 . The fitted value for m_Z is:

$$m_Z = 91189 \pm 4\text{MeV}.$$

Figure 8.2 shows the 68% confidence level contours in the m_Z-$j_{\text{had}}^{\text{tot}}$-plane, under the assumption of lepton universality, for the data taken at center-of-mass energies around the Z pole (dashed line) and after including the measurements at $\sqrt{s} > 100$ GeV (solid line). The improvement arising from the high energy measurements is clearly visible. Both contours are in good agreement with the Standard Model prediction for $j_{\text{had}}^{\text{tot}}$ which is shown as the horizontal band.

All cross section and forward-backward asymmetry measurements as well as the measurement of $j_{\text{had}}^{\text{tot}}$, $\bar{g}_A$ and $\bar{g}_V$ are in agreement with the respective Standard Model predictions and support the hypothesis of lepton universality of the electroweak neutral current.

parameter	Non-universality	Universality	Standard Model
m_Z [MeV]	91189±4	91189±4	-
Γ_Z [MeV]	2501±4	2501±4	2497
r_{had}^{tot}	2.979±0.010	2.978±0.010	2.967
r_e^{tot}	0.1428±0.0008	-	
r_μ^{tot}	0.1428±0.0008	-	
r_τ^{tot}	0.1437±0.0011	-	
r_l^{tot}	-	0.1429±0.0006	0.1426
j_{had}^{tot}	0.18±0.17	0.19±0.17	0.22
j_e^{tot}	-0.034±0.045	-	
j_μ^{tot}	0.035±0.031	-	
j_τ^{tot}	0.060±0.036	-	
j_l^{tot}	-	0.029±0.021	0.004
r_e^{fb}	0.0022±0.0012	-	
r_μ^{fb}	0.0036±0.0006	-	
r_τ^{fb}	0.0043±0.0009	-	
r_l^{fb}	-	0.00351±0.00048	0.00267
j_e^{fb}	0.690±0.081	-	
j_μ^{fb}	0.826±0.041	-	
j_τ^{fb}	0.765±0.052	-	
j_l^{fb}	-	0.786±0.030	0.799
χ^2 / DoF	160 / 200	167 / 208	

Table 8.5: Results of the fits in the S-matrix framework with and without the assumption of lepton universality.
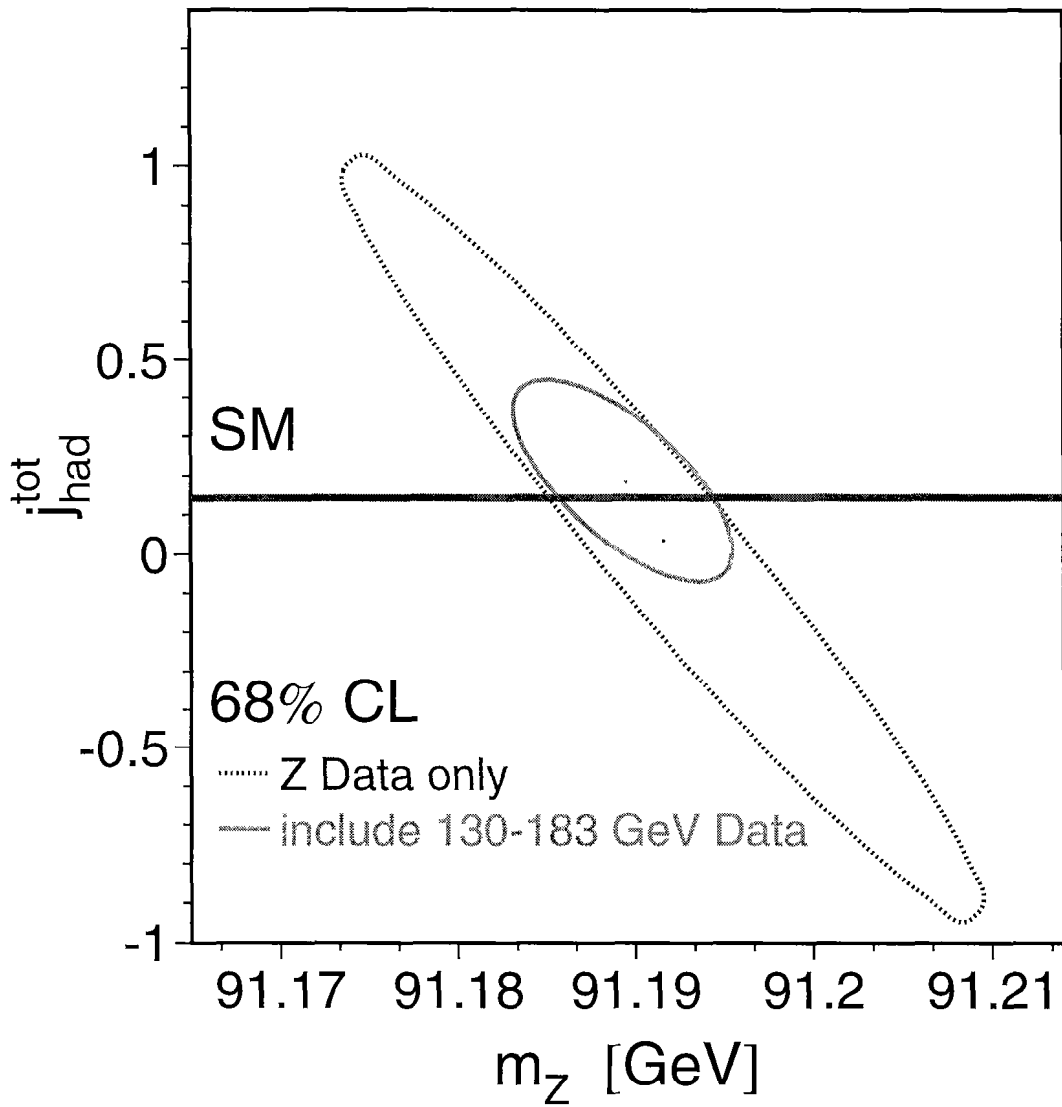
Figure 8.2: Contours in the m_Z-j_{had}^{tot}-plane at 68% confidence level under the assumption of lepton universality. The dashed line shows the Z data only. The solid line is obtained by including the results from 130 GeV through 172 GeV. The Standard Model prediction for j_{had}^{tot} is shown as the horizontal band.

Chapter 9

Conclusion

The cross sections and forward-backward asymmetries of muon-pair production from e^+e^- annihilation are measured at center-of-mass energies, $\sqrt{s}$, around the Z mass and at energies between 130 GeV and 183 GeV. The collected luminosities of 23.7 pb^{-1} and 88.5 pb^{-1} correspond to 16833 and 692 selected muon pairs in the two energy ranges, respectively. For the high energies, the cross sections and forward-backward asymmetries are measured for two effective center-of-mass energies, $\sqrt{s'}>0.1\sqrt{s}$ and $\sqrt{s'}>0.85\sqrt{s}$. The results of all measurements are in agreement with the Standard Model predictions.

Combining these results with the L3 results for hadron, electron and tau-pair production, the mass and width of the Z boson are determined under the assumption of lepton universality. The results obtained are:

$$m_Z = 91190 \pm 3\mathrm{MeV},$$
$$\Gamma_Z = 2502 \pm 4\mathrm{MeV}.$$

In addition, without assumption of lepton universality, the partial leptonic decay widths of the Z are calculated. Furthermore, by parametrizing the leptonic decay widths of the Z by means of its couplings to leptons, the effective vector and axial-vector couplings are obtained:

$$\bar{g}_A^l = -0.5013 \pm 0.0006,$$
$$\bar{g}_V^l = -0.0399 \pm 0.0018.$$

Interpreting the data in the framework of an S-matrix ansatz, the γZ interference term is determined under the assumption of lepton universality:

$$j_{\mathrm{had}}^{\mathrm{tot}} = 0.19 \pm 0.17.$$

All results agree with Standard Model predictions and support the hypothesis of lepton universality for the electroweak neutral current. The measurements provide an improved determination of mass and width of the Z boson and the γZ interference term with respect to a previous L3 publication [66].

Appendix A

Formulae

A.1 Variable definitions

Luminosity:	$\mathcal{L}$	
Cross section:	σ	
MC cross section prediction:	σ_{MC}	
Selected data events:	N_{sel}	$\Delta N_{sel} = \sqrt{N_{sel}}$
Background events in data sample:	N_{bkgd}	$\Delta N_{bkgd} = \sqrt{N_{bkgd}}$
Signal events:	$N_{sig} = N_{sel} - N_{bkgd}$	
Generated MC events:	N_{MC}^{gen}	$\Delta N_{MC}^{gen} = \sqrt{N_{MC}^{gen}}$
Total number of MC events:	N_{MC}^{tot}	$\Delta N_{MC}^{tot} = \sqrt{N_{MC}^{tot}}$
Selected MC events:	N_{MC}^{sel}	$\Delta N_{MC}^{sel} = \sqrt{N_{MC}^{sel}}$
Selected MC background events:	N_{sel}^{bkgd}	$\Delta N_{sel}^{bkgd} = \sqrt{N_{sel}^{bkgd}}$
Selection efficiency:	ϵ_{MC}	
Selected MC ISR background events:	N_{MCisr}^{sel}	
Cosmics per side band interval:	N_{int}^{i}	
Cosmics per selection interval:	N_{cos}^{i}	
Events in interval (SCN)	N_{int}^{SCN}	$\Delta N_{int}^{SCN} = \sqrt{N_{int}^{SCN}}$
Pre-scaled trigger events:	N_{ps}	$\Delta N_{ps} = \sqrt{N_{ps}}$
Level-2,3 trigger efficiency:	$\epsilon_{lev2,3}$	
Trigger efficiency:	ϵ_{trig}	
Syst. error from cut variation:	ΔC_{i}^{var}	
Charge confused events:	N_{cc}^{i}	
ISR events in forward direction:	N_{f}^{isr}	$\Delta N_{f}^{isr} = \sqrt{N_{f}^{isr}}$
ISR events in backward direction:	N_{b}^{isr}	$\Delta N_{b}^{isr} = \sqrt{N_{b}^{isr}}$
A_{fb} of the ISR events:	A_{fb}^{isr}	
A_{fb} of the fit for muon-pairs:	A_{fb}^{fit}	
Background fraction:	ω_{i}	
Sum of all background fractions	ω_{bkgd}	$\omega_{bkgd} = \sum_{i} \omega_{i}$
A_{fb} of the background processes:	$A_{fb}^{bkgd^{i}}$	
Background corrected A_{fb}^{fit}:	A_{fb}^{BgC}	
Background correction factor:	C_{bkgd}	

A.2 Formulae for cross section measurement

Error on ϵ_{MC}

$$\Delta\epsilon_{\text{MC}} = \frac{\sqrt{\frac{N_{\text{MC}}^{\text{sel}}\left(N_{\text{MC}}^{\text{tot}}-N_{\text{MC}}^{\text{sel}}\right)}{N_{\text{MC}}^{\text{tot}}}}}{N_{\text{MC}}^{\text{tot}}} = \frac{\sqrt{\frac{N_{\text{MC}}^{\text{sel}}N_{\text{MC}}^{\text{tot}}-N_{\text{MC}}^{\text{sel}^2}}{N_{\text{MC}}^{\text{tot}}}}}{N_{\text{MC}}^{\text{tot}}} = \sqrt{\frac{\frac{N_{\text{MC}}^{\text{sel}}N_{\text{MC}}^{\text{tot}}-N_{\text{MC}}^{\text{sel}^2}}{N_{\text{MC}}^{\text{tot}^2}}}{N_{\text{MC}}^{\text{tot}}}}$$

$$= \sqrt{\frac{\frac{N_{\text{MC}}^{\text{sel}}}{N_{\text{MC}}^{\text{tot}}} - \frac{N_{\text{MC}}^{\text{sel}^2}}{N_{\text{MC}}^{\text{tot}^2}}}{N_{\text{MC}}^{\text{tot}}}} = \sqrt{\frac{\epsilon_{\text{MC}} - \epsilon_{\text{MC}}^2}{N_{\text{MC}}^{\text{tot}}}} = \sqrt{\frac{\epsilon_{\text{MC}}\left(1-\epsilon_{\text{MC}}\right)}{N_{\text{MC}}^{\text{tot}}}} \tag{A.1}$$

Error on $\epsilon_{\text{lev2,3}}$

$$\Delta\epsilon_{\text{lev2,3}} = \frac{\sqrt{\frac{N_{\text{ps}}\left(N_{\text{sel}}-N_{\text{ps}}\right)}{N_{\text{sel}}}}}{N_{\text{sel}}} = \frac{\sqrt{\frac{N_{\text{ps}}N_{\text{sel}}-N_{\text{ps}}^2}{N_{\text{sel}}}}}{N_{\text{sel}}} = \sqrt{\frac{\frac{N_{\text{ps}}N_{\text{sel}}-N_{\text{ps}}^2}{N_{\text{sel}}^2}}{N_{\text{sel}}}}$$

$$= \sqrt{\frac{\frac{N_{\text{ps}}}{N_{\text{sel}}} - \frac{N_{\text{ps}}^2}{N_{\text{sel}}^2}}{N_{\text{sel}}}} = \sqrt{\frac{\epsilon_{\text{lev2,3}} - \epsilon_{\text{lev-2,3}}^2}{N_{\text{sel}}}} = \sqrt{\frac{\epsilon_{\text{lev2,3}}\left(1-\epsilon_{\text{lev2,3}}\right)}{N_{\text{sel}}}} \tag{A.2}$$

Number of background events and error on N_{bkgd}^i

$$N_{\text{bkgd}}^i = N_{\text{sel}}^{\text{bkgd}}\, f_{\text{scal}}^{\text{MC}} = N_{\text{sel}}^{\text{bkgd}}\,\frac{\mathcal{L}}{\mathcal{L}_{\text{MC}}} = N_{\text{sel}}^{\text{bkgd}}\,\frac{\mathcal{L}}{\frac{N_{\text{MC}}^{\text{gen}}}{\sigma_{\text{MC}}}} = N_{\text{sel}}^{\text{bkgd}}\,\frac{\mathcal{L}\sigma_{\text{MC}}}{N_{\text{MC}}^{\text{gen}}} \tag{A.3}$$

$$\Delta N_{\text{bkgd}}^i = N_{\text{MC}}^{\text{gen}} \times \frac{\sqrt{\frac{N_{\text{sel}}^{\text{bkgd}}\left(N_{\text{MC}}^{\text{gen}}-N_{\text{sel}}^{\text{bkgd}}\right)}{N_{\text{MC}}^{\text{gen}}}}}{N_{\text{MC}}^{\text{gen}}} = \sqrt{\frac{N_{\text{sel}}^{\text{bkgd}}\left(N_{\text{MC}}^{\text{gen}}-N_{\text{sel}}^{\text{bkgd}}\right)}{N_{\text{MC}}^{\text{gen}}}} \tag{A.4}$$

Number of Cosmics, N_{cosmic}, and ΔN_{cosmic}

$$N_{\text{cosmic}} = \frac{\frac{N_{\text{cos}}^{\text{SCN}}}{\Delta N_{\text{cos}}^{\text{SCN}^2}} + \frac{N_{\text{cos}}^{\text{DCA}}}{\Delta N_{\text{cos}}^{\text{DCA}^2}}}{\frac{1}{\Delta N_{\text{cos}}^{\text{SCN}^2}} + \frac{1}{\Delta N_{\text{cos}}^{\text{DCA}^2}}} \tag{A.5}$$

$$\Delta N_{\text{cosmic}} = \sqrt{\frac{1}{\frac{1}{\Delta N_{\text{cos}}^{\text{SCN}^2}} + \frac{1}{\Delta N_{\text{cos}}^{\text{DCA}^2}}}} \tag{A.6}$$

Error on ϵ_{isr}

$$\Delta\epsilon_{isr} = \frac{\sqrt{\dfrac{N^{sel}_{MCisr}\left(N^{sel}_{MC}-N^{sel}_{MCisr}\right)}{N^{sel}_{MC}}}}{N^{sel}_{MC}} = \frac{\sqrt{\dfrac{N^{sel}_{MCisr}N^{sel}_{MC}-N^{sel^2}_{MCisr}}{N^{sel}_{MC}}}}{N^{sel}_{MC}} = \sqrt{\dfrac{\dfrac{N^{sel}_{MCisr}N^{sel}_{MC}-N^{sel^2}_{MCisr}}{N^{sel^2}_{MC}}}{N^{sel}_{MC}}}$$

$$= \sqrt{\dfrac{\dfrac{N^{sel}_{MCisr}}{N^{sel}_{MC}}-\dfrac{N^{sel^2}_{MCisr}}{N^{sel^2}_{MC}}}{N^{sel}_{MC}}} = \sqrt{\dfrac{\epsilon_{isr}-\epsilon^2_{isr}}{N^{sel}_{MC}}} = \sqrt{\dfrac{\epsilon_{isr}\left(1-\epsilon_{isr}\right)}{N^{sel}_{MC}}} \qquad (A.7)$$

Error on N^{isr}_{bkgd}

$$\Delta N^{isr}_{bkgd} = \sqrt{\left|\dfrac{\partial N^{isr}_{bkgd}}{\partial\epsilon_{isr}}\Delta\epsilon_{isr}\right|^2 + \left|\dfrac{\partial N^{isr}_{bkgd}}{\partial N_{sel}}\Delta N_{sel}\right|^2}$$

$$= \sqrt{\left|N_{sel}\Delta\epsilon_{isr}\right|^2 + \left|\epsilon_{isr}\Delta N_{sel}\right|^2} = \sqrt{N^2_{sel}\Delta\epsilon^2_{isr} + \epsilon^2_{isr}\Delta N^2_{sel}} \qquad (A.8)$$

Systematic error contributions

The contributions to the systematic error on the cross section arising from the background subtraction, the luminosity measurement, the selection and trigger efficiency determinations and from the selection cut variations.

$$\Delta\sigma^{syst}_{bkgd} = \sqrt{\left(\dfrac{\partial\sigma}{\partial N_{bkgd}}\Delta N_{bkgd}\right)^2} = \sqrt{\left(\dfrac{-1}{\mathcal{L}\epsilon_{MC}\epsilon_{trig}}\Delta N_{bkgd}\right)^2}$$

$$= \dfrac{\Delta N_{bkgd}}{\mathcal{L}\epsilon_{MC}\epsilon_{trig}} \qquad (A.9)$$

$$\Delta\sigma^{syst}_{lumi} = \sqrt{\left(\dfrac{\partial\sigma}{\partial\mathcal{L}}\Delta\mathcal{L}\right)^2} = \sqrt{\left(\dfrac{-N_{sig}}{\mathcal{L}^2\epsilon_{MC}\epsilon_{trig}}\Delta\mathcal{L}\right)^2}$$

$$= \dfrac{N_{sig}\Delta\mathcal{L}}{\mathcal{L}^2\epsilon_{MC}\epsilon_{trig}} = \sigma\dfrac{\Delta\mathcal{L}}{\mathcal{L}} \qquad (A.10)$$

$$\Delta\sigma^{syst}_{MCeff} = \sqrt{\left(\dfrac{\partial\sigma}{\partial\epsilon_{MC}}\Delta\epsilon_{MC}\right)^2} = \sqrt{\left(\dfrac{-N_{sig}}{\mathcal{L}\epsilon^2_{MC}\epsilon_{trig}}\Delta\epsilon_{MC}\right)^2}$$

$$= \dfrac{N_{sig}\Delta\epsilon_{MC}}{\mathcal{L}\epsilon^2_{MC}\epsilon_{trig}} = \sigma\dfrac{\Delta\epsilon_{MC}}{\epsilon_{MC}} \qquad (A.11)$$

$$\Delta\sigma^{syst}_{TReff} = \sqrt{\left(\dfrac{\partial\sigma}{\partial\epsilon_{trig}}\Delta\epsilon_{trig}\right)^2} = \sqrt{\left(\dfrac{-N_{sig}}{\mathcal{L}\epsilon^2_{trig}\epsilon_{trig}}\Delta\epsilon_{trig}\right)^2}$$

$$= \dfrac{N_{sig}\Delta\epsilon_{trig}}{\mathcal{L}\epsilon_{MC}\epsilon^2_{trig}} = \sigma\dfrac{\Delta\epsilon_{trig}}{\epsilon_{trig}} \qquad (A.12)$$

$$\Delta\sigma^{syst}_{cuts} = \sigma\times\Delta C^{var}\ [\%] \qquad (A.13)$$

$$\Delta C^{var} = \sqrt{\Delta C^{var^2}_{ASRC} + \Delta C^{var^2}_{\xi MM} + \Delta C^{var^2}_{\xi MX} + \Delta C^{var^2}_{\xi XX} + \Delta C^{var^2}_{P_{max}} + \Delta C^{var^2}_{P_t}}$$

$$\qquad (A.14)$$

A.3   Formulae for A_{fb} measurement

Error on P_{cc}

$$\Delta P_{\mathrm{cc}} = \frac{\sqrt{\frac{N_{\mathrm{cc}}^i\left(N_{\mathrm{all}} - N_{\mathrm{cc}}^i\right)}{N_{\mathrm{all}}}}}{N_{\mathrm{all}}} \tag{A.15}$$

Error on κ

$$
\begin{aligned}
\Delta\kappa &= \sqrt{\left|\frac{\partial\kappa}{\partial P_{\mathrm{cc}}^i}\Delta P_{\mathrm{cc}}^i\right|^2 + \left|\frac{\partial\kappa}{\partial P_{\mathrm{cc}}^j}\Delta P_{\mathrm{cc}}^j\right|^2} \\
&= \sqrt{\left|\frac{(P_{\mathrm{cc}}^j - P_{\mathrm{cc}}^{j\,2})}{(1 - P_{\mathrm{cc}}^i - P_{\mathrm{cc}}^j)^2}\Delta P_{\mathrm{cc}}^i\right|^2 + \left|\frac{(P_{\mathrm{cc}}^i - P_{\mathrm{cc}}^{i\,2})}{(1 - P_{\mathrm{cc}}^i - P_{\mathrm{cc}}^j)^2}\Delta P_{\mathrm{cc}}^j\right|^2} \\
&= \frac{1}{(1 - P_{\mathrm{cc}}^i - P_{\mathrm{cc}}^j)^2}\sqrt{\left(P_{\mathrm{cc}}^j - P_{\mathrm{cc}}^{j\,2}\right)^2\Delta P_{\mathrm{cc}}^{i\,2} + \left(P_{\mathrm{cc}}^i - P_{\mathrm{cc}}^{i\,2}\right)^2\Delta P_{\mathrm{cc}}^{j\,2}}
\end{aligned} \tag{A.16}
$$

In the case that both muons of an event are from the same category, i.e. $i = j$, equation A.16 reduces to:

$$
\begin{aligned}
\Delta\kappa &= \sqrt{\left|\frac{\partial\kappa}{\partial P_{\mathrm{cc}}^i}\Delta P_{\mathrm{cc}}^i\right|^2} = \sqrt{\left|\frac{2P_{\mathrm{cc}}^i(1 - 2P_{\mathrm{cc}}^i) - (-2)P_{\mathrm{cc}}^{i\,2}}{(1 - 2P_{\mathrm{cc}}^i)^2}\Delta P_{\mathrm{cc}}^i\right|^2} \\
&= \left|\frac{2P_{\mathrm{cc}}^i - 2P_{\mathrm{cc}}^{i\,2}}{(1 - 2P_{\mathrm{cc}}^i)^2}\Delta P_{\mathrm{cc}}^i\right| = \left|\frac{2P_{\mathrm{cc}}^{i\,2}(1 - P_{\mathrm{cc}}^i)}{(1 - 2P_{\mathrm{cc}}^i)^2}\frac{\Delta P_{\mathrm{cc}}^i}{P_{\mathrm{cc}}^i}\right| = \kappa^2(1 - P_{\mathrm{cc}}^i)\frac{\Delta P_{\mathrm{cc}}^i}{P_{\mathrm{cc}}^i} \quad \text{(A.17)}
\end{aligned}
$$

Error on $A_{\mathrm{fb}}^{\mathrm{isr}}$

$$
\begin{aligned}
\Delta A_{\mathrm{fb}}^{\mathrm{isr}} &= \sqrt{\left|\frac{\partial A_{\mathrm{fb}}^{\mathrm{isr}}}{\partial N_{\mathrm{f}}^{\mathrm{isr}}}\Delta N_{\mathrm{f}}^{\mathrm{isr}}\right|^2 + \left|\frac{\partial A_{\mathrm{fb}}^{\mathrm{isr}}}{\partial N_{\mathrm{b}}^{\mathrm{isr}}}\Delta N_{\mathrm{b}}^{\mathrm{isr}}\right|^2} \\
&= \sqrt{\left|\frac{2N_{\mathrm{b}}^{\mathrm{isr}}}{(N_{\mathrm{f}}^{\mathrm{isr}} + N_{\mathrm{b}}^{\mathrm{isr}})^2}\Delta N_{\mathrm{f}}^{\mathrm{isr}}\right|^2 + \left|\frac{-2N_{\mathrm{f}}^{\mathrm{isr}}}{(N_{\mathrm{f}}^{\mathrm{isr}} + N_{\mathrm{b}}^{\mathrm{isr}})^2}\Delta N_{\mathrm{b}}^{\mathrm{isr}}\right|^2} \\
&= \sqrt{\frac{4N_{\mathrm{b}}^{\mathrm{isr}\,2}N_{\mathrm{f}}^{\mathrm{isr}}}{(N_{\mathrm{f}}^{\mathrm{isr}} + N_{\mathrm{b}}^{\mathrm{isr}})^4} + \frac{4N_{\mathrm{f}}^{\mathrm{isr}\,2}N_{\mathrm{b}}^{\mathrm{isr}}}{(N_{\mathrm{f}}^{\mathrm{isr}} + N_{\mathrm{b}}^{\mathrm{isr}})^4}} = \sqrt{\frac{4N_{\mathrm{b}}^{\mathrm{isr}}N_{\mathrm{f}}^{\mathrm{isr}}(N_{\mathrm{b}}^{\mathrm{isr}} + N_{\mathrm{f}}^{\mathrm{isr}})}{(N_{\mathrm{f}}^{\mathrm{isr}} + N_{\mathrm{b}}^{\mathrm{isr}})^4}} \quad \text{(A.18)} \\
&= 2\sqrt{\frac{N_{\mathrm{f}}^{\mathrm{isr}}N_{\mathrm{b}}^{\mathrm{isr}}}{(N_{\mathrm{f}}^{\mathrm{isr}} + N_{\mathrm{b}}^{\mathrm{isr}})^3}}
\end{aligned}
$$

Error on $A_{\mathrm{fb}}^{\mathrm{BgC}}$

$$
\begin{aligned}
\Delta A_{\mathrm{fb}}^{\mathrm{BgC}} &= \sqrt{\left|\frac{\partial A_{\mathrm{fb}}^{\mathrm{BgC}}}{\partial A_{\mathrm{fb}}^{\mathrm{fit}}}\Delta A_{\mathrm{fb}}^{\mathrm{fit}}\right|^2 + \left|\frac{\partial A_{\mathrm{fb}}^{\mathrm{BgC}}}{\partial(\sum_i\omega_i A_{\mathrm{fb}}^{\mathrm{bkgd}^i})}\Delta(\textstyle\sum_i\omega_i A_{\mathrm{fb}}^{\mathrm{bkgd}^i})\right|^2 + \left|\frac{\partial A_{\mathrm{fb}}^{\mathrm{BgC}}}{\partial(\sum_i\omega_i)}\Delta(\textstyle\sum_i\omega_i)\right|^2} \\
&= \sqrt{\frac{\Delta A_{\mathrm{fb}}^{\mathrm{fit}\,2}}{(1 - \sum_i\omega_i)^2} + \frac{(\Delta(\sum_i\omega_i A_{\mathrm{fb}}^{\mathrm{bkgd}^i}))^2}{(1 - \sum_i\omega_i)^2} + \frac{(\sum_i\omega_i A_{\mathrm{fb}}^{\mathrm{bkgd}^i} - A_{\mathrm{fb}}^{\mathrm{fit}})^2}{(1 - \sum_i\omega_i)^4}(\Delta(\textstyle\sum_i\omega_i))^2}
\end{aligned} \quad \text{(A.19)}
$$

with

$$\Delta(\textstyle\sum_i \omega_i A_{\mathrm{fb}}^{\mathrm{bkgd}\,i}) = \sqrt{\sum_i \left|\Delta(\omega_i A_{\mathrm{fb}}^{\mathrm{bkgd}\,i})\right|^2} \tag{A.20}$$

$$
\begin{aligned}
\Delta(\omega_i A_{\mathrm{fb}}^{\mathrm{bkgd}\,i}) &= \sqrt{\left|\frac{\partial(\omega_i A_{\mathrm{fb}}^{\mathrm{bkgd}\,i})}{\partial \omega_i}\Delta\omega_i\right|^2 + \left|\frac{\partial(\omega_i A_{\mathrm{fb}}^{\mathrm{bkgd}\,i})}{\partial A_{\mathrm{fb}}^{\mathrm{bkgd}\,i}}\Delta A_{\mathrm{fb}}^{\mathrm{bkgd}\,i}\right|^2} \\
&= \sqrt{\left|A_{\mathrm{fb}}^{\mathrm{bkgd}\,i}\Delta\omega_i\right|^2 + \left|\omega_i \Delta A_{\mathrm{fb}}^{\mathrm{bkgd}\,i}\right|^2} \\
&= \sqrt{A_{\mathrm{fb}}^{\mathrm{bkgd}\,i\,2}\Delta\omega_i^2 + \omega_i^2 \Delta A_{\mathrm{fb}}^{\mathrm{bkgd}\,i\,2}} = \omega_i A_{\mathrm{fb}}^{\mathrm{bkgd}\,i}\sqrt{\frac{\Delta\omega_i^2}{\omega_i^2} + \frac{\Delta A_{\mathrm{fb}}^{\mathrm{bkgd}\,i\,2}}{A_{\mathrm{fb}}^{\mathrm{bkgd}\,i\,2}}}
\end{aligned}
\tag{A.21}
$$

$$\Delta(\textstyle\sum_i \omega_i) = \sqrt{\sum_i |\Delta\omega_i|^2} \tag{A.22}$$

Error on C_{bkgd}

$$
\begin{aligned}
\Delta C_{\mathrm{bkgd}} &= \omega_{\mathrm{bkgd}}\sqrt{\left|\frac{\partial C_{\mathrm{bkgd}}}{\partial A_{\mathrm{fb}}^{\mathrm{BgC}}}\Delta A_{\mathrm{fb}}^{\mathrm{BgC}}\right|^2 + \left|\frac{\partial C_{\mathrm{bkgd}}}{\partial A_{\mathrm{fb}}^{\mathrm{fit}}}\Delta A_{\mathrm{fb}}^{\mathrm{fit}}\right|^2} \\
&= \omega_{\mathrm{bkgd}}\sqrt{\left|\frac{1}{A_{\mathrm{fb}}^{\mathrm{fit}}}\Delta A_{\mathrm{fb}}^{\mathrm{BgC}}\right|^2 + \left|\frac{-A_{\mathrm{fb}}^{\mathrm{BgC}}}{A_{\mathrm{fb}}^{\mathrm{fit}^2}}\Delta A_{\mathrm{fb}}^{\mathrm{fit}}\right|^2} \\
&= \omega_{\mathrm{bkgd}}\sqrt{\frac{\Delta A_{\mathrm{fb}}^{\mathrm{BgC}^2}}{A_{\mathrm{fb}}^{\mathrm{fit}^2}} + \frac{A_{\mathrm{fb}}^{\mathrm{BgC}^2}\Delta A_{\mathrm{fb}}^{\mathrm{fit}^2}}{A_{\mathrm{fb}}^{\mathrm{fit}^4}}} = \omega_{\mathrm{bkgd}}C_{\mathrm{bkgd}}\sqrt{\frac{\Delta A_{\mathrm{fb}}^{\mathrm{BgC}^2}}{A_{\mathrm{fb}}^{\mathrm{BgC}^2}} + \frac{\Delta A_{\mathrm{fb}}^{\mathrm{fit}^2}}{A_{\mathrm{fb}}^{\mathrm{fit}^2}}}
\end{aligned}
\tag{A.23}
$$

Appendix B

Tables

$\sqrt{s}$ [GeV]	Data [%]			Monte Carlo [%]		
	MM	MX	XX	MM	MX	XX
91.31	83.0±1.2	11.6±0.4	5.4±0.3	82.0±0.4	12.1±0.1	5.9±0.1
89.45	81.9±1.7	12.6±0.7	5.5±0.4	81.6±0.4	12.4±0.2	6.0±0.1
91.29	82.9±1.4	11.0±0.5	6.1±0.4	81.6±0.3	12.4±0.1	6.0±0.1
92.98	82.2±1.4	11.3±0.5	6.5±0.4	81.0±0.4	12.9±0.2	6.1±0.1
average	82.4±1.4	11.8±0.5	5.8±0.4	81.5±0.4	12.5±0.2	6.0±0.1
130.0	80.0±9.2	20.0±4.6	-	84.4±1.2	15.6±0.5	-
$\sqrt{s'}$>110.5	93.0±14.7	7.0±4.0	-	87.6±1.8	12.4±0.7	-
135.9	75.6±9.8	24.4±5.6	-	82.8±1.2	17.2±0.6	-
$\sqrt{s'}$>115.5	76.5±15.0	23.5±8.3	-	85.9±1.8	14.1±0.7	-
161.3	75.8±8.9	24.2±5.0	-	83.7±0.9	16.3±0.4	-
$\sqrt{s'}$>137.1	85.0±14.6	15.0±6.1	-	87.6±1.3	12.4±0.5	-
172.1	87.3±11.1	12.7±4.2	-	85.2±0.9	14.8±0.4	-
$\sqrt{s'}$>146.3	91.2±16.4	8.8±5.1	-	88.9±1.3	11.1±0.5	-
182.7	78.5±4.7	21.5±2.5	-	85.7±0.9	14.3±0.4	-
$\sqrt{s'}$>155.3	85.4±7.4	14.7±3.1	-	89.0±1.3	11.0±0.4	-

Table B.1: The ratio of events in the MM, MX and XX samples for data and the Monte Carlo prediction for all data taking periods. The average is weighted with respect to luminosity.

$\sqrt{s}$ [GeV]	$e^+e^- \to \tau^+\tau^-(\gamma)$ background [%]	$e^+e^- \to e^+e^-\mu^+\mu^-(\gamma)$ background [%]	$e^+e^- \to q\bar{q}(\gamma)$ background [%]
91.31	1.05±0.05	0.05±0.01	0.03±0.02
89.45	1.09±0.04	0.14±0.02	0.05±0.02
91.29	1.03±0.04	0.04±0.01	0.03±0.02
92.98	1.08±0.04	0.10±0.02	0.06±0.02
130.0	1.3±0.1	2.0±0.4	-
$\sqrt{s'}$>110.5	0.6±0.1	1.0±0.4	-
135.9	1.2±0.1	3.1±0.6	-
$\sqrt{s'}$>115.5	0.6±0.1	0.9±0.5	-
161.3	1.6±0.1	6.8±1.0	-
$\sqrt{s'}$>137.1	0.9±0.1	3.6±1.1	-
172.1	1.8±0.1	9.1±1.5	-
$\sqrt{s'}$>146.3	1.0+0.1	3.9±1.4	-
182.7	1.7±0.1	18.0±1.3	-
$\sqrt{s'}$>155.3	1.0±0.1	7.0±1.3	-

$\sqrt{s}$ [GeV]	$e^+e^- \to W^+W^-(\gamma)$ background [%]	cosmic radiation background [%]	$e^+e^- \to \mu^+\mu^-\gamma_{ISR}$ background [%]
91.31	-	0.09±0.02	-
89.45	-	0.18±0.03	-
91.29	-	0.03±0.01	-
92.98	-	0.11±0.02	-
130.0	-	0.8±0.4	-
$\sqrt{s'}$>110.5	-	0.9±0.7	8.0±0.5
135.9	-	1.0±0.5	-
$\sqrt{s'}$>115.5	-	2.4±1.2	6.6±0.5
161.3	0.3±0.1	0.4±0.2	-
$\sqrt{s'}$>137.1	0.2±0.1	0.8±0.4	5.5±0.3
172.1	1.5±0.2	1.8±0.5	-
$\sqrt{s'}$>146.3	1.0±0.2	1.8±0.7	5.2±0.3
182.7	2.1±0.1	1.1±0.3	-
$\sqrt{s'}$>155.3	1.9±0.2	1.3±0.4	4.4±0.3

$\sqrt{s}$ [GeV]	$e^+e^- \to Ze^+e^-(\gamma)$ background [%]	$e^+e^- \to ZZ(\gamma)$ background [%]	$e^+e^- \to e^+e^-\tau^+\tau^-(\gamma)$ background [%]
130.0	0.14±0.02	0.05±0.01	-
$\sqrt{s'}$>110.5	0.02±0.01	0.04±0.01	-
135.9	0.15±0.02	0.05±0.01	-
$\sqrt{s'}$>115.5	0.04±0.02	0.03±0.01	-
161.3	0.24±0.02	0.09±0.01	-
$\sqrt{s'}$>137.1	0.06±0.02	0.06±0.01	-
172.1	0.38±0.03	0.11±0.01	-
$\sqrt{s'}$>146.3	0.11±0.03	0.07±0.01	-
182.7	0.46±0.03	0.19±0.01	0.3±0.2
$\sqrt{s'}$>155.3	0.11±0.03	0.18±0.01	0.2±0.2

Table B.2: The background contamination for all background sources and all data taking periods.

Bibliography

[1] F. Halzen, A.D. Martin, *Quarks & Leptons: An Introductory Course in Modern Particle Physics*, J. Wiley and Sons, New York (1984)

[2] S.L. Glashow, Nucl. Phys. **22** (1961) 579
A. Salam, J.C. Ward, Phys. Lett. **13** (1964) 168
S. Weinberg, Phys. Rev. Lett. **19** (1967) 1264

[3] The Particle Data Group, R.M. Barnett *et al.*, Phys. Rev. **D 54** (1996) 1

[4] P.W. Higgs, Phys. Lett. **12** (1964) 132
P.W. Higgs, Phys. Rev. Lett. **13** (1964) 508
P.W. Higgs, Phys. Rev. **145** (1966) 1156

[5] M. Consoli, W. Hollik, CERN Report **89-08 Vol.I** (1989) 7

[6] F.A. Berends, CERN Report **89-08 Vol.I** (1989) 89

[7] M. Böhm, W. Hollik, CERN Report **89-08 Vol.I** (1989) 203

[8] S. Jadach, J.H. Kühn, R.G. Stuart and Z. Was, Z. Phys. **C 38** (1988) 609

[9] S. Eidelmann, F. Jegerlehner, Z. Phys. **C 67** (1995) 585

[10] A. Leike, T. Riemann,J. Rose Phys. Lett. **B 273** (1991) 513
T. Riemann, Phys. Lett. **B 293** (1992) 451

[11] A.A. Sokolov, I.M. Ternov, Sov. Phys. Dokl.8 (1964) 1203

[12] P. Garcia-Abia *et al.*, L3 Note **2131** (1997)

[13] Gargamelle Collab. , F.J. Hasert *et al.*, Phys. Lett. **B 46** (1973) 121
Gargamelle Collab. , F.J. Hasert *et al.*, Phys. Lett. **B 46** (1973) 138

[14] UA1 Collab. , G. Arnison *et al.*, Phys. Lett. **B 122** (1983) 103
UA2 Collab. , M. Banner *et al.*, Phys. Lett. **B 122** (1983) 476

[15] ALEPH Collab., D. Decamp *et al.*, Nucl. Inst. Meth. **A 294** (1990) 121
DELPHI Collab., P. Aarnio *et al.*, Nucl. Inst. Meth. **A 303** (1991) 233
OPAL Collab., K. Ahmet *et al.*, Nucl. Inst. Meth. **A 305** (1990) 275

[16] L3 Collab., B. Adeva *et al.*, Nucl. Inst. Meth. **A 289** (1990) 35

[17] I.C. Brock *et al.*, *Luminosity Measurement in the L3 Detector at LEP*, CERN-PPE **96-89** (1996)
M. Acciarri *et al.*, *Luminosity Measurement in the L3 Detector at LEP*, Nucl. Inst. Meth. **A 381** (1996) 236

[18] M. Acciarri *et al.*, *The L3 Silicon Micro-vertex Detector*, Nucl. Inst. Meth. **A 351** (1994) 300

[19] F. Beissel *et al.*, *Construction and Performance of the L3 Central Tracking Detector*, Nucl. Inst. Meth. **A 332** (1993) 33

[20] K. Deiters *et al.*, *Construction and Performance of a Large Cylindrical Wire Chamber with Cathode Readout*, Institut für Hochenergiephysik Zeuthen, PHE **91-015** (1991)

[21] L3 Collab., B. Adeva *et al.*, *The L3 BGO Electromagnetic Calorimeter*, Nucl. Inst. Meth. **A 265** (1988) 252

[22] L3 Collab., O. Adriani *et al.*, Physics Reports **236** (1993) 1

[23] U. Uwer, *Aufbau und Eichung der Szintillationszähler des L3-Experiments*, Diplomarbeit, RWTH Aachen (1990)

[24] L3 Collab., O. Adriani *et al.*, *Hadron Calorimetry in the L3 Detector*, Nucl. Inst. Meth. **A 302** (1991) 53

[25] L3 Collab., B. Adeva *et al.*, *Muon Detection in the L3 Experiment at LEP*, Nucl. Inst. Meth. **A 277** (1989) 187
L3 Collab., B. Adeva *et al.*, *Test Results of the L3 Precision Muon Detector*, Nucl. Inst. Meth. **A 289** (1990) 335

[26] L3 Collab., A. Adam *et al.*, *The Forward Muon Detector of L3*, Nucl. Inst. Meth. **A 383** (1996) 342

[27] R. Santonico, R. Cardarelli, Nucl. Inst. Meth. **A 187** (1981) 377

[28] M. Chemarin *et al.*, Nucl. Inst. Meth. **A 349** (1994) 345

[29] J. Berdugo, C. Burgos, M. Cerrada, K. Deiters, M. Fabre, W. Lustermann, A. Robohm, W. van Rossum, *The Alignment of the L3 Forward-Backward Muon Chambers at LEP 200*, Nucl. Inst. Meth. **A 384** (1997) 364

[30] J. Berdugo, C. Burgos, M. Cerrada, K. Deiters, M. Fabre, W. Lustermann, A. Robohm, W. van Rossum, *The Alignment of the Forward-Backward Muon Chambers*, L3 Note **1909** (1995)

[31] X.D. Cai, *Data Acquisition and Trigger System in the L3 Experiment*, Université de Savoie (Chambéry/Annecy), PhD. thesis (1994)

[32] P. Bene *et al.*, *First Level Charged Particle Trigger for the L3 Detector*, Nucl. Inst. Meth. **A 306** (1991) 150

[33] J. Perrier, *Level-1 TEC Trigger*, L3 Note **622** 1989
M. Bourquin *et al.*, *First - Level Charged Particle Trigger for the L3 Detector*, Nucl. Inst. Meth. **A 306** (1991) 151; L3 Note **1014** (1990)

[34] R. Bizzari *et al.*, *The L3 Energy Trigger*, Nucl. Inst. Meth. **A 283** (1989) 799
P. Bagnaia *et al.*, *The First Level Energy Trigger of the L3 Experiment*, Nucl. Inst. Meth. **A 324** (1993) 101
P. Bagnaia *et al.*, *The L3 Energy Trigger for the LEP 8 bunch operation*, Nucl. Inst. Meth. **A 323** (1992) 528

[35] M. Fukushima, *L3 Level 1 Muon Trigger*, L3 Note **515** (1987)
T.S. Dai, M. Fukushima, *L3 Level 1 Muon Trigger Schematics*, L3 Note **668** (1989)

[36] G. Carlino, P. Paolucci, D. Piccolo, *The forward-backward Trigger Efficiency*, L3 Note **1951** (1996)

[37] Y. Bertsch *et al.*, *The Second Level Trigger of the L3 Experiment*, Nucl. Inst. Meth. **A 340** (1994) 309

[38] C. Dionisi *et al.*, *The Third Level Trigger System of the L3 Experiment at LEP*, Nucl. Inst. Meth. **A 306** (1991) 150

[39] L. Arnaudon *et al.*, Phys. Lett. **B 284** (1992) 431
L. Arnaudon *et al.*, *Accurate Determination of the LEP beam energy by Resonant Depolarization*, CERN-SL **94-71** (1994)

[40] The Working Group on LEP energy, R. Assmann *et al.*, Z. Phys. **C 66** (1995) 567
The Working Group on LEP energy, *LEP Energy Calibration in 1993, 1994 and 1995*, Internal Note **95-10**
The Working Group on LEP energy, *LEP Energy Calibration in 1996*, Internal Note **97-01**

[41] L3 Collab., M. Acciarri *et al.*, Z. Phys. **C 62** (1994) 551
I.C. Brock, *et al.*, Nucl. Inst. Meth. **A 381** (1996) 236

[42] L3 Collab., B. Adeva *et al.*, Nucl. Inst. Meth. **A 289** (1990) 35

[43] C. Checci *et al. BGO Calibration at LEP II*, L3 Note **1892** (1995)

[44] U. Uwer, *The L3 Scintillation Counter System: Description and Status*, L3 Note **2003** (1996)

[45] D. Bourilkov, G. Rahal-Callot, *TEC Calibration at LEP2 using High Energy Lepton Pairs*, L3 Note **2047** (1997)

[46] G. Carlino, P. Paolucci, D. Piccolo, *RPC Performances at L3 experiment*, L3 Note **1811** (1995)

[47] J. Swain, L. Taylor, *L3 Computing Guide*, Northeastern University **NUB-3065** (1993)

[48] R. Brun *et al.*, *GEANT* , CERN DD/EE/84-1 (Revised), 1987
GEANT Version 3.16 (1993) is used

[49] S. Jadach *et al.*, Comp. Phys. Comm. **70** (1992) 305
S. Jadach *et al.*, Phys. Lett. **B 353** (1995) 349
S. Jadach *et al.*, Phys. Lett. **B 353** (1995) 362
S. Jadach *et al.*, CERN-TH **96-158**, submitted to Comp. Phys. Comm.

[50] F.A. Berends, P.H. Daverfeldt, R. Kleiss, Nucl. Phys. **B 253** (1985) 441

[51] T. Sjöstrand, *PYTHIA 5.7 and JETSET 7.4 Physics and Manual*, CERN-TH **7112/93** (1993), Comp. Phys. Comm. **82** (1994) 74

[52] F. James, M. Roos, *MINUIT, Function Minimization and Error Analysis*, CERN Program Library Long Writeup **D506** (1992)

[53] M. Skrzypek, S. Jadach, W. Placzek, Z. Was, Comp. Phys. Comm. **94** (1996) 216
M. Skrzypek, S. Jadach, M. Martinez, W. Placzek, Z. Was, Phys. Lett. **B 372** (1996) 289

[54] S. Jadach, B.F.L. Ward, Z. W as, Comp. Phys. Comm. **79** (1994) 503

[55] D. Bardin *et al. An Analytical Program for Fermion Pair Production in e^+e^- annihilation*, CERN-TH **6443/92** (1992)

[56] S. Kirsch, T. Riemann, Phys. Comm. **88** (1995) 89

[57] The LEP Electroweak Working Group, CERN-PPE **95-172** (1995)

[58] CDF Collab., F. Abe *et al.*, Phys. Rev. Lett. **74** (1995) 2626
D0 Collab., F. Abachi *et al.*, Phys. Rev. Lett. **74** (1995) 2632

[59] M. Fabre, *The Dimuon Mass Resolution of the L3 experiment at LEP*, ETH Zürich, PhD. thesis **9696** (1992)

[60] C. Paus, *Measurement of the Hadron Cross Section with the L3 Detector and Determination of Standard Model Parameters*, RWTH Aachen, PhD. thesis (1996)

[61] S. Roth, *Messung der Myonpaarproduktion und ihrer Strahlungskorrekturen mit dem L3-Detektor bei LEP*, RWTH Aachen, PhD. thesis (1997)

[62] D. Bourilkov, *Large Angle Bhabha Cross Section and Forward-Backward Asymmetry from 1991 and 1992 L3 Data*, L3 Note **1497** (1993)

[63] L3 Collab., B. Adeva *et al.*, Z. Phys. **C 62** (1994) 551

[64] L3 Collab., M. Acciarri *et al.*, *Determination of Electroweak Parameters from the Measurement of Hadronic and Leptonic Cross Sections and Forward-Backward Asymmetries at the Z Resonance and Determination of Electroweak Parameters*, to be submitted

[65] L3 Collab., M. Acciarri *et al.*, Phys. Lett. **B 370** (1996) 195

[66] L3 Collab., M. Acciarri *et al.*, Phys. Lett. **B 407** (1997) 361

[67] L3 Fermion-Pair Production Group, L3 Note **2227** (1998)

[68] L3 Collab., O. Adriani *et al.*, Phys. Lett. **B 315** (1993) 494

[69] G. Isidori, Phys. Lett. **B 314** (1993) 139
M. Grünewald, S. Kirsch, Preprint CERN-PPE **93-188** (1993)

Acknowledgements

Without the help, advice and criticism of many members of the L3 collaboration, it would have been impossible to write this thesis and I am very grateful for all the support I received.

First of all, I would like to thank the examiner, Prof. Dr. H. Hofer, and co-examiner of this thesis, Prof. Dr. H.C. Walter. I am indebted to M. Pohl, M. Fabre and T. Siedenburg, who were always there during the past four years when an *insoluble* problem had to be solved and who taught me a lot about experiment and data analysis.

During the installation of the alignment system of the forward-backward muon chambers I enjoyed working with K. Deiters and W. Lustermann.

R. Bock, S. Roth and U. Uwer *introduced me to the muon pairs* and helped me to become familiar with software and analysis techniques. I also would like to thank D. Bourilkov for patiently explaining to me the details of charge confusion.

I very much appreciated the team work in the muon group under the leadership of U. Becker. Many suggestions and constructive criticism came from the lineshape group. Here I would like to thank especially J. Mnich and C. Paus.

Of course, there are many more who are not mentioned but whose help and support I will not forget. Thanks, Jon, for reading my thesis.

Last, but not least, I want to thank all my friends I had a great time with in Geneva.

Curriculum Vitae

Name: Arne Robohm

Date of birth: June 14, 1967

Place of birth: Hamburg (Germany)

1973 - 1986 *Grundschule* and *Gymnasium* in Bad Wimpfen.
Certificate: Abitur

1986 - 1987 Military service

1987 - 1993 Physics studies at the University of Karlsruhe, *Diplomarbeit* at the DELPHI experiment at CERN (1991/92).
Certificate: Diplom

since 1994 Scientific assistent at the ETH Zürich and the Paul-Scherrer-Institut. PhD thesis at the L3 experiment at CERN.

Lebenslauf

Name: Arne Robohm

Geburtsdatum: 14. Juni 1967

Geburtsort: Hamburg

1973 - 1986 Grundschule und Gymnasium in Bad Wimpfen.
Abschluss: Abitur

1986 - 1987 Grundwehrdienst

1987 - 1993 Physikstudium an der Universität Karlsruhe, Diplomarbeit beim
DELPHI Experiment am CERN (1991/92).
Abschluss: Diplom

seit 1994 Wissenschaftlicher Assistent der ETH Zürich and des Paul-Scherrer-
Instituts. Doktorarbeit beim L3 Experiment am CERN.